



Run Run Shaw Library

香港城市大學
City University of Hong Kong

Copyright Warning

Use of this thesis/dissertation/project is for the purpose of private study or scholarly research only. ***Users must comply with the Copyright Ordinance.***

Anyone who consults this thesis/dissertation/project is understood to recognise that its copyright rests with its author and that no part of it may be reproduced without the author's prior written consent.

**OBSERVED DISPERSION
CHARACTERISTICS AND
EVOLUTION OF TROPICAL
PACIFIC MIXED-ROSSBY
GRAVITY WAVES IN BOREAL
SUMMER**

AU-YEUNG YEE MAN

**DOCTOR OF PHILOSOPHY
CITY UNIVERSITY OF HONG KONG**

SEPTEMBER 2015

CITY UNIVERSITY OF HONG KONG

香港城市大學

**Observed Dispersion Characteristics and
Evolution of Tropical Pacific Mixed-Rossby
Gravity Waves in Boreal Summer**

**夏季太平洋熱帶混合羅斯貝重力波
頻散及其演變特徵**

**Submitted to
School of Energy and Environment
能源及環境學院
in Partial Fulfillment of the Requirements
for the Degree of Doctor of Philosophy
哲學博士學位**

by

**Au-Yeung Yee Man
歐陽綺雯**

**September 2015
二零一五年九月**

Abstract

A new algorithm has been developed to track westward travelling mixed-Rossby gravity waves (MRG) waves in the western Pacific based on the theoretical meridional wind structure stated in the shallow water equation (SWE) solutions. Applied to space-time filtered (period=3 to 8 days and wavenumber $k=-20$ to 0), asymmetric meridional wind data at the 850hPa level from a reanalysis dataset, the algorithm finds locations with Gaussian-shaped meridional wind structure stated in SWE solutions through space and time. Local and instantaneous wave properties such as occurrence time, wavenumber, intrinsic frequency and magnitude, are then examined.

It was found that the tracked low-level MRG waves can be classified into two groups: one with higher wavenumber ($k \sim 11$) and another one with lower-wavenumber ($k \sim 6$). Moreover, the MRG waves show very different dispersive properties and occurrence behavior in the western and eastern equatorial Pacific. While both groups appear in the western Pacific, mainly $k \sim 6$ waves were found in the eastern Pacific. The fact that both $k \sim 6$ and $k \sim 11$ waves appear in the western Pacific agrees with past discussions on the co-existence of MRG waves and tropical-disturbance type (TD-type) waves. Also, MRG waves in

the western Pacific were observed to have larger variation in their dispersive properties, implying that they do not have a very regular waveform in terms of their wavenumber and frequencies and it is better to track them without assuming any waveform in space. Furthermore, the high-wavenumber wave activities mainly appear west of the dateline, meaning that some triggering process may have taken place there.

Low-level wind composites found east of $\sim 140^{\circ}\text{E}$ agree with the alternating cyclonic and anti-cyclonic patterns given by SWE solutions. Northwestward wave train movement was found west of $\sim 140^{\circ}\text{E}$. On the other hand, negative correlation between meridional wind and temperature (negative $\overline{v'T}$) found in the vertical composites indicates downward vertical wave activity flux prior to the occurrences of MRG waves. Finally, in the western Pacific, kinetic energy energetics suggests that energy source of transient eddies is from the confluent background flow and also the zonal wind shear terms in the western Pacific, while the energy source in eastern Pacific mainly comes from the meridional shear in the barotropic convergence term.

Overall, our method provides a way to identify the MRG waves instantaneously; in contrast, most of the methods employed in the past (e.g., spectral analysis or lag correlation/regression) are based on aggregates of data and

they can only examine wave properties averaged over a certain period of time.

Since MRG waves can serve as precursors for tropical cyclone formation,

recording the space-time properties of MRG waves in an instantaneous sense

should be useful for studying possible formation mechanisms.

CITY UNIVERSITY OF HONG KONG
Qualifying Panel and Examination Panel

Surname: AU-YEUNG
First Name: Yee Man
Degree: Doctor of Philosophy
College/Department: Sch of Energy and Environment

The Qualifying Panel of the above student is composed of:

Supervisor(s)

Prof. CHAN Chung Leung Sch of Energy and Environment
Johnny City University of Hong Kong

Qualifying Panel Member(s)

Dr. NGAN Keith Sch of Energy and Environment
City University of Hong Kong

Dr. ZHOU Wen Sch of Energy and Environment
City University of Hong Kong

This thesis has been examined and approved by the following examiners:

Dr. ZHOU Wen Sch of Energy and Environment
City University of Hong Kong

Prof. CHAN Chung Leung Sch of Energy and Environment
Johnny City University of Hong Kong

Prof. KUO Hung-chi Department of Atmospheric Science
National Taiwan University

Prof. SOBEL Adam Department of Applied Physics and Applied Mathematics
Columbia University, USA

Acknowledgements

I would like to take this opportunity to thank my beloved mother, who has always allowed me to pursue things I feel intrigued and truly enjoy. Not for once has she ever asked me to live my life like other people. I would also like to express my gratitude to my supervisor Professor Francis Chi-Yung Tam, who has guided me in conducting scientific research independently and has given me minimal amount of limitations in my study.

It was a delightful time to share with other research students at CityU including Glory L. K. Kwok, Eric K. W. Ng, Ray W. K. Lee and Christopher C. Holst. I am grateful that we had each other's backs when we were going through hard times. We discussed our studies and we learnt a lot from each other. I sincerely hope that everyone of us will be able to work in fields that we enjoy.

My gratitude also goes to the external examiners, Professor Adam Sobel and Professor Hung-Chi Kuo, for their responses and ideas raised in the final stage of my study. Finally I would also like to thank Professor Johnny Chan and Professor Wen Zhou for their valuable comments from time to time during my study period.

Table of Contents

Abstract	i
Acknowledgements	v
Table of Contents	vi
List of Acronyms	ix
List of Symbols	x
List of Figures	xi
List of Tables	xviii
Chapter 1 Introduction	1
1.1 Background	1
1.2 Objectives	7
1.3 Overview of chapters	7
Chapter 2 Literature Review	8
2.1 Intertropical convergence zone (ITCZ) and variability in the Tropics	8
2.2 Shallow Water Equations (SWE)	13
2.3 Wave properties: Spectra and dispersion	19
2.4 Observing convectively coupled MRG waves	25

2.5	Dynamical structure of MRG waves and associated convective activities	29
2.6	Wave energetics	38
2.7	Wave transition, energy accumulation and TC genesis	41
2.8	Interannual variation of MRG waves	46
2.9	Origins of synoptic-scale waves	48
2.10	Summary	50
Chapter 3	Data and Methodology	53
3.1	Data and filtering	53
3.2	Theoretical profile for MRG waves (mode n=0)	54
3.3	Matching filtered data with theoretical profile	56
3.4	Local wavenumber from wavelet analysis	59
3.5	Tracking MRG waves	60
3.6	Other methods	62
3.7	Summary of the new algorithm	63
Chapter 4	Wave features in CFSR dataset as inferred from spectral and regression-based methods	66
4.1	Spectral analysis	66
4.2	Variance of filtered meridional wind	78

4.3	Lag-correlation analysis	82
4.4	Summary	86
Chapter 5	Wave features tracked by dynamical method	88
5.1	Dispersion diagrams	88
5.2	Occurrences of MRG waves	93
5.3	Composites of three-dimensional circulation and convection	97
5.3.1	Composites at t=0day	100
5.3.2	Composites from t=-5.5day to 4day	107
5.4	Energetics	114
Chapter 6	Discussion and Conclusion	121
References	126	
Appendix – Composites of MRG structures in western Pacific		134

List of Acronyms

EOF	empirical orthogonal function
MRG	mixed-Rossby gravity waves
OLR	outgoing longwave radiation
PC	principal component
SWE	shallow water equations
TC	tropical cyclone
TD-type	Tropical-Disturbance type
MSU	microwave sounding unit
EKE	eddy kinetic energy

List of Symbols

u', v', Φ'	Zonal wind, meridional wind, geopotential height perturbation around a motionless basic state
$\hat{u}, \hat{v}, \hat{\Phi}$	Meridional structure function of zonal wind, meridional wind, geopotential height
k	Wavenumber
ω	Wave frequency
f	Coriolis parameter
β	Latitudinal gradient of f in beta-plane approximation
h_e	Mean depth of shallow water layer / equivalent depth / equivalent height
D_n	Parabolic cylinder function of order n
K'	Eddy kinetic energy

List of Figures

Figure 1 – Schematic of trade winds coming from northern and southern hemisphere converge in an area called intertropical convergence zone (ITCZ). The "H" indicates sea-level high pressure systems. This situation applies to both Atlantic and Pacific Oceans (Wallace and Hobbs 2006).	8
Figure 2 – Time-longitude section of Global Precipitation Climatology Project (GPCP) daily rainfall (mm day^{-1}) averaged from 5°N - 10°N in summer of 2001.	9
Figure 3 – Schematic diagram showing relationship between Intraseasonal variability (ISV) and convective activities with smaller scales (Nakazawa 1988)	11
Figure 4 – Schematic of the situation in the summer western North Pacific. (Chan and Evans 2002)	12
Figure 5 - Relationship between zonal wavenumber ω^* and k^* , which can be expressed in terms of ω and k in (5): $\omega^* = \omega/\beta ghe^{1/2}$ and $k^* = kghe/\beta^{1/2}$. The curves are solutions for (3) up to $n = 4$ except for $n = -1$. (Kiladis et al. 2009)	15
Figure 6 – Horizontal wind distribution for solutions to (3) for different modes (as indicated above each graph). Hatching is for divergence, and shading is for convergence (0.6 unit internal). Unshaded contours are geopotential, with a contour interval of 0.5 units. (see details in Kiladis et al. 2009)	18
Figure 7 – Time series of wind barb for 1958 April obtained from an upper-air observation station over the central Pacific. Observations of MRG waves were shown in the v-wind components, which appeared alternatively. (Yanai and Maruyama 1966)	20
Figure 8 – Power spectra of 850hPa vorticity during period of 1980-1987 June-August seasons with $vP(v)$ (ordinate, units: 10 – 11s – 2day – 1) against $\ln(v)$ (abscissa, units: days) for different locations in western Pacific, where P =power and v =frequency (LL90).	21
Figure 9 – Power spectra of 850hPa v-wind along equator during period of 1980-1987 September-December season, frequency against longitude (left) and wavenumber against frequency (right). Units= m^2s^{-2} day. On the left, dashed contours are 1,2 where solid contours are 3,6,12,20 and	

values above 20 are shaded. On the right, contour values are 5 (dashed), 10, 20, 30... (solid) and values above 20 are shaded. (Liebmann and Hendon 1990)

21

Figure 10 – Lag-correlation between high-pass filtered 850mb v wind at equator, 150°W and itself on different locations. Negative contours are dashed Phase speed

22

Figure 11 – Intrinsic frequencies (units: day⁻¹) versus zonal wave number for different locations in the equatorial area. Left: Obtained from lag correlations and composites on activities found in convection-proxy data. "W" signs are for Indian and western Pacific oceans (65°-145°E); "C"s for central Pacific (180°-90°W), "A"s for Atlantic (65°W-5°E). Dashed lines are the curves for Rossby waves (Liebmann and Hendon 1990) Right: Obtained from composite maps associated with convective activities. (Takayabu and Nitta 1993) Lines: the theoretical dispersion relationships for MRG waves with different equivalent heights (units: m).

24

Figure 12 – The antisymmetric (around equator) OLR wavenumber-frequency power divided by a background spectrum (not shown).

28

Figure 13 – Coherence square (contours) and phase (vectors) of cross-spectra between antisymmetric MSU34 and antisymmetric MSU23 (upper panel), and between antisymmetric OLR and antisymmetric MSU23 (lower panel) for the period 1979-1993 and summed between 15°S and 15°N. Contour interval is 0.05 and an additional contour of 0.02 is added in upper graph. Upward pointing of vectors indicates in phase relationship. MRG dispersion curves with equivalent depths of 25m and 200m are drawn here.

28

Figure 14 – Similar to Figure 12 except contours less than 1.1 and greater than 1.4 are removed. Dispersion curves shown are for $he=8,12,25,50$ and 90m. The enclosed areas indicate the wavenumber-frequency domains used in OLR filtering. (see details in Wheeler and Kiladis 1999)

29

Figure 15 – Distribution of variance of MRG wave filtered OLR (upper panel). Contour interval is 15(Wm⁻²)². Cross sign denotes the position with highest variance. The 14-day running MRG band variance at the cross location(177.5°E, 7.5°N) and annual variation are shown (lower panel). Thin lines are the average values. The MRG wave wavenumber and frequency domain is defined in Figure 14. (Wheeler et al. 2000)

29

- Figure 16 – Maps of regressed OLR (hatching positive/shading negative), 850hPa streamfunction (contours), and 850-hPa wind (vectors) anomalies associated with the OLR variation of the convectively coupled MRG wave (base point 7.5°N, 177.5°E) on day 0. (see details in Wheeler et al. 2000) 31
- Figure 17 – First empirical orthogonal function (EOF) of 2-10 day westward filtered OLR using 30°N-30°S data (negative shaded) and regressed 850hPa wind from 1979 to 2006. (see details in Kiladis et al. 2009) 32
- Figure 18 – Horizontal composites of blackbody temperature (contour, viewed as active convective activities) and 850hPa bandpass filtered wind centered at 5°N, (a) dateline, (b) 170°E, (c) 160°E and (d) 150°E. Contour interval is 2.5K and reference vector indicates 0.6 m s^{-1} . (Takayabu and Nitta 1993) 34
- Figure 19 – Schematics showing convection arrangement (cloud icon) with low level dynamical circulations. H/L are for highs and lows anomaly regions. (Takayabu and Nitta 1993). 34
- Figure 20 – Vertical composite of bandpass-filtered v-wind at equator for (a) dateline and (b) 150°E. Negative values are dashed and contour level is at 0.2 m s^{-1} . (Takayabu and Nitta 1993) 36
- Figure 21 – Vertical cross-sections of composite (a) relative velocity, (b) geopotential height, (c) pressure velocity, (d) temperature and (e) specific humidity of the western Pacific perturbations. Negative values are shaded and contour levels are $3 \times 10^{-6} \text{ s}^{-1}$, 2gpm, $1 \times 10^{-2} \text{ Pa s}^{-1}$, 0.1°C and 2×10^{-4} respectively. Composites are produced from EOF method with synoptic-scale bandpass-filtered data. Locations of the cross-sections shown under (e). (LL90) 37
- Figure 22 – Vertical cross-sections of different terms in eddy kinetic energy balance equation (9) : (a) barotropic conversion, (b) conversion from eddy available potential energy and (c) convergence of eddy geopotential flux. Composites are produced from EOF method with synoptic-scale bandpass-filtered data. Negative values are shaded and the contour interval is $1 \times 10^{-5} \text{ m}^2 \text{ s}^{-3}$ (see details in Lau and Lau 1992) 40
- Figure 23 – Vertically averaged composites of eddy kinetic energy balance terms for TD-type disturbances: (a) EKE, (b) baroclinic conversion, (c) barotropic conversion and (d) convergence of geopotential flux Negative contours are dashed. Contour intervals for (a) are $2.0 \text{ m}^2 \text{ s}^{-2}$ starting from value of 1 and values greater than 12 are shaded. Contour levels for (b),(c),(d) are $2.0 \text{ m}^2 \text{ s}^{-2} \text{ day}^{-1}$ starting from value of 1 and values greater

(less) than 1 (-1) are dark (light) shaded. (Maloney and Dickinson 2003)

40

Figure 24 – Vertical composites of eddy kinetic energy balance terms for TD-type disturbances: (a)EKE, (b) baroclinic conversion, (c) barotropic conversion and (d) convergence of geopotential flux. Negative contours are dashed. Contour intervals for (a) are $4.0\text{m}^2 \text{s}^{-2}$ starting from value of 2 and values greater than 12 are shaded. Contour levels for (b)(c)(d) are $4.0\text{m}^2 \text{s}^{-2} \text{ day}^{-1}$ starting from value of 2 and values greater (less) than 6 (-6) are dark (light) (see Maloney and Dickinson 2003).

41

Figure 25 – 6-10-day filtered wind vectors (ECMWF analyses) on the 315-K surface plotted with 6–10-day OLR (negative in shading) at 0000 UTC of (a) 10 July, (b) 12 July, (c) 14 July, and (b) 16 July 8 in 1987. Tropical Strom Thelma in (a)(b) and Tropical Storm Vernon in (d) are shown in hurricane symbol (see details in Dickinson and Monlinari 2002).

42

Figure 26 – Hovmöller diagram of the unfiltered OLR (shaded) from May 1st to September 1st 2004. Black contours: filtered OLR for MJO averaged from 5°S to 5°N (interval=10 Wm $^{-1}$). Green contours: 850hPa filtered vorticity for $n = 1$ Rossby waves averaged from 5°N to 15°N (interval= $3 \times 10^{-5}\text{s}^{-1}$). Purple contours: 850hPa filtered v-wind for MRG-TD waves averaged from 5°N to 15°N (interval=1.5 ms $^{-1}$). Solid (dashed) contours represent positive (negative) anomalies. Dots indicate the formation longitude and time of TCs. (Ching et al. 2010).

46

Figure 27 – Interannual anomaly of the longitude ($^\circ$) of the easternmost edge of the monsoon trough (line), locations of wave transition (light bar) and the subsurface ocean temperature anomaly ($^\circ\text{C}$) (dark bar) in the western Pacific for the period 1980-2001 July to October (Chen and Huang 2009).

48

Figure 28 – A snapshot of filtered 850hPa v-wind **vdata** (upper panel), its value on equator (line, lower panel) and **v0** found at local maxima and minima (crosses, lower panel) on 2004 June 24th 18 UTC. Negative values are drawn with dashed lines. Unit: m s^{-1} .

57

Figure 29 – The longitudinal distribution of v-wind at 168.5°E on 2004 June 24th 18UTC (see Figure 28). Thick line represents filtered data **vdata** and thin line is the projected values **vfitted** (15). Note that the value of **v0** is the value of filtered data **vdata** at equator. Unit: m s^{-1} .

58

Figure 30 – Upper: same as Figure 28(upper panel). Lower: Spectral power found from wavelet power $W(\mathbf{k}, \mathbf{x})$ (16) with \mathbf{k} and \mathbf{x} as indices of

wavenumber and longitude.	60
Figure 31 – Selected locations (black dots), tracked wave activities (black lines) and filtered v-wind ν in shading.	65
Figure 32 – Spectrum of 850hPa unfiltered v-wind from 1980-2009 April to October over 12 locations in the western North Pacific. The locations are shown in the map. Graphs are plotted with $\nu P(\nu)$ (unit: $m^2 s^{-2}$) against $\ln(\nu)$ (unit: day) where ν = frequency, P = power.	70
Figure 33 – Spectrum power $P(\nu)$ of unfiltered 850hPa v-wind (1980-2009) for the equator against longitudes for months from May to October. The eastward (westward) traveling powers are on left (right) panel. Left y-axis refers to frequency (cycle per day). Right y-axis refers to period in days. The thin lines indicate where period=3day and 8day. (shading unit: $m^2 s^{-1}$)	71
Figure 34 – Same as Figure 33 except for latitude 10°N	72
Figure 35 – The zonal wavenumber-frequency power spectrum of v-wind power (as in Wheeler and Kiladis 1999) calculated for the period 1980-2009 April-October. Power values are the sums between 15°S to 15°N and base-10 logarithm is used.	76
Figure 36 – Same as Figure 35 except the anti-symmetric and symmetric components about the equator are extracted.	77
Figure 37 – Background spectrum produced from adding spectra in Figure 36 together and smoothing with 1-2-1 filter many times (details referred to text).	77
Figure 38 – The symmetric v-wind power divided by background power. The curves are the dispersion profiles for MRG waves ($n = 0$) predicted by shallow water theory. The values of equivalent height $he = 1m, 12m, 25m, 50m$ and ∞ are marked on the curves. Enclosed areas indicate regions of MRG wave domain defined in (a) WK99, (b) Ching et al. 2010 and (c) this study	78
Figure 39 – 850hPa meridional bandpass-filtered wind variance in 1980-2009 April to October.	80
Figure 40 – Mean Wind in 1980-2009 April to October at pressure level (a) 850hPa and (b) 300hPa. Mean zonal wind ($m s^{-1}$) is shown in shading.	81
Figure 41 – The vertical distribution of mean zonal wind ($m s^{-1}$) at 10°N.	81
Figure 42 – Longitude-lag correlation between bandpass 850hPa v-wind at different locations – (15°N,160°E), (15°N,180°), (15°N,160°W), (0°,160°E), (0°,180°) and (0°,160°W) – and filtered 850 v-wind. The slopes of black lines shown in 15°N,160°E graph indicate the values of	

phase speed (\mathbf{vp}) and group speed (\mathbf{vg}). The length of the horizontal black line indicates value of $1/2 \times$ wavelength (λ). 83

Figure 43 – Correlation of filtered 850hPa v-wind at two locations at equator, 150°E (left panel) and dateline (right panel). 86

Figure 44 – Number of occurrences according to intrinsic frequency and wavenumber per summer during 1980-2009 in (a) all three basins, (b) western Pacific, (c) eastern Pacific and (d) Atlantic. Black lines are the dispersion relation of MRG waves and the values are the equivalent height (he) in meter. 92

Figure 45 – Average $\mathbf{v'02}/2$ of tracked wave activity (bar height) and average $\mathbf{v'2}/2$ from filtered wind field (black lines). Color indicates the number of occurrences per season for each bin. Bottom two plots are for the wave activity with absolute wavenumber smaller than 9 and larger than 9. Black lines in all three graphs are identical. Units bar height and line: m^2s^{-2} 96

Figure 46 – Total $\mathbf{v'0xe - (y/y02)2}/2$ of tracked wave activity (shading) and seasonal average $\mathbf{v'(x,y)2}/2$ from filtered wind field (contour). Units: m^2s^{-2} 96

Figure 47 – Composites of MRG wave events at t=0days between 110°E-180 (western Pacific). The filtered variables are (a)-(d) V-wind (contour, at 0.4m s^{-1} levels) and temperature (shading, at 0.225K levels); (e)-(h) geopotential height (contour, at 1gpm levels) and OLR (shading, at 1W m^{-2} levels). Red, black and blue lines are positive, zero and negative values. Red and blue shadings are positive and negative values. (a) and (e) are 850hPa composite maps and (b) and (f) are 200hPa composite maps. (c) and (g) are vertical cross-sections at 15°N . (d) and (h) are vertical cross-sections at the middle longitude of the composites. Vectors in the horizontal cross sections are horizontal wind (ms^{-1}) at that level. Vectors in the vertical cross sections are the pressure velocities (Pa s^{-1}) with values multiplied by 150. The vectors in all graphs are 99.9% above significance level in Student t-test (please refer to text). Values of OLR are shown for all vertical levels in (g) and (h). MRG waves are found with region 110°E to 180° (defined in section 5.1). Total number of events over 30 years is 956. Label bars of temperature and OLR (shadings) can be found in the appendix. 104

Figure 48 – Same as Figure 47 except the graphs are for MRG waves between 180° and 75°W (eastern Pacific). Vectors in the vertical cross sections are the pressure velocities (Pa s^{-1}) with values multiplied by 300.

Total number of events over 30 years is 935.	105
Figure 49 – Average unfiltered 850hPa zonal wind during the times for MRG events tracked in western Pacific (graphs not aligned in longitudes). Left graph is 850hPa distribution of composite zonal wind. Right graph is vertical cross-section of zonal wind. Units: m s^{-1}	106
Figure 50 – Same as Figure 49 except for eastern Pacific	106
Figure 51 – Same as Figure 47 except the graphs are at $t=-5.5\text{day}$. Same values for the contour and shading levels are used here.	112
Figure 52 – Schematic diagram of vertical-latitudinal cross-section of composite $t=-5.5\text{day}$ (refer to Figure 51c). Black boxes indicate the temperature perturbations with words “warm” and “cold”. Red and blue boxes are v-wind perturbations. The red (blue) box with solid lines is the positive (negative) v-wind at high levels between $130^\circ\text{E}-140^\circ\text{E}$ ($150^\circ\text{E}-160^\circ\text{E}$).	113
Figure 53 – Same as Figure 52, except it is for $t=0\text{day}$ (refer to Figure 47). The red box with solid lines is the positive (negative) v-wind at high levels between $140^\circ\text{E}-150^\circ\text{E}$.	113
Figure 54 – Vertical and horizontal composites of average EKE and EKE tendency terms in (9) for MRG waves for the western Pacific. They include (a)(c)(e) three barotropic terms, (e) barotropic energy conversion, or, sum of all barotropic terms, (b) baroclinic conversion, (d) convergence of the geopotential flux, (f) advection of EKE by mean and perturbation flow, and (h) EKE. For each term, a vertical composite (15°N) and a 850hPa horizontal composite are plotted. Red and blue contour lines are positive and negative values. Black contour line equals to zero. Contour interval level is marked on each term. EKE is shown by shading levels.	117
Figure 55 – Same as Figure 54 except for higher horizontal levels (300hPa).	118
Figure 56 – Same as Figure 54 except for the eastern Pacific.	119
Figure 57 – Same as Figure 55 except for the eastern Pacific.	120

List of Tables

Table 1 – Wave properties found by lag correlation graphs (see Figure 10) at different locations in the past studies. They are wavelength (λ), wavenumber (k), observed phase speed (v_p), observed group speed (v_g), intrinsic speed (v_{int}), intrinsic frequency (ω_{int}), and average zonal wind (U). Some variables are not available. 22

Table 2 – Wave properties found from lag correlation graphs (see Figure 42) at different locations. They are wavelength (λ), wavenumber (k), phase speed (v_p), group speed (v_g), intrinsic speed (v_{int}), intrinsic frequency (ω_{int}), equivalent depth (h_e) and average zonal wind (U). 85

Chapter 1

Introduction

1.1 Background

Atmospheric oscillations oftentimes involve periodic changes of air properties in both space and time. Different wave types can have different temporal and spatial scales, ranging from seconds to years, and from meters to a few thousand kilometers. It is important to study how these waves are originated, propagate and evolve; synoptic-scale waves in the Tropics, for instance, can shape the regional rainfall pattern over places where large populations reside.

Matsuno (1966) was the first to provide a theoretical framework of the equatorial atmospheric waves using the shallow water equations (SWE). In this mathematical model, the fluid is incompressible, horizontally homogeneous and under hydrostatic balance. With a resting basic state, no external forcing and no friction, separation of vertical and horizontal motion is possible. At the same time when Matsuno published his results, observations of such waves were reported by Yanai and Maruyama (1966). They found instances during which lower stratospheric wind alternated back and forth from northerly to southerly in the equatorial western Pacific region. These equatorially trapped, westward travelling

tropical waves, with typical period of 5 days and wavelength of 10,000 km (wavenumber of 4), have dynamical properties matching those described by Matsuno's tropical solutions. They are now known as mixed-Rossby Gravity (MRG) waves or Yanai waves, naming after the Japanese meteorologist.

Since then there have been numerous observational studies of tropical or equatorial waves, and their properties including wavelength, periods and propagation direction have been studied using various methods. For instance, spectral properties of different dynamical variables, precipitation and proxies of convective activities were examined by a number of researchers (Lau and Lau 1990; hereafter LL90; Takayabu and Nitta 1993; Takayabu 1994a; Takayabu 1994b; Wheeler and Kiladis 1999, hereafter WK99; Gu and Zhang 2001; Hendon and Wheeler 2008; Gehne and Kleeman 2012). Strongest signals in the space-time cross-spectra were found to be consistent with dispersion diagrams based on the SWE solutions. It was also found that wave properties, even for the same wave type, over the equatorial band can change from one location to another, indicative of strong geographical dependence of wave characteristics in relation to changes in the basic state. Lag-correlation analysis has also been used to find wave properties such as wavelength, phase and group velocity in different locations in the Pacific (Liebmann and Hendon 1990; Dunkerton and Baldwin 1995; Chen and

Huang 2009). Despite the great simplification of SWE, the horizontal dynamic structures obtained from the SWE wave solutions greatly resemble those concerning tropical waves observed in the real atmosphere (Dunkerton and Baldwin 1995; Hendon and Liebmann 1991; Liebmann and Hendon 1990; Wheeler et al. 2000). Typical in these studies, filtered outgoing longwave radiation (OLR, which is treated as a proxy of convection) at a base point was used for linearly regressing various dynamical fields. The resulting circulation patterns, which correspond to one standard deviation of OLR change (hence change in convective activities), were found to be very similar to those from the theoretical SWE solutions. Circulation features, stated in the SWE solutions, such as alternating cyclonic and anti-cyclonic flow at the equator and the anti-symmetric divergent field can be found in the regressed pattern.

In LL90, empirical orthogonal function (EOF) techniques were applied on the bandpass-filtered low-level vorticity, in order to obtain circulation features typically associated with summertime synoptic disturbances in the Tropics. Phase and amplitude were found based on the first and second EOFs and their principal components (PC). Composite maps for different variables, including vorticity, pressure velocity, temperature and specific humidity, were then constructed for different phases of these waves and on different vertical levels. The synoptic-scale

waves were found to be vertically tilted, with different tilting structures in different ocean basins. Off-equatorial wave propagation was also observed in the western North Pacific. With the EOF method, LL90 showed that a substantial amount of tropical variability can be attributed to the synoptic-scale waves, however it was also mentioned that EOF patterns can be sensitive to the size and shape of the analysis domain, and possibly the time period chosen. The dependency of the wave signals, which are derived by this method, on the choice of domain and time period can undermine the robustness of the analysis results.

It should also be mentioned that drastic changes in wave properties or even wave type transformation can happen during the life cycle of these waves (Liebmann and Hendon 1990; Takayabu and Nitta 1993; Zehr 1992; Dickinson and Molinari 2003), especially in western North Pacific monsoon region (Richie and Holland 1999; Sobel and Bretherton 1999; Kuo et al. 2001). MRG waves are also known to be closely related to tropical cyclone (TC) genesis (Dickinson and Molinari 2002; Frank and Roundy 2006), not only by providing favorable conditions, but also by forming part of the positive cyclone vorticity for the growth of TC itself (i.e. providing seeds). It was also suggested (Sobel and Bretherton 1999; Kuo et al. 2001) that wave energy accumulation could occur when MRG waves propagate westward and encounter the low-level westerly

monsoon flow. While past literature provides evidence of these waves, their space-time structure, convective coupling and their relationship with background flow, a novel method is needed to study wave structure transformation happening within the MRG wave trains.

Yang et al. (2003) developed a method to provide instantaneous identification of different tropical wave modes. The instantaneous pattern was obtained by projecting horizontal structures derived from the SWE solutions onto observational data. First, a “trapping scale” y_0 , is chosen by data fitting so that the first few modes of the projected solutions will give the smallest deviation from observations. Once determined, the scale y_0 is universal for all subsequent procedures, and is used to determine latitudinal wave shapes. Westward and eastward-moving components are then separated in the data. Subsequently, each field is projected onto different equatorial modes according to y_0 . This way, the space and time evolution of different modes can then be examined. The method was proved to be able to identify off-equatorial convection associated with westward moving MRG waves. Based on a case study, the observed MRG wave in the eastern Pacific region was found to have a vertical structure resembling the first baroclinic mode. In their later work (Yang et al. 2007a,b,c), indices based on pattern projections were used to perform linear regression for various wave modes,

in order to obtain the corresponding three-dimensional circulation structures and dispersion characteristics. This method is powerful in offering a systematic way to extract wave signals from meteorological data for different wave modes, and the resulting composite wave structures were found to be consistent with tropical wave theory. However, it should be noticed that the composite structures were not extracted directly from the instantaneous data, but were produced by linear regression (as in many past studies). Also, the trapping scale is not allowed to vary over space and time, which limits the projected patterns to a fixed shape trapped near the equator. This will directly affect the signals obtained by linear regression based on these projected patterns. Also, the regressed dynamical patterns are not describing the waves instantaneously; instead the regressed patterns, or the wave properties found from the regressed patterns, are used to represent all concerned activities happening within a period of time. Therefore, if MRG waves really exist and drastic transformation occurs in the wave train, a systematic and instantaneous algorithm is needed for tracking them and analyzing physical processes involved during such transformation.

1.2 Objectives

The intent of this study is to identify the MRG waves under the framework of SWE with filtered wind, such that

- i) MRG dispersion relationship can be found for different basins,
- ii) the geographically dependence of their occurrence and amplitudes can be recorded, and
- iii) the composite maps of different circulation variables can be formed, and diagnostics can be applied for studying the physical processes involved.

1.3 Overview of chapters

The overview of this thesis is as follows. Chapter 2 introduces the theory of MRG waves and previous observational studies. Chapter 3 describes the data used and outlines the methodology of a new wave tracking algorithm. In chapter 4, MRG waves are identified and studied, based on previous wave analysis techniques. Chapter 5 explains the wave features found using the new tracking algorithm. Chapter 6 gives the summary and conclusion of this study.

Chapter 2

Literature Review

2.1 *Intertropical convergence zone (ITCZ) and variability in the Tropics*

As part of the Hadley circulation, the tropical northeasterly trade winds in the northern hemisphere and southeasterly in the southern hemisphere converge in an area called the intertropical convergence zone (ITCZ) near the equator (Figure 1). Such a circulation structure in conjunction with a moist atmosphere can provide a favorable environment for cloud formation and precipitation.

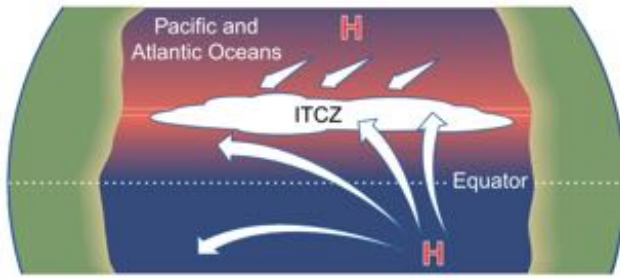


Figure 1 – Schematic of trade winds coming from northern and southern hemisphere converge in an area called intertropical convergence zone (ITCZ). The "H" indicates sea-level high pressure systems. This situation applies to both Atlantic and Pacific Oceans (Wallace and Hobbs 2006).

Oftentimes in the ITCZ region, transient cloud clusters with well-defined propagation can form (Figure 2). In fact, associated with these convective activities are disturbances with distinctive wave-like properties – convectively active and inactive areas are found to alternate in the space and in time. These atmospheric waves exist with various spatial and temporal scales, from mesoscale to planetary scale convective activities, from a few days to months, and can be

spotted propagating eastward or westward around the equatorial area.

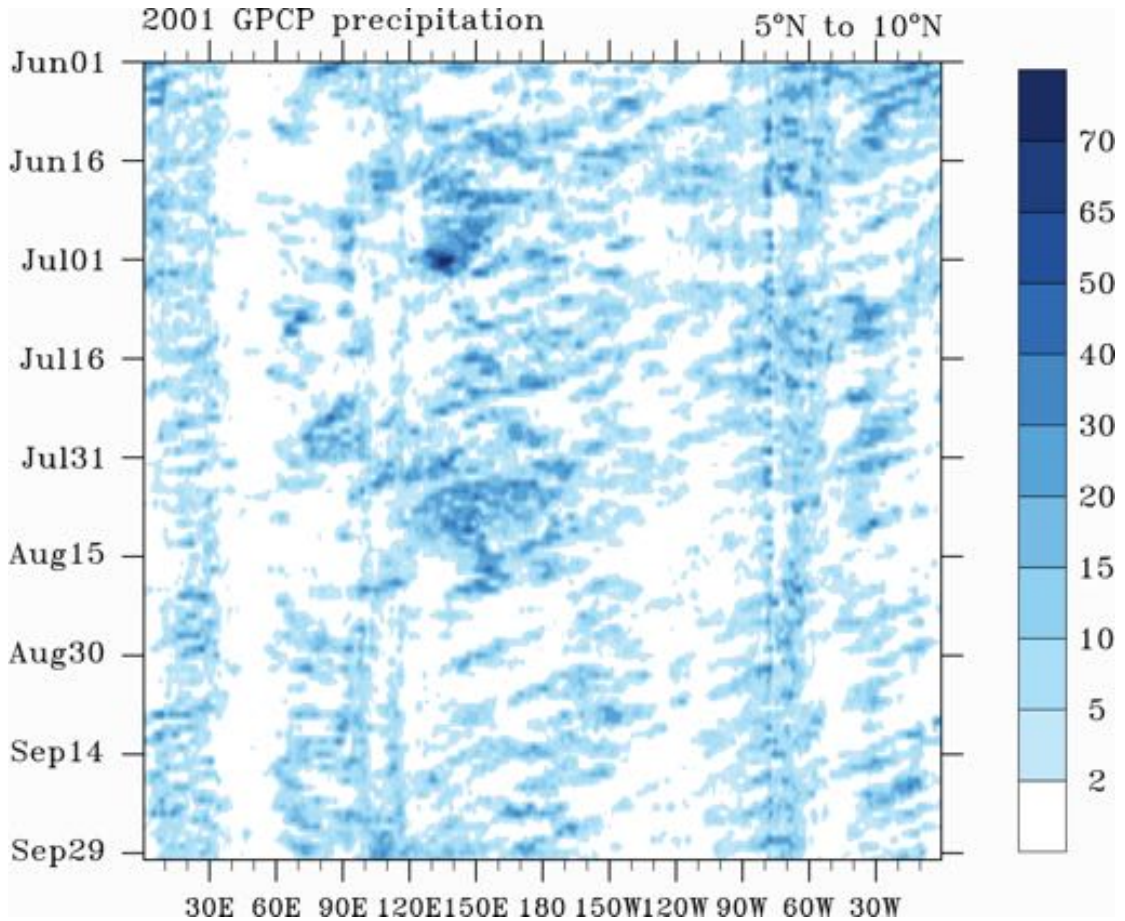


Figure 2 – Time-longitude section of Global Precipitation Climatology Project (GPCP) daily rainfall (mm day^{-1}) averaged from 5°N - 10°N in summer of 2001.

Synoptic-scale waves in the Tropics, also known as “easterly waves” because of the background low-level easterly wind in the Caribbean Sea, were first discussed by Riehl (1945). The mathematical framework for describing tropical equatorial waves was worked out by Matsuno (1966) using shallow water equations (SWE, to be described in next section), and these waves were subsequently observed in the lower stratosphere in the 1960s (Yanai and Maruyama 1966; Maruyama and Yanai 1967; Wallace and Kousky 1968) over the

tropical region. The features of these eastward and westward travelling synoptic-scale tropical waves observed in these studies resemble those described in Matsuno's solution to SWE. In particular, periodic fluctuations in the meridional wind (v-wind) with a typical period of 5days (Yanai and Maruyama 1966) provided evidence for existence of MRG waves in the atmosphere. Similarly, fluctuations in the zonal wind (Wallace and Kousky 1968) also supported the existence of atmospheric Kelvin waves. Using upper air data, Wallace and Chang (1969) performed spectral analysis on wave activity in the equatorial lower troposphere and found disturbances with different temporal and spatial scales, namely the horizontal (temporal) scales of 3,000km (4-5days), 10,000km (more than 10days) and wavenumber 1 planetary-scale fluctuations (4-5days). The use of satellite data provided broader pictures of these disturbances (Chang 1970; Reed and Recker 1971). Satellite photographs of Chang 1970 showed clearly longitudinal movement of cloud clusters in the Tropics. Reed and Recker (1971) averaged over data from 18 disturbances in the tropical western Pacific, in order to construct a composite structure of these waves. They found an average wavelength of 3500-4000km and phase speed of 9ms^{-1} , along with well-defined circulation and relationship between circulation variables, including cold anomalies close the surface trough, eastward (westward) tilting in central

(western) Pacific and out of phase relationship between upper- and lower-level fluctuations. The role of tropical intraseasonal oscillations on synoptic-scale fluctuations was discussed by Nakazawa (1988). It was suggested that the short period, synoptic-scale convective activities were embedded within the planetary-scale intraseasonal 30-60 day fluctuations (Figure 3).

HIERARCHY OF INTRASEASONAL VARIATIONS

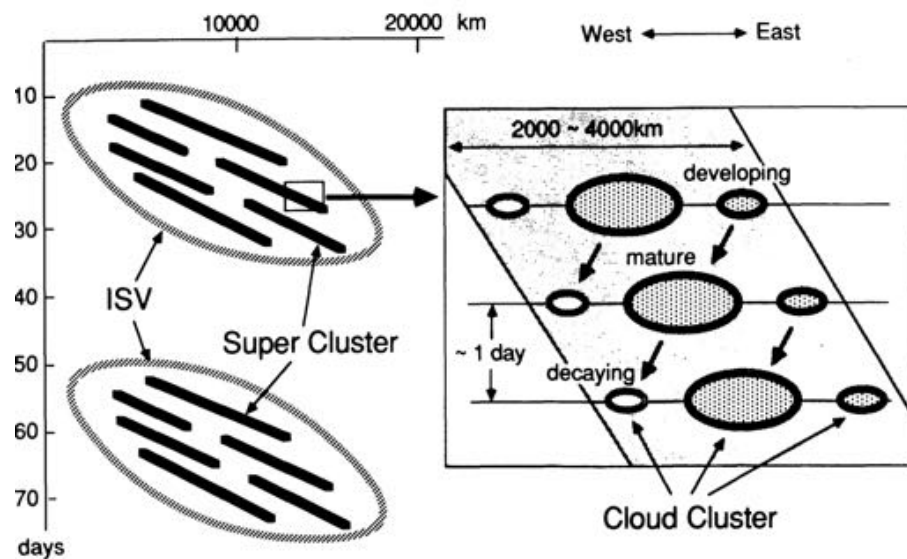


Figure 3 – Schematic diagram showing relationship between Intraseasonal variability (ISV) and convective activities with smaller scales (Nakazawa 1988)

In the summertime western North Pacific region, main features of the large-scale low-level circulation include the Pacific subtropical high-pressure system, trade winds coming from both hemispheres and the low-level monsoon trough (Figure 4). The monsoon trough is a convergence zone which has westerly equatorial winds on the equatorward side and trade wind easterlies further north. Organized deep convection in the monsoon trough region provides favorable

conditions for TC formation (Briegel and Frank 1997, Zehr 1992).

In the region where the westward moving synoptic waves meets the monsoon trough (see Figure 4), it has been suggested that the wave scales are reduced and wave energy is accumulated as they transform into tropical-disturbance type (TD-type) systems (Takayabu and Nitta 1993; Kuo et al. 2001; Sobel and Bretherton 1999). This wave transition is also related to TC genesis (Dickinson and Molinari 2002; Frank and Roundy 2006; Fu et al. 2007; Ritchie and Holland 1999). This will be further discussed in the wave transition section.

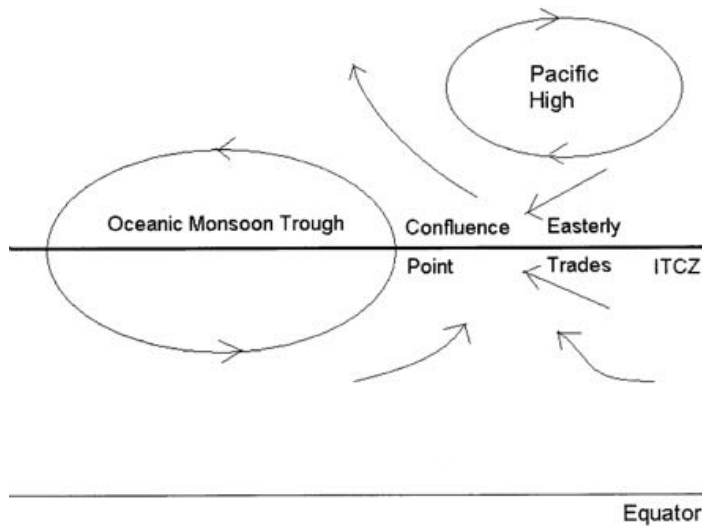


Figure 4 – Schematic of the situation in the summer western North Pacific. (Chan and Evans 2002)

2.2 Shallow Water Equations (SWE)

Alongside with the tropical wave observations, it is also instructive to have a theoretical framework based on which the former can be interpreted. Matsuno (1966) considered a 1-layer shallow water model and found zonally propagating trapped waves along the equator. Expressing zonal wind (or u-wind), v-wind (or v-wind) and geopotential height solutions as (Holton 2004),

$$\begin{pmatrix} u' \\ v' \\ \Phi' \end{pmatrix} = \begin{bmatrix} \hat{u}(y) \\ \hat{v}(y) \\ \hat{\Phi}(y) \end{bmatrix} e^{i(kx - \omega t)} \quad (1)$$

where u' , v' and Φ' represent respectively, perturbations related to the u-wind, v-wind, geopotential height above a motionless mean state. The meridional structure functions for u-wind, v-wind and geopotential height are $\hat{u}(y)$, $\hat{v}(y)$, and $\hat{\Phi}(y)$ respectively. Variables k and ω denote the zonal wavenumber and the angular frequency. Here a motionless mean state indicates that the average value over time and/or space is zero. If the total zonal wind is separated into the basic state and perturbation around the basic state ($u = \bar{u} + u'$), the mean basic state \bar{u} here is assumed to be zero. The wind and geopotential height variables are then related according to the linearized momentum and continuity equations as

$$\begin{aligned}
\frac{\partial u'}{\partial t} - \beta y v' &= -\frac{\partial \Phi'}{\partial x} \\
\frac{\partial v'}{\partial t} + \beta y u' &= -\frac{\partial \Phi'}{\partial y} \\
\frac{\partial \Phi'}{\partial t} + g h_e \left(\frac{\partial u'}{\partial x} + \frac{\partial v'}{\partial y} \right) &= 0
\end{aligned} \tag{2}$$

where $\beta = \frac{df}{dy}$, g = gravitational acceleration and h_e = mean depth of the layer.

Note that in these equations the Coriolis parameter $f = \beta y$ is decided under the beta-plane approximation which is only valid for latitudes within $\pm 30^\circ$ latitude.

After substituting (1) into (2) and by eliminating \hat{u} and $\hat{\Phi}$, the equations become an ordinary differential equation of $\hat{v}(y)$:

$$\frac{\partial^2 \hat{v}}{\partial y^2} + \left[\left(-\frac{k}{\omega} \beta - k^2 + \frac{\omega^2}{gh_e} \right) - \frac{\beta^2 y^2}{gh_e} \right] \hat{v} = 0 \tag{3}$$

The solutions to this equation define the meridional structure of these waves.

The equation can be re-written in a dimensionless form as,

$$\frac{\partial^2 \hat{v}}{\partial \tilde{y}^2} + \left[\frac{\sqrt{gh_e}}{\beta} \left(-\frac{k}{\omega} \beta - k^2 + \frac{\omega^2}{gh_e} \right) - \tilde{y}^2 \right] \hat{v} = 0 \tag{4}$$

where $\tilde{y} = y \cdot (\beta / \sqrt{gh_e})^{1/2}$. Since the equation is intended to describe wave activities around the equator, one expects that $\hat{v} \rightarrow 0$ as $y \rightarrow \infty$. Solutions under the above conditions can only exist if the constant part equals to $2n + 1$, such that,

$$\frac{\sqrt{gh_e}}{\beta} \left(-\frac{k}{\omega} \beta - k^2 + \frac{\omega^2}{gh_e} \right) = 2n + 1 \quad n = 0, 1, 2, 3, \dots \quad (5)$$

Equation (4) therefore can be rewritten as,

$$\frac{\partial^2 \hat{v}}{\partial \tilde{y}^2} + [(2n + 1) - \tilde{y}^2] \hat{v} = 0 \quad (6)$$

whose solutions are given by

$$\hat{v}(\tilde{y}) = v_n D_n(\tilde{y}) \quad (7)$$

where D_n is the parabolic cylinder function (Abramowitz and Stegun 1972) of order n and v_n is a constant coefficient of the mode. The dispersion relationship in (5) between ω and k for each positive integer n (meridional mode) is shown in Figure 5.

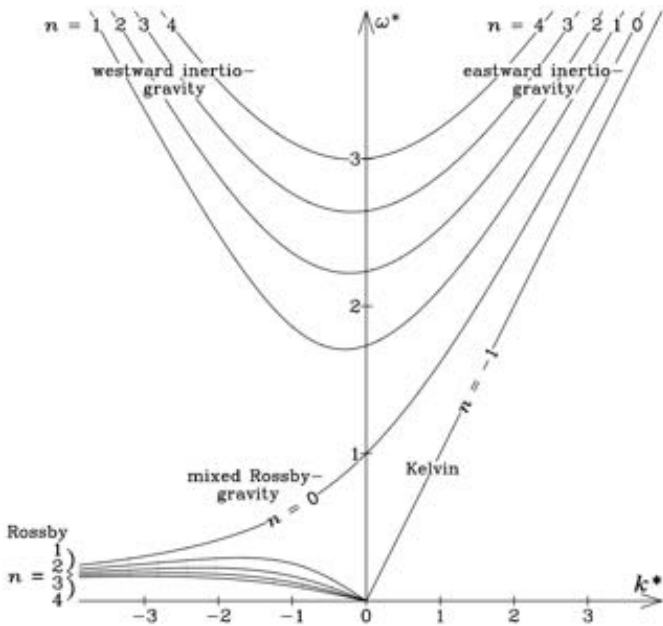


Figure 5 - Relationship between zonal wavenumber ω^* and k^* , which can be expressed in terms of ω and k in (5):
 $\omega^* = \omega / (\beta \sqrt{gh_e})^{1/2}$ and
 $k^* = k (\sqrt{gh_e} / \beta)^{1/2}$. The curves are solutions for (3) up to $n = 4$ except for $n = -1$. (Kiladis et al. 2009)

Given the meridional mode n and specific wavenumber k , solutions for v-wind v' is then solved by (3) and the zonal wind u' is also solved in a similar way, and the horizontal wind distribution can be found. Features of the horizontal wave pattern for different modes can then be used to spot the phenomenon in observational data (with satellite space-time filtering of data). For instance, MRG waves ($n = 0$ and $k = -1$) have the signature of cross equatorial flow, which hence give the strongest meridional flow at the equator (Figure 6c). It is clear from the graph that for the $n = 0$ mode, the wave appears in alternating southerly and northerly flows along the x axis (equator), as observed in Yanai and Maruyama (1966). Note the structural differences between solutions for different modes in Figure 6.

Although the theoretical framework of equatorial waves is clear, it is sometimes difficult to match the theoretical solutions with real observations. This is because, strictly speaking, the SWE solutions apply only to a barotropic and dry atmosphere under no background wind. Deviations from the theory may appear in reality, since water vapor and background wind do exist in our baroclinic atmosphere. Still, spectral signals from observation indicate significant similarities between behavior of synoptic disturbances in the atmosphere and wave solutions to SWE (will be discussed in next sections). Hence, despite the

difference between the model given by the SWE and the real atmosphere, SWE are used to provide a framework to describe synoptic disturbances and as a first step to understand the dynamics of these waves. It should be mentioned that more sophisticated models, such as a two-level equatorial beta-plane model have also been used to study equatorially trapped waves in the atmosphere (Wang and Xie 1996; Xie and Wang 1996).

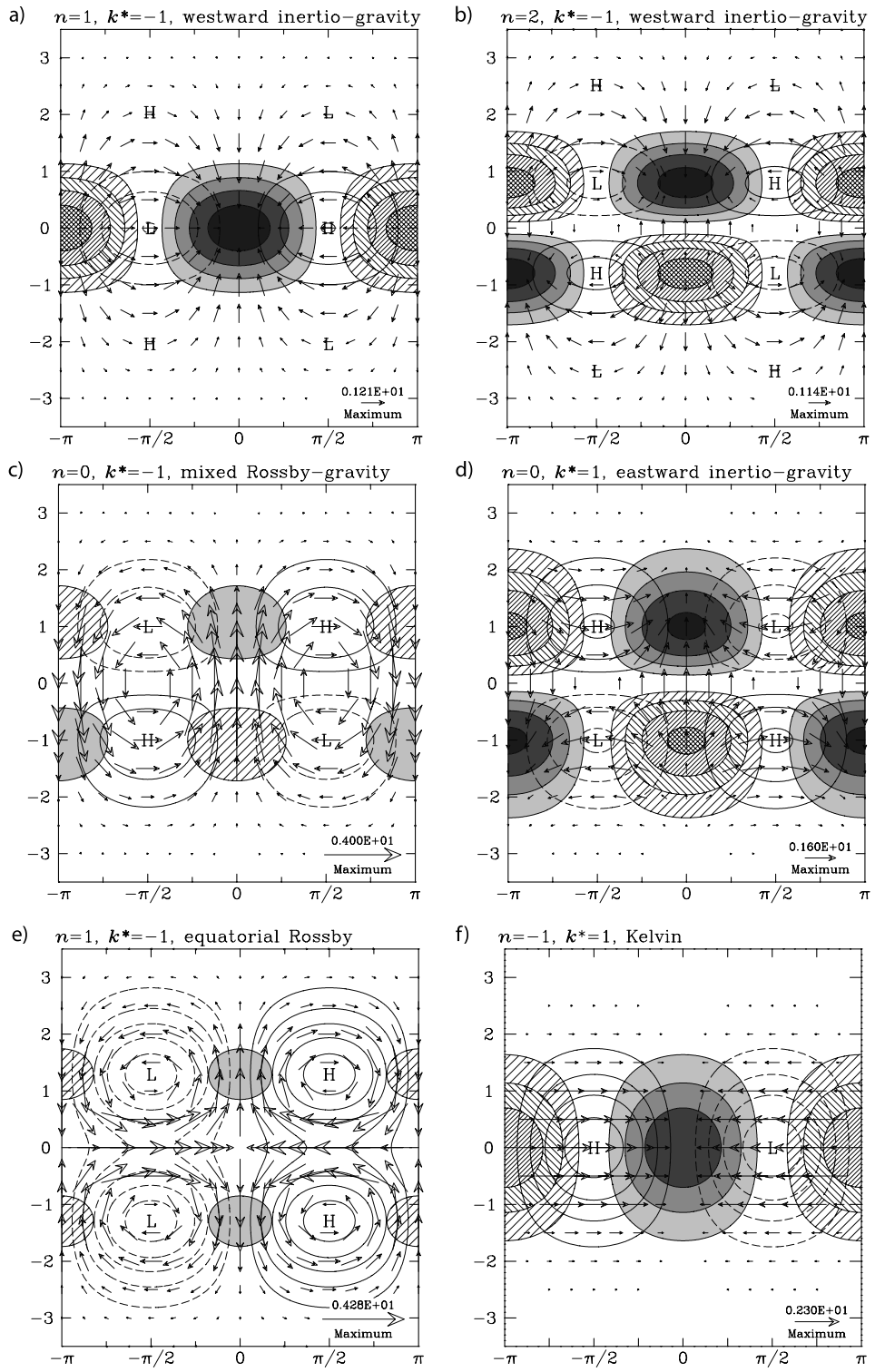


Figure 6 – Horizontal wind distribution for solutions to (3) for different modes (as indicated above each graph). Hatching is for divergence, and shading is for convergence (0.6 unit internal). Unshaded contours are geopotential, with a contour interval of 0.5 units. (see details in Kiladis et al. 2009)

2.3 Wave properties: Spectra and dispersion

As it has been mentioned in section 2.1, early MRG observations (Figure 7) were from upper air station data. Although they allowed examination of wave properties such as the oscillating period, the data can only represent local wave characteristics. Later studies utilized global analysis data to identify features of tropical wave disturbances on a global scale (Nitta and Takayabu 1985; LL90, Liebmann and Hendon 1990; Dunkerton 1993; Takayabu and Nitta 1993; Dunkerton and Baldwin 1995). In LL90, the spectral analysis of 850hPa vorticity over the western Pacific for the summers of 1980-1987 provided characteristics of waves propagating in this region (Figure 8). It is noteworthy that the frequency of spectral peaks depends on the locations of interest. Over 22.5°N 132.5°E, a peak is found corresponding to the 8-9day period and the peak becomes stronger farther to the northwest direction. In fact, waves at different locations were found to have different spectral peaks, indicative of the regional dependence of wave properties. Spectral analysis of Takayabu and Nitta (1993) suggested that these disturbances are most active in the 3-5day period.

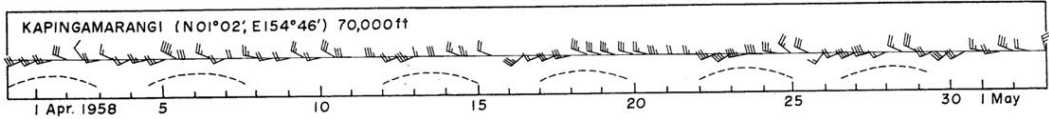
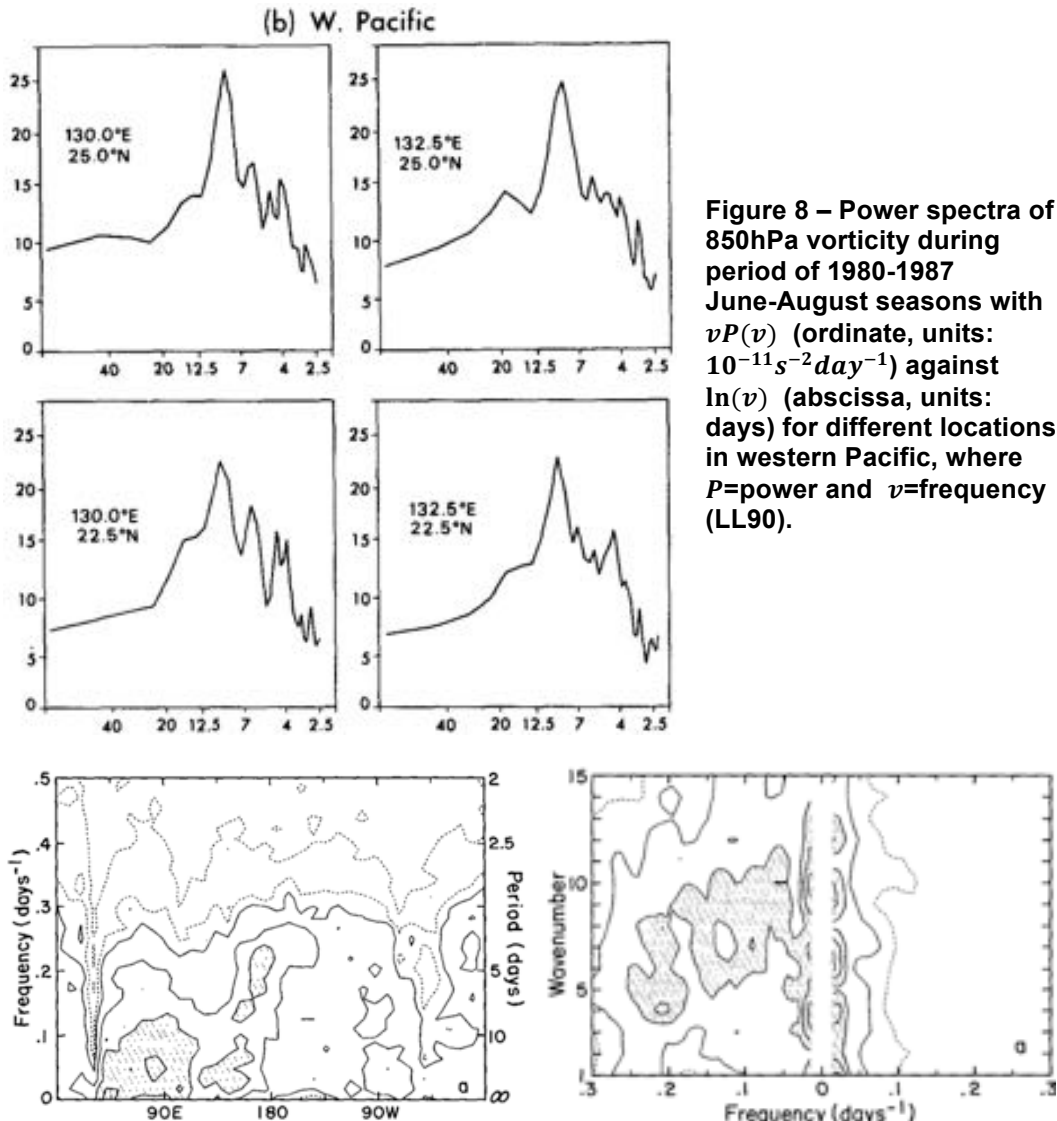


Figure 7 – Time series of wind barb for 1958 April obtained from an upper-air observation station over the central Pacific. Observations of MRG waves were shown in the v-wind components, which appeared alternatively. (Yanai and Maruyama 1966)

Liebmann and Hendon (1990) performed spectral analysis of the 850hPa v-wind and demonstrated how the wave properties could be deduced before performing any data filtering. In their study, the spectra of 850hPa v-wind at different longitudes along the equator were computed (see their Figure 2). It was found that variance corresponding to the 3.5-6day period around 180° can be as strong as that for periods larger than 10 days. Since the power spectrum of u-wind is uniform (see their Figure 2), it was suggested that studying v-wind can provide more information on the zonally varying characteristics of the synoptic-scale disturbances. After the signal was separated into westward and eastward components, westward propagation in the 3.5-6day oscillation period (Figure 9) was found to be dominant. Again this stronger westward propagating signal is not obvious in the zonal wind data.

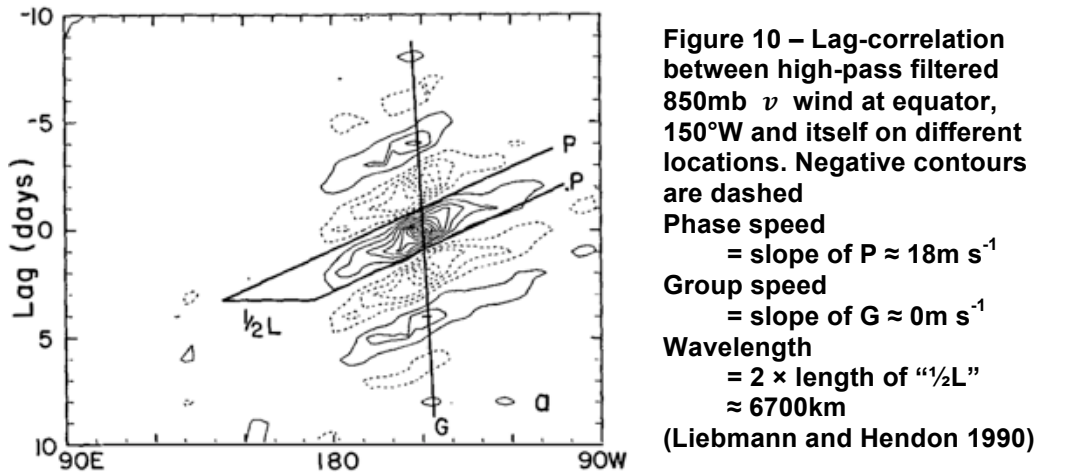


Besides using spectral analysis, some studies (Liebmann and Hendon 1990; Chen and Huang 2009) also made use of lag correlation to extract wave properties from observation data. Liebmann and Hendon (1990) (see Figure 10) performed lag correlations between 850hPa v-wind at a base location (namely, equator, 150°W) with data at other locations at the equator. The same kind of analysis was

then repeated using different longitudes as the base location, so that phase speeds, group speeds and wavelengths at these locations were found. The intrinsic frequencies can then be found as

$$\omega_{int} = \omega_{obs} - \bar{U} \cdot k$$

where ω_{obs} and k are the observational frequencies and wavenumber found in the lag correlation method, \bar{U} is the background zonal wind. Wave properties found are listed in Table 1. Similar summary tables can be found in Gu and Zhang (2001) and Yang et al. (2007b).



Locations		λ (km)	k	v_p (ms^{-1})	\bar{U} (ms^{-1})	v_{int} (ms^{-1})	ω_{int} (cpd)	v_g (ms^{-1})
Liebmann and Hendon (1990)	150°E	~4700	11	-10.5	/	/	~0.15	4
	150°W	~6700	6	-18	/	/	~0.2-0.3	0
Chen and Huang (2009)	180°	/	/	-18.8	-7.1	-11.7	/	/

Table 1 – Wave properties found by lag correlation graphs (see Figure 10) at different locations in the past studies. They are wavelength (λ), wavenumber (k), observed phase speed (v_p), observed group speed (v_g), intrinsic speed (v_{int}), intrinsic frequency (ω_{int}), and average zonal wind (\bar{U}). Some variables are not available.

The relationship between wavenumber and intrinsic frequencies, i.e. the wave dispersion relationship, was found to strongly depend on the longitudinal position (Figure 11). It was suggested that wave properties change from the central to western Pacific (Liebmann and Hendon 1990; Takayabu and Nitta 1993). Wave wavelength, in eastern Pacific was reported to be \sim 6700km (Figure 10) and \sim 3600km in the western Pacific (Liebmann and Hendon 1990). It should be mentioned that values of ω_{int} and k found in the western Pacific were actually outside of the range of (ω, k) values allowed by the MRG wave dispersion curves. Takayabu and Nitta (1993) first named these waves as “TD-type” waves by pointing out the different dispersive properties and also different phase relationship between horizontal structure and convective activity from MRG wave type (will be discussed in next section).

Another wave property that can be determined in dispersion diagram is the equivalent depth h_e (Figure 11). Although it is introduced in SWE as the actual height of the fluid, in application the parameter is considered as the separation constant linking the vertical structure and the horizontal structure as implied in SWE (Lindzen 1967). Another interpretation is that a value of h_e corresponds to a certain vertical wavelength if the stability of the atmosphere is given (Kiladis et al. 2009 their Table 1). Therefore the value of h_e is related to the heating profile

which is implied to provide vertical length scale. Although here discussions are only limited to dry waves and with a resting basic state, different theories have been proposed to model the convectively-coupled equatorial waves and also by assuming different vertical modes (Kiladis et al. 2009). Interests in studying the convectively coupled tropical waves were recently kindled by observations of these waves based on OLR or other proxy data for convection, which will be discussed in the next section.

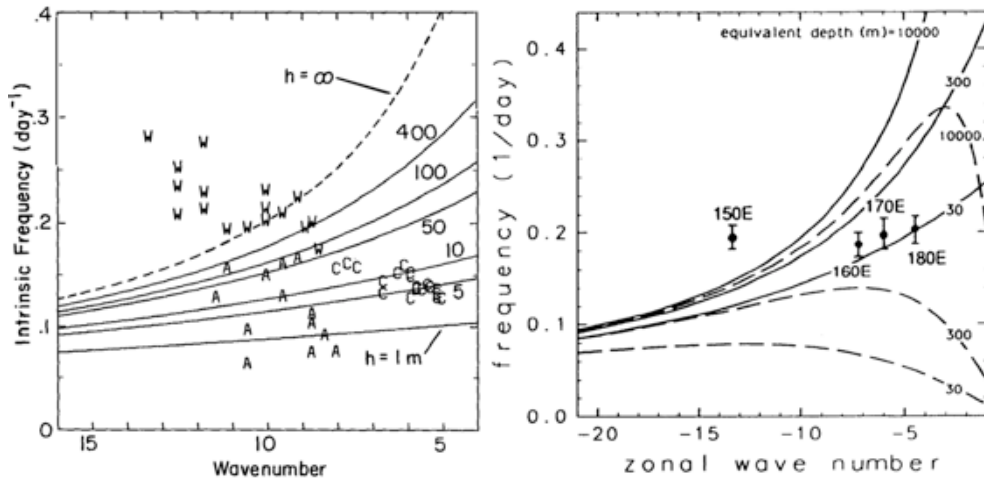


Figure 11 – Intrinsic frequencies (units: day⁻¹) versus zonal wave number for different locations in the equatorial area.

Left: Obtained from lag correlations and composites on activities found in convection-proxy data. "W" signs are for Indian and western Pacific oceans (65° - 145° E); "C"s for central Pacific (180° - 90° W), "A"s for Atlantic (65° W- 5° E). Dashed lines are the curves for Rossby waves (Liebmann and Hendon 1990)

Right: Obtained from composite maps associated with convective activities. (Takayabu and Nitta 1993)

Lines: the theoretical dispersion relationships for MRG waves with different equivalent heights (units: m).

2.4 *Observing convectively coupled MRG waves*

As mentioned in section 2.1, part of the variance of convective activity in the tropical area is associated with wave-like disturbances. Convectively coupled equatorial waves can therefore be studied with convection data. The most extensively used proxy data for convection is the OLR data (WK99, Wheeler et al. 2000), or infrared equivalent blackbody temperature data (Takayabu 1994a) from satellites. WK99 made use of OLR data to study the spectral properties of these convectively coupled equatorial waves. The OLR dataset was from the National Oceanic and Atmospheric Administration (NOAA) polar-orbiting satellites with a resolution of $2.5^\circ \times 2.5^\circ$, which allowed examination of waves with high wavenumber. As the ITCZ is providing precipitation-favorable conditions in the Tropics, it is reasonable to expect a red-noise background in the OLR spectrum near the equator. By attributing the red-noise signals to the random and non-periodic variations of deep convection, WK99 divided the symmetric (not shown here) and antisymmetric OLR components of the equatorial data by the background spectrum (not shown here) and found distinct dispersion curves corresponding to different modes from SWE solutions (Figure 12).

These spectral peaks showed the preferred spatial and temporal scales for each of the wave mode. For convectively coupled MRG waves, the dominant

period is 3-6day and the equivalent depth was found to be 12-50m in WK99 (comparable to values of 12-30m by Takayabu 1994a). TD-type disturbances signals were also observed in the symmetric OLR spectrum. These preferred values, which are an order of magnitude smaller than that for free wave response to deep convective heating, were considered to be related to coupling between wave dynamics and cumulus convection / diabatic heating profile (Takayabu 1994a; Kiladis et al. 2009).

WK99 also conducted the cross-spectrum analysis based on OLR and deep layer-tropospheric temperature data. In particular, radiance measurements from microwave sounding unit (MSU) for the lower-tropospheric temperature (labeled as MSU23, between surface and 300hPa) and upper-tropospheric temperatures (labeled as MSU34, between 500 and 100hPa) were examined in relation to convectively coupled equatorial waves. The antisymmetric cross spectrum between upper-level and lower-level temperatures indicated that almost-in-phase westward travelling disturbances are vertically coherent (upper panel of Figure 13). The strongest signals were found at around $k=-5$ with a period of 5-10day. They do not appear in the same domain as the peaks in the cross spectrum between OLR and lower tropospheric temperatures (lower panel of Figure 13), in which the strongest coherence was found with $h_e=25m$, $k=-1$ and a period of

about 4day. The cross spectrum between OLR and lower tropospheric temperature is similar to the OLR spectrum itself (Figure 12), indicating an interaction between the tropical tropospheric temperature and convection associated with these waves. Here wave dynamics and OLR share the common wavenumber-frequency domain where the equivalent depths are about to 25m. The phase difference (as shown by arrow direction in the cross spectrum) indicated that OLR is leading the lower tropospheric temperature phase relationship, thus implying a preferred phase relationship between convection and dynamics.

Based on the locations of spectral peaks for MRG waves in WK99, Wheeler et al. (2000) filtered the OLR data in the wavenumber-frequency space to retain MRG signals only (Figure 14, domain enclosed with thick lines and marked with “MRG”). Where the filtered OLR variance is the largest (black cross in upper panel of Figure 15), the wave amplitudes are further determined by the 14day running averaged variance (time series of lower panel of Figure 15). They found that MRG waves are most active during August to November. The time series of filtered OLR variance then can be used in regression to find the corresponding dynamical features, which will be discussed in the next section.

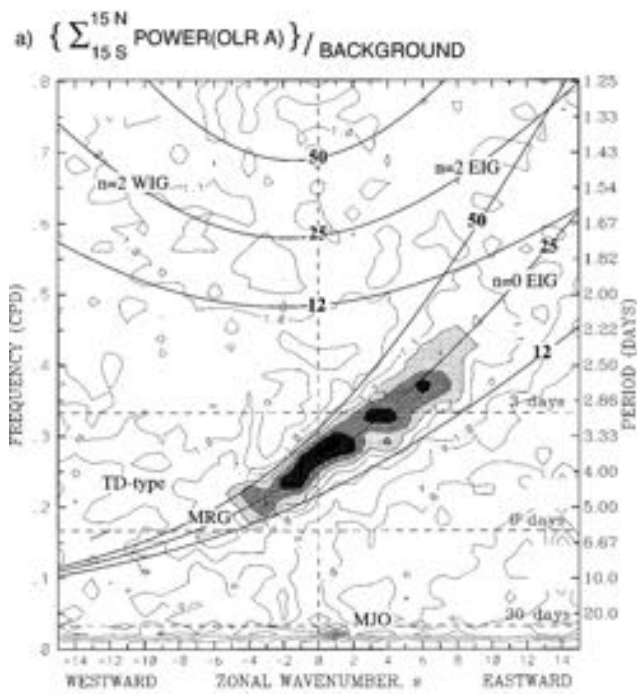


Figure 12 – The antisymmetric (around equator) OLR wavenumber-frequency power divided by a background spectrum (not shown).

Black lines are the dispersion relationships marked by equivalent depths of 12, 25, 50m for different wave modes (such as MRG waves).

**Contour interval is 0.1.
Shading area is greater than 1.1.
(see details in Wheeler and Kiladis 1999)**

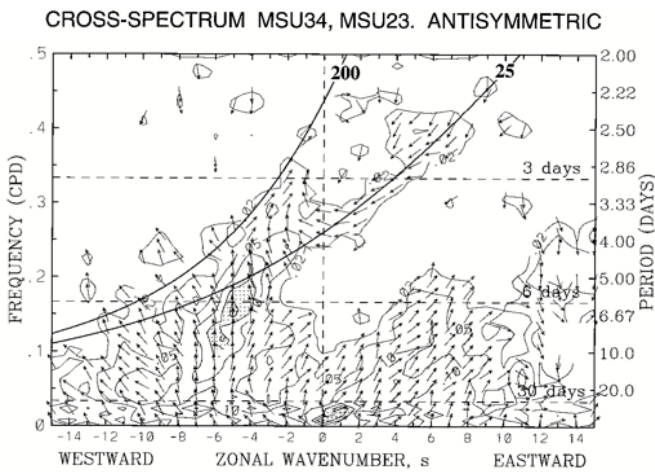
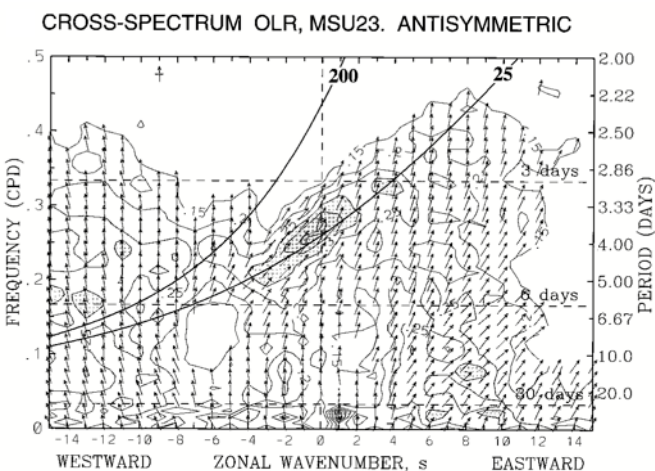


Figure 13 – Coherence square (contours) and phase (vectors) of cross-spectra between antisymmetric MSU34 and antisymmetric MSU23 (upper panel), and between antisymmetric OLR and antisymmetric MSU23 (lower panel) for the period 1979-1993 and summed between 15°S and 15°N.

**Contour interval is 0.05 and an additional contour of 0.02 is added in upper graph.
Upward pointing of vectors indicates in phase relationship.**

**MRG dispersion curves with equivalent depths of 25m and 200m are drawn here.
(see details in WK99)**



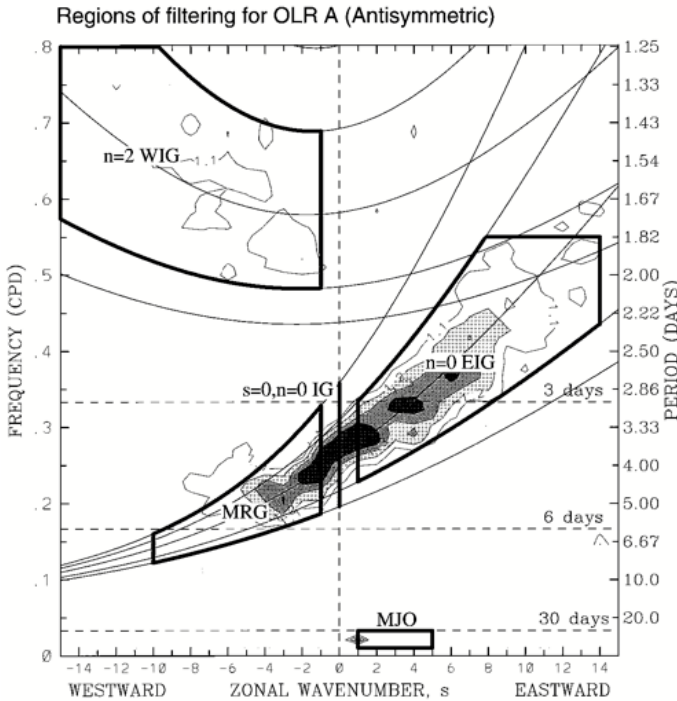


Figure 14 – Similar to Figure 12 except contours less than 1.1 and greater than 1.4 are removed.

Dispersion curves shown are for $h_e = 8, 12, 25, 50$ and 90m.

The enclosed areas indicate the wavenumber-frequency domains used in OLR filtering.

(see details in Wheeler and Kiladis 1999)

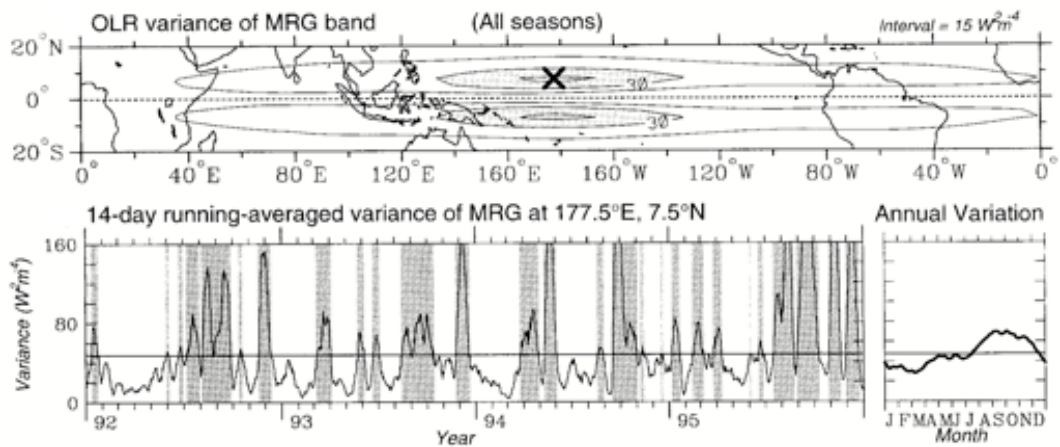


Figure 15 – Distribution of variance of MRG wave filtered OLR (upper panel). Contour interval is $15(\text{Wm}^{-2})^2$. Cross sign denotes the position with highest variance. The 14-day running MRG band variance at the cross location (177.5°E , 7.5°N) and annual variation are shown (lower panel). Thin lines are the average values. The MRG wave wavenumber and frequency domain is defined in Figure 14. (Wheeler et al. 2000)

2.5 Dynamical structure of MRG waves and associated convective activities

As mentioned in the previous sections, the wind patterns associated with the

tropical waves can be derived analytically from SWE. To extract this circulation structure from observations, a number of studies (Nitta and Takayabu 1985; Liebmann and Hendon 1990; Takayabu and Nitta 1993; Dunkerton and Baldwin 1995; Wheeler et al. 2000; Kiladis et al. 2009) have attempted various approaches, such as linear regression (Wheeler et al. 2000; Kiladis et al. 2009) or composite maps based on selected cases (Nitta and Takayabu 1985; Takayabu and Nitta 1993).

Time series based on either filtered OLR at a certain base point (Wheeler et al. 2000) or the principal components (PC) of empirical orthogonal function (EOF) found based on bandpass-filtered OLR (LL90) was chosen to represent the magnitude of wave activity. This time series was then used to perform linear regression for other parameters in all other grid points. This way, the wind field distribution associated to variation of the reference time series can then be found. These regressed wind patterns were found to be consistent with those predicted in shallow water theory (see Figure 6), where there are alternating v-wind anomalies crossing the equator for MRG waves. It was also found that negative OLR regions (indicative of strong convective activity) generally coincide with the low-level convergence centers (Wheeler et al. 2000) as predicted for MRG waves (Figure 16). The agreement between the observed wind circulation patterns from

regression and the one predicted by theory gives strong evidence of the existence of MRG waves over equatorial locations in the troposphere. It also indicates that these waves are coupled with convection. The regressed wind field from another study (Kiladis et al. 2009) showed a similar pattern west of the dateline (Figure 17). Note that the whole horizontal wind field moved away from the equatorial area in the western North Pacific and over which positions of active convection (negative OLR) became more in phase with positive low-level vorticity anomalies. Takayabu and Nitta (1993) found similar results in composite maps of circulation related to convective activities at different reference longitudes (Figure 18). The convectively coupled waves in the far western Pacific, therefore, resembled the so-called TD-type disturbances (Takayabu and Nitta 1993) (Figure 19).

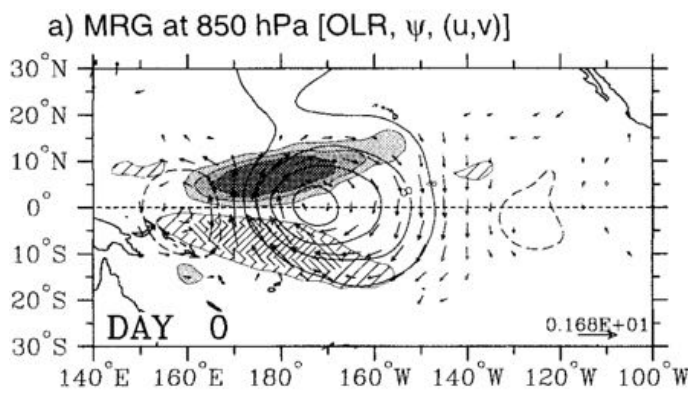


Figure 16 – Maps of regressed OLR (hatching positive/shading negative), 850hPa streamfunction (contours), and 850-hPa wind (vectors) anomalies associated with the OLR variation of the convectively coupled MRG wave (base point 7.5°N, 177.5°E) on day 0. (see details in Wheeler et al. 2000)

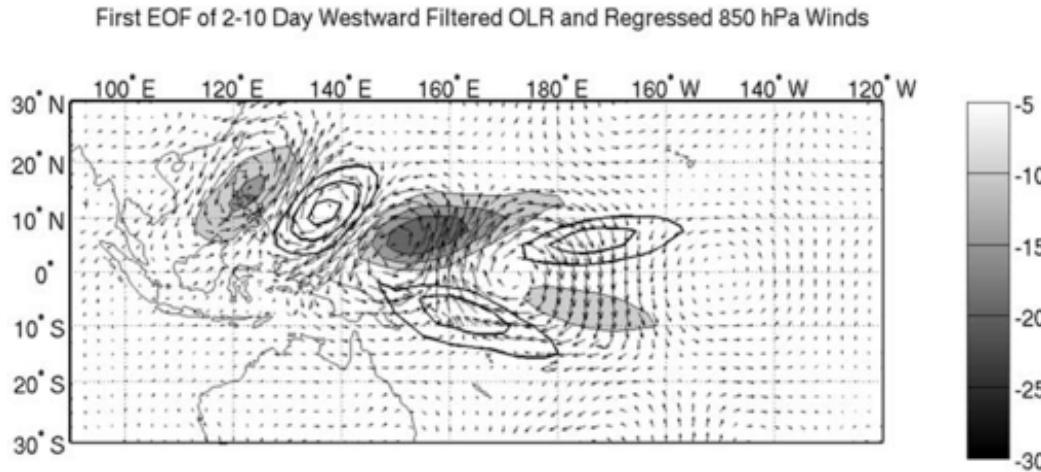


Figure 17 – First empirical orthogonal function (EOF) of 2-10 day westward filtered OLR using 30°N-30°S data (negative shaded) and regressed 850hPa wind from 1979 to 2006. (see details in Kiladis et al. 2009)

Using satellite blackbody temperature data as a proxy for convection, Pires et al. (1997) also showed that placement between convection anomalies and 3-6day bandpass-filtered 850hPa wind agreed with the theoretical MRG wave structure. Based on a case study, they found that convection activity was consistent with the anti-symmetric structure of divergent field (see shading and hatching in Figure 6c).

As mentioned earlier (Figure 17), active convection becomes in phase with the low-level cyclonic center when synoptic-scale waves moved westward into the western Pacific, implying even stronger convectively coupling (Takayabu and Nitta 1993; Wheeler et al. 2002; Dickinson and Molinari 2002; Tam and Li 2006; Serra et al. 2008). However, past studies focusing on the dynamical structures (Takayabu and Nitta 1993; Wheeler et al. 2000; Kiladis et al. 2009) relied on the

use of convection proxy data as the starting point, either by linear regression or from composite map, to find synoptic wave signals. While it is sensible to pay attention to the convectively coupled features of the synoptic waves in the Pacific Ocean, there might be an uncoupled preceding stage, or even a dry stage, which can be difficult to find with convection proxy data. Also, wave variance defined based on activities at a single location or PC of a certain pattern cannot reflect variations of wave strength at different locations. Nevertheless, systematic examinations of spectral properties and dynamical structures of different modes of convectively coupled tropical waves can be carried out with OLR data, despite the drawbacks just mentioned here.

BPF-TBB & Wind 850hPa JJA 1980-89(ex84)

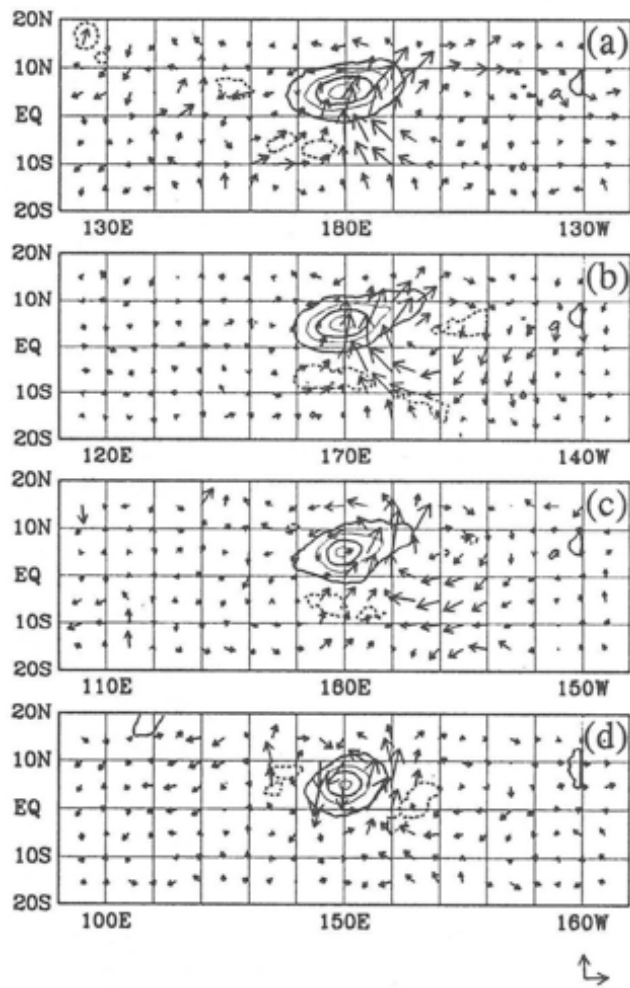


Figure 18 – Horizontal composites of blackbody temperature (contour, viewed as active convective activities) and 850hPa bandpass filtered wind centered at 5°N, (a) dateline, (b) 170°E, (c) 160°E and (d) 150°E.

Contour interval is 2.5K and reference vector indicates 0.6 m s^{-1} .

(Takayabu and Nitta 1993)

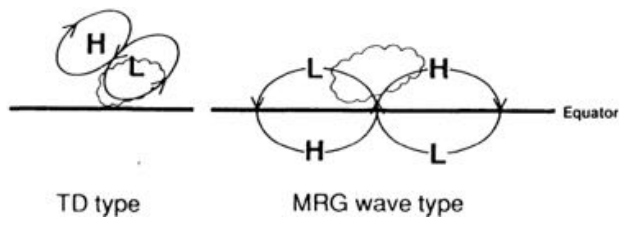


Figure 19 – Schematics showing convection arrangement (cloud icon) with low level dynamical circulations. H/L are for highs and lows anomaly regions. (Takayabu and Nitta 1993).

- Although SWE can provide a framework for understanding the equatorially waves, it is reasonable to extend our analysis in vertical dimension because
- i) convection, which is intimately related to vertical atmospheric motions, is observed to be associated with those waves (already mentioned),
 - ii) vertical wind shear changes from westerly in central/eastern Pacific to

easterly in western Pacific (which will be discussed), and

iii) upper-level structures are observed to be associated with the development of lower-level disturbances (Briegal and Frank 1997; Nitta and Takayabu 1985; Dunkerton and Baldwin 1995). Nitta and Takayabu (1985) also suggested that upper-level coupling exists between upper-level vortices in higher latitudes (known as upper-level Mid-Pacific trough) and lower-level wave disturbances (their Figures 8 and 9).

Early studies in the 1960s-1970s reported vertical tilting of synoptic tropical waves (Yanai et al. 1968; Reed and Recker 1971). The tilting with height (Figure 20 and Figure 21) was found to be eastward in the central Pacific and decreases as the waves move into the western Pacific until there is very little tilting or even with a slight westward tilt (LL90; Takayabu and Nitta 1993; Maloney and Dickinson 2003, Yang et al 2007a). It was suggested that the vertical structures of these disturbances were sensitive to the vertical shear of background zonal wind (Holton 1971; Wang and Xie 1996) – easterly shear in the monsoon region western Pacific gives rise to the westward tilt. As seen in Figure 21 (a), low-level disturbances were stronger in the western part of the Pacific and positive vorticity was more in phase with low-level upward motion, implying that the synoptic waves signals were stronger in the west in the low levels and possibly due to the

stretching effect by the upward motion there. Vertical warming in the upper levels (Figure 21d) also coincides with rising motion (Figure 21c), indicating energy conversion from eddy potential available energy to eddy kinetic energy (west of 120°E). Energy conversion involved in the wave dynamics will be discussed in the energetics section.

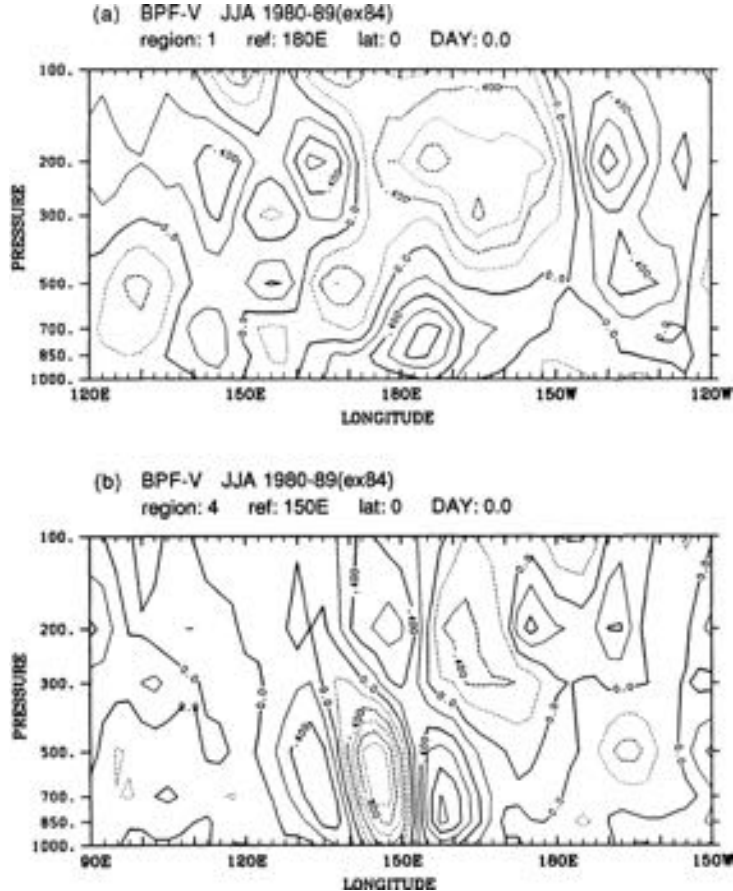


Figure 20 – Vertical composite of bandpass-filtered v-wind at equator for (a) dateline and (b) 150°E.

Negative values are dashed and contour level is at 0.2m s⁻¹.

(Takayabu and Nitta 1993)

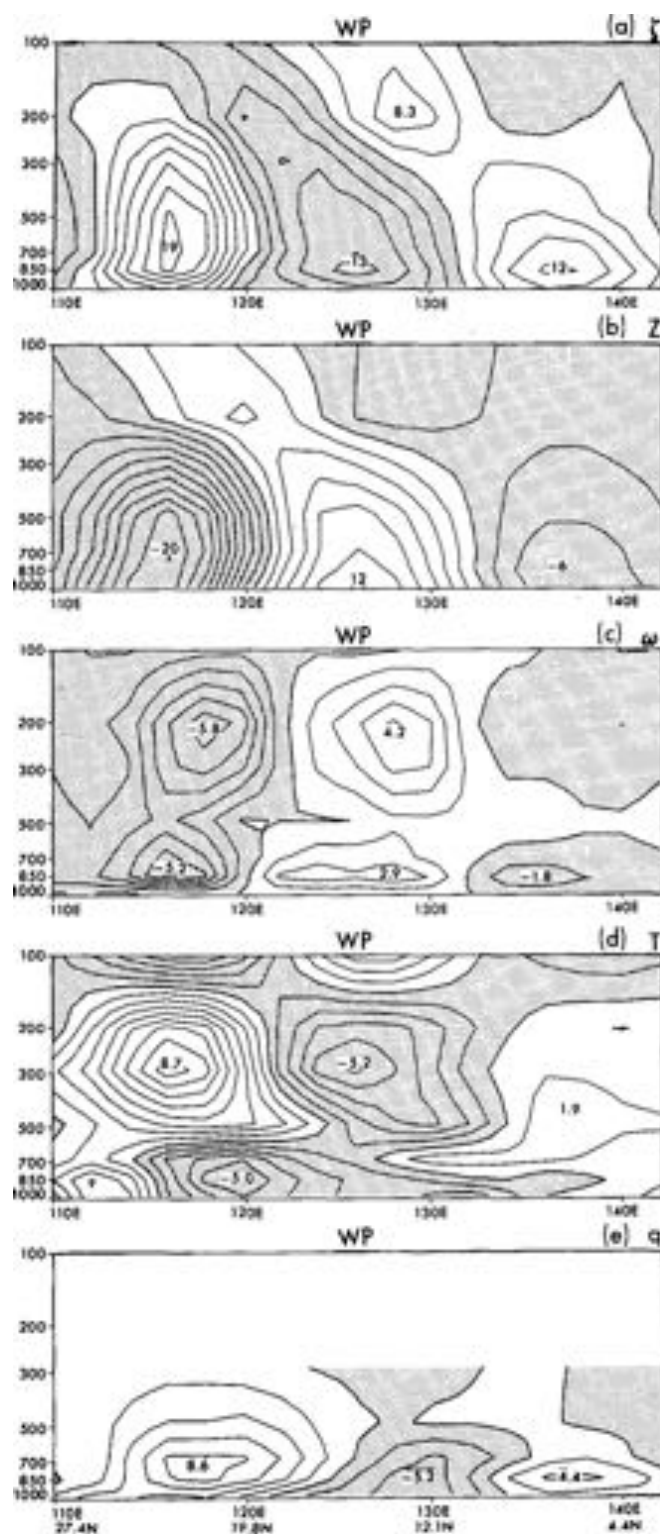


Figure 21 – Vertical cross-sections of composite (a) relative velocity, (b) geopotential height, (c) pressure velocity, (d) temperature and (e) specific humidity of the western Pacific perturbations.

Negative values are shaded and contour levels are $3 \times 10^{-6} \text{ s}^{-1}$, 2 gpm , $1 \times 10^{-2} \text{ Pa s}^{-1}$, 0.1°C and 2×10^{-4} respectively.

Composites are produced from EOF method with synoptic-scale bandpass-filtered data.

Locations of the cross-sections shown under (e).

(LL90)

2.6 Wave energetics

The eddy kinetic energy (EKE) balance equation can be used to study processes involved in wave dynamics. The EKE K' is defined as,

$$K' = \frac{1}{2} (\overline{u'^2} + \overline{v'^2}) \quad (8)$$

where u' and v' are the perturbation wind fields. Rate of change of EKE is then given by (Maloney and Hartmann 2001; Maloney and Dickinson 2003),

$$\begin{aligned} \frac{\partial K'}{\partial t} &= -\overline{u'v'} \frac{\partial}{\partial y} \bar{u} - \overline{u'v'} \frac{\partial}{\partial x} \bar{v} - \overline{u'^2} \frac{\partial}{\partial x} \bar{u} - \overline{v'^2} \frac{\partial}{\partial y} \bar{v} \\ &- \frac{R}{p} \overline{\omega' T'} - \bar{V} \cdot \nabla \bar{K}' - \bar{V}' \cdot \nabla \bar{K}' - \nabla \cdot (\bar{V}' \Phi') + \text{Dissipation} \end{aligned} \quad (9)$$

where T' = temperature perturbation, Φ' = geopotential perturbation, ω' = vertical pressure velocity perturbation, R = gas constant for dry air ($286.7 \text{ J K}^{-1} \text{ kg}^{-1}$), p = pressure and V = perturbation wind field in vector form (ω should be not confused with angular frequency ω mentioned in section 2.2). The sum of the first four terms is referred to as the barotropic conversion. They explain EKE generation by drawing energy from change in mean flow. The fifth term is energy conversion from eddy available potential energy. The first five terms are considered to be the real sources of EKE generation; the rest of the terms are the

advection of EKE by the mean and perturbation flow, the convergence of eddy geopotential flux and dissipation processes such as friction in the lower boundary.

The equation can be used to analyze influences from different dynamical or thermodynamical process on the maintenance of tropical disturbances (Lau and Lau 1992; Maloney and Hartmann 2001; Maloney and Dickinson 2003; Hsu et al. 2011; Ha et al. 2013). After tracking the synoptic-scale wave signals in the western Pacific, Lau and Lau (1992) were able to find that the barotropic conversion – EKE generation from mean flow – was important in the low levels (Figure 22a). In other words, eddies were drawing energy from kinetic energy of the mean flow. They also found that anomalous warming, which is in phase and collocated with upward vertical motion, leads to EKE generation in the upper levels (Figure 22b). Baroclinic conversion in upper levels and barotropic conversion in low levels were also found in Maloney and Dickinson (2003) for TD-type disturbances (Figure 24). It is also noteworthy that EKE generation area in the vertically averaged composites of barotropic conversion (Figure 23c) coincides with the climatological TC genesis locations.

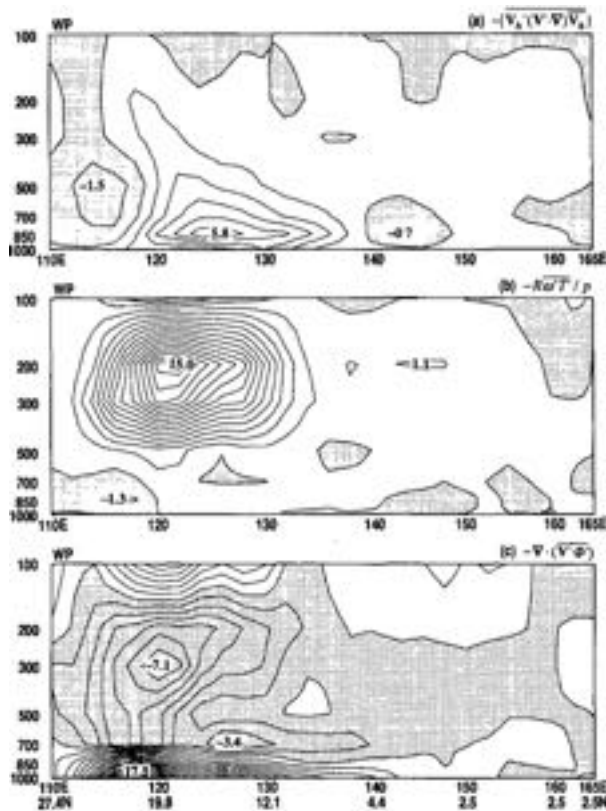


Figure 22 – Vertical cross-sections of different terms in eddy kinetic energy balance equation (9) :
(a) barotropic conversion,
(b) conversion from eddy available potential energy and
(c) convergence of eddy geopotential flux.

Composites are produced from EOF method with synoptic-scale bandpass-filtered data.

Negative values are shaded and the contour interval is $1 \times 10^{-5} \text{ m}^2 \text{ s}^{-3}$

(see details in Lau and Lau 1992)

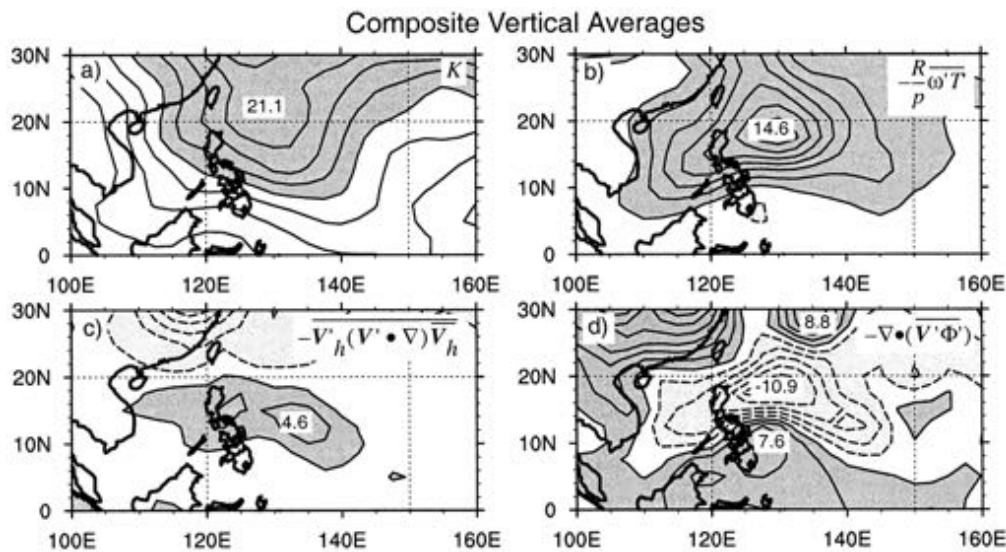


Figure 23 – Vertically averaged composites of eddy kinetic energy balance terms for TD-type disturbances: (a) EKE, (b) baroclinic conversion, (c) barotropic conversion and (d) convergence of geopotential flux
Negative contours are dashed. Contour intervals for (a) are $2.0 \text{ m}^2 \text{ s}^{-2}$ starting from value of 1 and values greater than 12 are shaded. Contour levels for (b), (c), (d) are $2.0 \text{ m}^2 \text{ s}^{-2} \text{ day}^{-1}$ starting from value of 1 and values greater (less) than 1 (-1) are dark (light) shaded. (Maloney and Dickinson 2003)

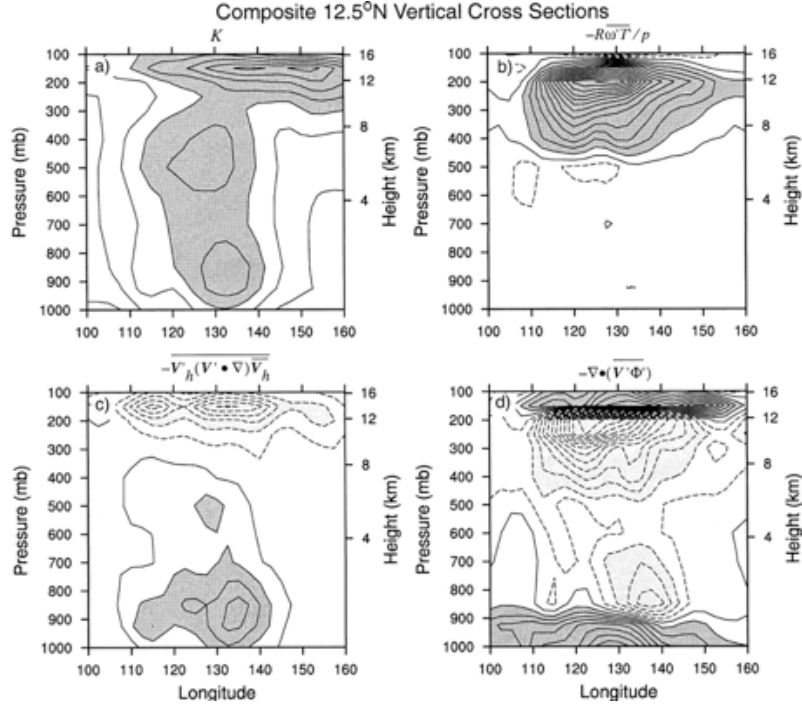


Figure 24 – Vertical composites of eddy kinetic energy balance terms for TD-type disturbances: (a)EKE, (b) baroclinic conversion, (c) barotropic conversion and (d) convergence of geopotential flux. Negative contours are dashed. Contour intervals for (a) are $4.0\text{m}^2\text{s}^{-2}$ starting from value of 2 and values greater than 12 are shaded. Contour levels for (b)(c)(d) are $4.0\text{m}^2\text{day}^{-1}$ starting from value of 2 and values greater (less) than 6 (-6) are dark (light) (see Maloney and Dickinson 2003).

2.7 Wave transition, energy accumulation and TC genesis

As it has already mentioned in last sections, the dispersive characteristics (Takayabu 1994a; WK99) and the dynamical features (Takayabu and Nitta 1993; Wheeler et al. 2000) both implied the co-existence of and transformation between the MRG waves and TD-type waves in the western Pacific due to spatial variation of the background flow. Since TD-type disturbances are off-equatorial wave trains and have convection organized associated with their low-level vortices (Figure 19), they can be the vortex “seeds” for TCs. In other words, the wave type

transformation could influence the TC activity and reviewing the processes involved is necessary. Dickinson and Monlinari (2002) investigated a 1987 case and found that the transformation of MRG into TD-type waves was closely related to TC genesis in the vicinity (Figure 25). Frank and Roundy (2006) also found that MRG waves tend to provide favorable conditions for TC genesis. Composite analysis relative to genesis location showed that the preferred genesis location is over the area of northeasterly anomaly flows and western edge of cyclonic circulation.

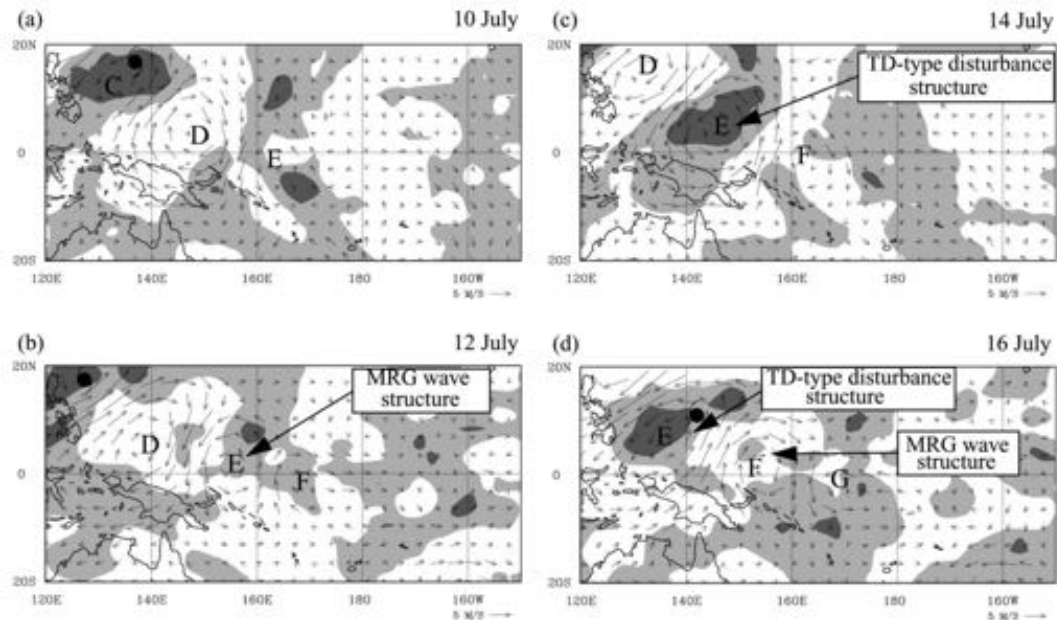


Figure 25 – 6-10-day filtered wind vectors (ECMWF analyses) on the 315-K surface plotted with 6-10-day OLR (negative in shading) at 0000 UTC of (a) 10 July, (b) 12 July, (c) 14 July, and (b) 16 July 8 in 1987. Tropical Strom Thelma in (a)(b) and Tropical Storm Vernon in (d) are shown in hurricane symbol (see details in Dickinson and Monlinari 2002).

Background flow where the waves are embedded does not only affect the

wave structures, it could also be related to transport of wave energy. Sobel and Bretherton (1999) and Kuo et al. (2001) argued that the zonal wind convergence could amplify wave energy and reduce the wave scale through a wave accumulation process. Sobel and Bretherton (1999) analyzed reanalysis data and found that the wave energy growth rate, which reflected the rate of wave accumulation, is dominated by the convergences of low-level mean flow. This was suggested to be the initiation mechanism for synoptic-scale disturbances in this region. Kuo et al. (2001) used a β -plane non-divergent barotropic model to show that wave scale contraction and energy accumulation need a confluent background flow, nonlinear dynamics, beta effect, and large-scale convergence. It was also showed that linear dynamics could not explain energy increase after initiation stage of wave development. Another study (Tam and Li 2006) showed wave accumulation is important for the growth of low-level synoptic disturbances in the western North Pacific based on reanalysis data.

Besides observational studies, some regional model studies with full physics and dynamics also focused on the wave accumulation issue. Li et al. (2003) showed that in the model environment, a new TC with realistic dynamic and thermodynamic structures can form either in the wake of a mature TC due to Rossby wave energy dispersion or in the monsoon confluence zone due to energy

accumulation of easterly waves. Done et al. (2011) explored the issue by simulating the entire 2005 hurricane season in Atlantic. By comparing the values of $\frac{\partial U}{\partial x}$ between different months, they showed that the longitudinal gradient of zonal wind $\frac{\partial U}{\partial x}$ is more negative in August and September where the easterly waves experienced strong modification via wave accumulation and more TCs formed in the same area of the negative $\frac{\partial U}{\partial x}$ (between 60°W and 20°W).

Ching et al. (2010) studied the influence of multi-scale oscillations on TC activities (Figure 26). A space-time filtering of OLR and 850hPa wind fields is performed in order to identify the Madden-Julian Oscillation (MJO) (with typical eastward wavenumber of 0-5 and a period of 30-90 days), Rossby waves (westward wavenumber of 1-10 and a period of 10-40 days) and MRG-TD waves (westward wavenumber of 0-14 and a period of 2.5-10day). By studying the structure and evolution of these waves during the formation of 5 TCs in 2004 June, they found that some “seeding vortices” for TC genesis can be attributed to Rossby waves and MRG-TD waves during an active MJO period. This result agrees with that of Zehr (1992) which stated that low-level cyclonic vortices are important precursors to TC genesis. A later TC case study based on numerical models examined the precursor signal of Typhoon Manyi (2001) (Xu et al. 2014). They found that typhoon genesis in their model can be eliminated by removing

either the northwest-southeast-orientated synoptic-scale wave train or the intraseasonal oscillations (Figure 3). In other words, for this type of TC genesis, both intraseasonal oscillations and the synoptic-scale wave trains can play a crucial role.

Zhou and Wang (2007) traced back the disturbances that finally became Typhoon Nanmadol in 2004 and found that they were originally upper-level MRG waves. They showed that near the dateline, in the presence of prevailing easterly shear, the wave train in the upper troposphere can travel downward, and the phase difference between low-level low and cyclonic vortex as well as the vertical tilting disappeared. This is consistent with Wang and Xie (1996) who showed that easterly vertical wind shear tends to trap and amplify MRG wave signal in the lower troposphere.

The western Pacific background flow also plays a very important role in shaping synoptic-scale wave structures (see section 2.5) and wave energy accumulation. If wave type transformation is in fact related to TC formation, the interannual variation of the wave transformation will also be related to TC seasonal activity. This will be discussed in the next section.

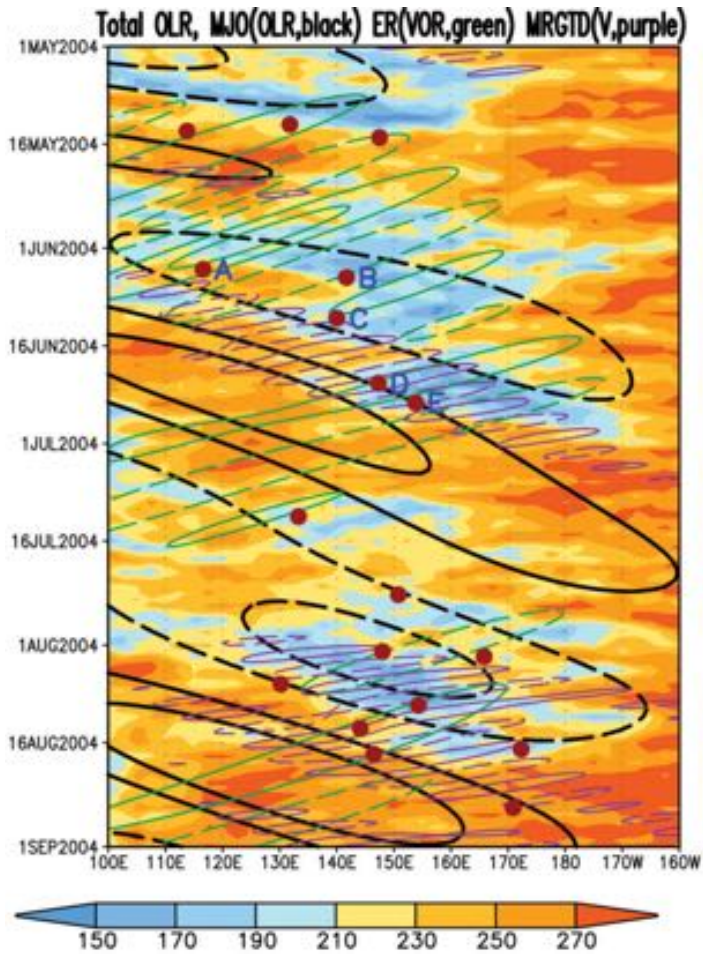


Figure 26 – Hovmöller diagram of the unfiltered OLR (shaded) from May 1st to September 1st 2004. Black contours: filtered OLR for MJO averaged from 5°S to 5°N (interval=10 Wm⁻¹). **Green contours:** 850hPa filtered vorticity for $n = 1$ Rossby waves averaged from 5°N to 15°N (interval= $3 \times 10^{-5} \text{ s}^{-1}$). **Purple contours:** 850hPa filtered v-wind for MRG-TD waves averaged from 5°N to 15°N (interval=1.5 ms⁻¹). **Solid (dashed) contours** represent positive (negative) anomalies. Dots indicate the formation longitude and time of TCs. (Ching et al. 2010).

2.8 Interannual variation of MRG waves

Chen and Huang (2009) investigated the interannual variation of wave transition from MRG to TD-type waves by comparing locations of wave transition, locations of the easternmost edge of the monsoon trough and the western Pacific thermal state (Figure 27). The location of the monsoon trough

edge, viewed as the place where background flow changes, was found to have similar interannual variation as the location where MRG waves transformed into TD-type disturbances. Using lag-correlation method, they defined the wave transition position as the place where synoptic-scale activities moved away from the equator (their Figure 3). Their results could be interpreted as relating the location of background flow changes and the location where the 3-6day disturbances moved poleward away from the equator. Since drifting away from the equator is one of the features of TD-type waves, other features such as wavelength and frequency, that truly representing this type of waves, should be taken into consideration if the involved physical processes are studied.

They also found that the western Pacific thermal state, as represented by subsurface ocean temperature anomalies (SOTA) over the region of 0°-16°N and 125°-165°E, and the monsoon trough position are related. During years in which the monsoon trough retreats (extends) to the west (east), SOTA is above 1.5°C (below -1.5°C).

It was speculated that the variation of the western Pacific thermal state could exert thermodynamic impacts on tropical waves and the monsoon trough circulation and hence the tropical wave activities. Here the region, where subsurface ocean temperature is extracted, is the same region of the monsoon

trough (see their Figure 6). Although it is quite reasonable to relate the wind field situation and the ocean temperature in mostly the same region, it is difficult to tell which one is the cause and which one is the effect. Further studies are needed for investigating the cause of the interannual variations of synoptic-scale waves.

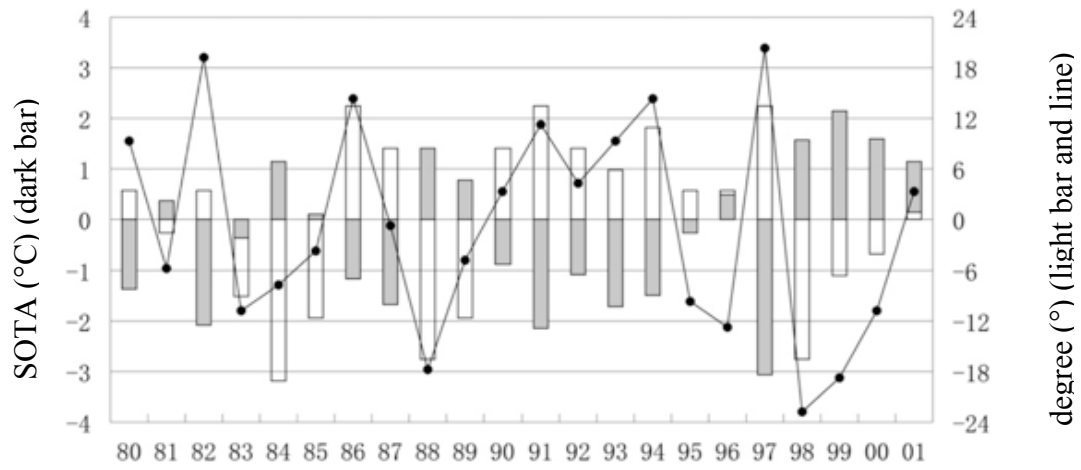


Figure 27 – Interannual anomaly of the longitude ($^{\circ}$) of the easternmost edge of the monsoon trough (line), locations of wave transition (light bar) and the subsurface ocean temperature anomaly ($^{\circ}\text{C}$) (dark bar) in the western Pacific for the period 1980-2001 July to October (Chen and Huang 2009).

2.9 *Origins of synoptic-scale waves*

While energy accumulation can explain the growth of synoptic-wave disturbances and energetics can be used to analyse the energy budget, it is also important to find out the origins of these waves. A number of observational studies using spectra along longitudes, Hovmöller diagrams, variance of low-level v-wind etc., indicate that the synoptic-scale waves in the western Pacific start to

become active around the dateline region (Nitta and Takayabu 1985; Liebmann Hendon 1990; Takayabu and Nitta 1993).

There have been discussions on the influence of the extratropical wave activities on tropical disturbances as well (Mak 1969; Nitta 1970; Magaña and Yanai 1995; Kiladis 1998; Tam and Li 2006; Zhou and Wang 2007). Mak (1969) found that forcing at lateral boundaries (30°N and 30°S) could initiate responses in the tropics with wavenumber and frequencies similar to MRG waves. Nitta (1970) found that for disturbances with periods longer than 6 days, the equatorward energy flux was strong in upper troposphere. It has also been mentioned in section 2.5 that the Mid-Pacific Trough could influence the low-level wave activities in the Tropics (Nitta and Takayabu 1985). In Tam and Li (2006), vertical cross-section associated with synoptic-scale disturbances showed that $v'T'$ was negative around 400-700hPa levels, meaning that the wave activity, or group velocity, was directed downward there. By using the regressed upper-level fields upon the leading PC of 850hPa vorticity, they suggested that synoptic eddies in the tropics could be originated from or triggered by eddies in upper-level extratropical regions. A case study on Typhoon Nanmadol (2004) found that the ancestor of the storm could be traced back to upper tropospheric MRG waves in the Eastern Pacific (Zhou and Wang 2007).

Another proposal for the wave origin is that MRG waves can be excited by energetic TD-type disturbances in the western Pacific (Dunkerton and Baldwin 1995). Chen and Tam (2012) found that energy dispersion from pre-existing off-equatorial disturbances could initiate MRG waves, based on idealized experiments in which a time-dependent heat source is located off an equatorial area in an anomaly model. The fact that TD-type waves can be transformed from MRG waves (see wave transition section) and MRG waves can be excited from TD-type waves showed that the synoptic-scale waves interact with each other and made the study more difficult. Nevertheless, further effort should be put into studying the origins of MRG waves as they are clearly related to convective and TC activities in summertime equatorial area.

2.10 Summary

The study of MRG waves in the atmosphere has been carried out for decades. Ever since the shallow water theory was proposed, the quest for understanding the science behind this type of equatorial waves has never stopped. With the help of the global gridded satellite data, their dispersive properties, relationship with convection, resemblance between the regressed dynamical field and theoretical wind structure, wave transition under energy accumulation, origins of

synoptic-scale waves were discussed in past studies. Most of these studies attempt to seek evidence for the existence of MRG waves in the atmosphere and compare them with the SWE solutions. Data from a certain period of time were gathered for analysis and usually one set of wave properties was used to describe all wave activities within that period of time. For instance, wavenumber, phase speed, group speed found with lag-correlation method are usually treated as the characteristics that are representative for all wave activities at one location. However, even for one particular location, properties of MRG waves might change during a period of time. The filtered variable at one base point (or PC of an EOF pattern) or the running variance of a filtered variable can show the wave activity variation over time. However, this kind of representation cannot resolve the change of wave properties at different locations. In other words, a new method is needed to describe the variation of MRG waves over both space and time simultaneously.

Another reason for developing a new method is that the wave dynamical structures were usually produced by regression with convection proxy data. The waves were first tracked within the convection data. Then the regression took place to produce a preferred wave structure. With this method, signals collected in dynamical variables must be describing the processes in which convection is

involved. As mentioned in WK99, the responses of dynamical variables and convection can be different. There is a possibility of missing out the uncoupled (or dry) stage of the MRG waves, if there is any. A new methodology was proposed by Yang et al. (2003) to track the equatorial waves. They projected the theoretical wave structure from SWE so that the instantaneous structures of different tropical wave modes were allowed. It was an innovative way of tracking these waves. However, the instantaneous wave properties were not extracted in their study. Their discussions on wave structures (Yang et al. 2007a) and the dispersion characteristics (Yang et al. 2007b) were based on the wave characteristics gathered from regressions or lag-correlations, not the instantaneous wave properties. In this study, their wave extracting method is modified so that the instantaneous wave properties can be studied.

Chapter 3

Data and Methodology

3.1 Data and filtering

In this study, the main dataset is the National Centers for Environmental Prediction (NCEP) Climate Forecast System Reanalysis (CFSR) data (Saha et al. 2010). Reanalysis data are a collective form of observations from various types of instruments. To construct the reanalysis, observations from sources such as satellite and ground weather stations were assimilated and then reprocessed in a numerical model to reduce the inconsistencies between different data sources. Hence reanalysis data are supposed to provide the best estimates of meteorological fields and the 6-hourly gridded CFSR dataset is used to study the observed MRG waves in this study. Here the global CFSR dataset, with resolution of 0.5° latitude $\times 0.5^\circ$ longitude, from 1980 to 2009 during the period of April to October were used. Upper-air variables considered include wind, vorticity, geopotential height, temperature and humidity. Outgoing longwave radiation (OLR) data from National Oceanic and Atmospheric Administration (NOAA) is also used in this study, which was spatially interpolated onto the same $0.5^\circ \times 0.5^\circ$ grid as CFSR and temporally interpolated as 6-hourly so that OLR can also be

included in the wave structure analysis.

Both CFSR and OLR data were filtered in the frequency and wavenumber domain, in order to obtain westward propagating MRG signals. Similar to previous studies, a 3-8day bandpass filter was applied to retain synoptic-scale wave signals (Nitta and Takayabu 1985; LL90; Takayabu and Nitta 1993; Roundy and Frank 2004). Only signals travelling westward were considered and signals with wavenumber larger than 20 were filtered out (corresponding to wavelength less than 2000km). For the v-wind, the symmetric component around equator is extracted because of the symmetry of MRG waves about the equator from the SWE solutions. Overall, the purpose of filtering is to extract MRG signals so that they can be projected clearly onto the theoretical equatorial wave structure, the procedure of which will be discussed below.

3.2 *Theoretical profile for MRG waves (mode n=0)*

According to Gill (1982) and Yang et al. (2003), the meridional structure $\hat{v}(y)$ in (3) can be written like this,

$$\hat{v}(\tilde{y}) = \sum_{n=0}^{\infty} v_n \cdot D_n(\tilde{y}) \quad (10)$$

where v_n is the coefficient for the n th mode and $D_n(y)$ is the parabolic cylinder function. This is the most general solution of SWE for the v-wind, which consists of the summation of all meridional modes. The term $D_n(y)$ here depends on latitude y (in degree) and y_0 (also in degree),

$$D_n\left(\frac{y}{y_0}\right) = 2^{-\frac{n}{2}} \cdot H_n\left(\frac{y}{y_0\sqrt{2}}\right) \cdot e^{-\left(\frac{y}{2y_0}\right)^2} \quad (11)$$

where H_n is the Hermite polynomials and $y_0 = \left[\frac{\sqrt{gh_e}}{2\beta}\right]^{1/2}$ is a parameter called trapping scale. It controls the meridional “stretching” of the theoretical equatorial wave because it is also related to the non-dimensional meridional coordinate $\tilde{y} = y \cdot (\beta/\sqrt{gh_e})^{1/2} = \frac{y}{\sqrt{2}y_0}$ mentioned in (4). As it is determined by the equivalent height h_e , the value also is related to the wave vertical structure as mentioned in the wave properties section. For MRG waves, $n = 0$ and $H_0 = 1$, $D_0\left(\frac{y}{y_0}\right) = e^{-\left(\frac{y}{2y_0}\right)^2}$, after adding zonally travelling component as in (1), the theoretical multiplying form of MRG waves can be written as

$$v' = v_0 \cdot e^{-\left(\frac{y}{2y_0}\right)^2} \cdot e^{i(kx - \omega t)} \quad (12)$$

where v_0 is the coefficient for mode $n = 0$.

3.3 Matching filtered data with theoretical profile

In Yang et al. (2003), y_0 was determined from the whole dataset by minimizing the difference between the sum of first ten modes and the reanalysis data. The value y_0 was found to be 6° . A similar approach was also adopted in this study. In particular, the meridional data was fitted to the gravest mode according to (12). Note that since the fitting was done for each snapshot of the v-wind, (12) becomes

$$v' = v_0 \cdot e^{-\left(\frac{y}{2y_0}\right)^2} \cdot \cos(kx + \theta) \quad (13)$$

Here the v-wind perturbation v' is equivalent to the filtered observational data which is considered as the perturbed activities around the mean basic state of the atmosphere. The filtered, symmetric component around the equator is used because the v-wind from the SWE solutions is supposed to have symmetric structure. In the following procedures, the symmetric component is shown in northern hemisphere.

Using the filtered, symmetric CFSR v-wind (v_{data}), values at equator (lower panel of Figure 28, line), local maxima and minima are found (crosses). At these locations, the magnitude of the term $\cos(kx + \theta)$ is assumed to be 1 and the coefficient v_0 is then determined by $v_{data}(x, y = 0^\circ, t)$ (see Figure 28, crosses).

Finally, the Gaussian profile in (13) is determined only at the longitudes that give the local maxima and minima of $\cos(kx + \theta)$. Hence, at these selected longitude positions, the projected v-wind v_{fitted} profile is,

$$v_{fitted}(x, y, t) = v_0(x, t) \cdot e^{-\left(\frac{y}{2y_0}\right)^2} \quad (14)$$

where $v_0(x, t) = v_0 \cos(kx + \theta)$ can be positive or negative.

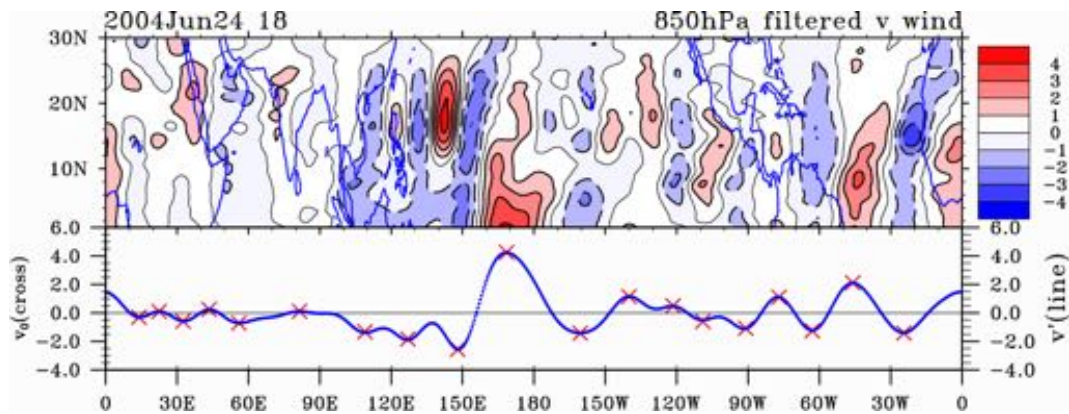


Figure 28 – A snapshot of filtered 850hPa v-wind v_{data} (upper panel), its value on equator (line, lower panel) and v_0 found at local maxima and minima (crosses, lower panel) on 2004 June 24th 18 UTC. Negative values are drawn with dashed lines. Unit: $m s^{-1}$.

The deviation $E(x, t)$ of this projected v wind calculated in (14) from the filtered data is then found with this,

$$E(x, t) = \sqrt{\frac{1}{n} \sum_{y=0^\circ}^{y=90^\circ} [(v_{data} - v_{fitted})^2 \times weight] / abs(v_0)} \quad (15)$$

where v_{data} is the filtered v wind and n is the number of grids in the positive y-direction. Note that this deviation is normalized by the magnitude of v_0 and weighted according to the latitudes so that values closer to equator contribute more than those from afar, with

$$weight(y) = \begin{cases} 1, & y = 0^\circ - 10^\circ \\ 0.2, & y = 10^\circ - 50^\circ \\ 0.1, & y > 50^\circ \end{cases}$$

Figure 29 demonstrates this process at the local maximum at 168.5°E on 2004 June 24th 18 UTC. Here it is seen that v_{data} (thick line) deviates from the Gaussian profile v_{fitted} (thin line) only for $y > 10^\circ\text{N}$, and the deviation E is found to be 0.062.

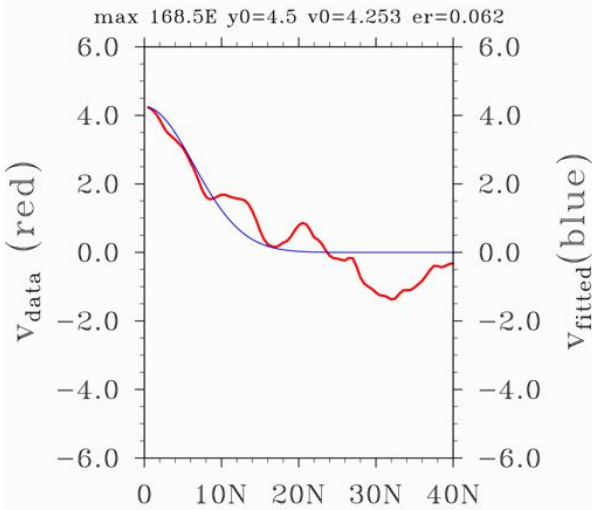


Figure 29 – The longitudinal distribution of v-wind at 168.5°E on 2004 June 24th 18UTC (see Figure 28). Thick line represents filtered data v_{data} and thin line is the projected values v_{fitted} (15).

Note that the value of v_0 is the value of filtered data v_{data} at equator. Unit: m s^{-1} .

3.4 Local wavenumber from wavelet analysis

Since the wavenumber k cannot be extracted from (12) because the phase θ is not determined at the selected local maxima and minima locations (hereafter “selected locations”), wavelet analysis (Torrence and Compo 1998; Gu and Zhang 2001) is performed in space in order to find the local spectral properties of these waves. Here wavelet analysis is performed using the Mexican hat function $\psi(x)$ (Torrence and Compo 1998), which is the second derivative of a Gaussian $e^{-x^2/2}$. For a series of V (filtered v-wind on equator at time t) with values $v(x, t)$ at longitudes x' , where each value is separated by δx , the wavelet transform $W(k, x)$ for wavenumber k at index x (longitudinal position) can then be written as the inner product of the complex conjugate of the wavelet function and series V ,

$$W(k, x) = \sum_{j'=0}^{N-1} v(x', t) \cdot \psi^* \left(\frac{x' - x}{a(k)} \right) \delta x' \quad (16)$$

where N is the number of values in series V and $a(k) = x = 360/k$. The spectral power equals to the sum of square of the real and imaginary parts of $W(k, x)$, as in Gu and Zhang (2001). The wavelet spectral power of the filtered, symmetric equatorial v-wind on 2004 June 24 UTC18 (Figure 30) shows that the

observed wavenumber (hence wavelength) of this variable varies greatly along the equator. The instantaneous local wavenumbers at different longitudes, $k(x, t)$, are then determined based on the location of the strongest signals of the wavelet transform in k space. For example, the wavenumber of the local maximum of v wind on equator at 170°E on 2004 June 24th was found to be around 6-7 (see Figure 30). Thus for each of the selected location, parameters $y_0(x, t)$, $k(x, t)$, $v_0(x, t)$ and deviation from Gaussian profile $E(x, t)$ can then be found.

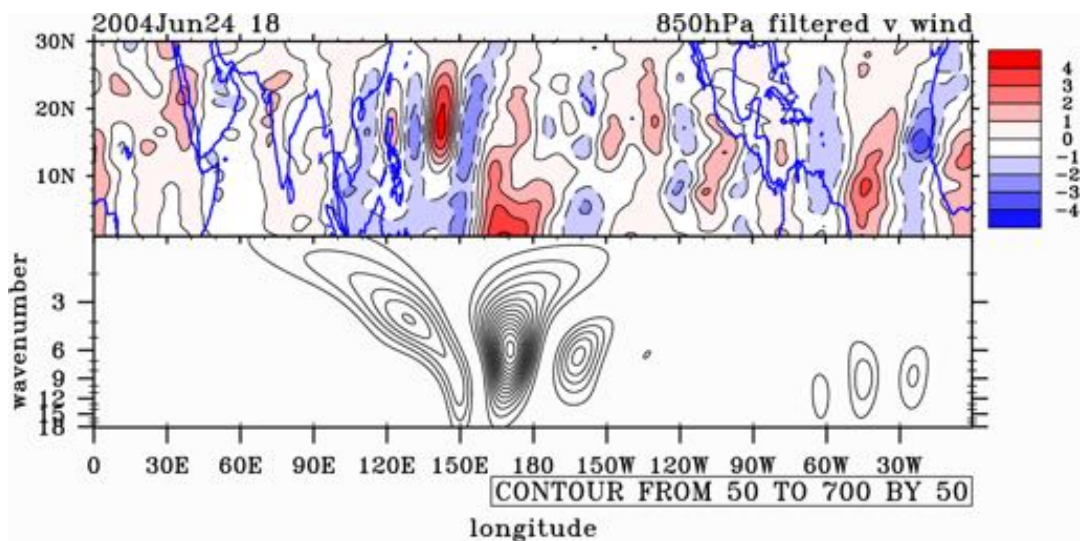


Figure 30 – Upper: same as Figure 28(upper panel). **Lower:** Spectral power found from wavelet power $W(k, x)$ (16) with k and x as indices of wavenumber and longitude.

3.5 Tracking MRG waves

Thus far, the selected locations, namely where MRG waves crests and troughs as identified by the Gaussian shape in the meridional structure, are only

found for each time step, they are not yet related in time dimension. To track wave propagation in time, an algorithm is developed to link the neighboring activity centers in the last time step (i.e. 6 hour earlier) with activity in the next time step. If no activity is identified in the previous time, the activity at the current time will be defined as a new start (Figure 31). Each of the series tracked MRG wave (black lines in Figure 31) is subject to a screening process: in at least one time step (black dots in Figure 31) $E(x, t)$ should be lower than a certain threshold (blue circles in Figure 31), meaning that the wave has a structure which matches the theoretical Gaussian shape. In other words, any wave signals with none of its $E(x, t)$ value lower than the threshold are discarded.

A range of thresholds for $E(x, t)$ was tested in this study, namely 0.04, 0.05, 0.06, 0.07 and 0.08. For $E(x, t) \leq 0.04$, there hardly any waves can be found; on the other hand, most of the shaded area in Figure 31 would be identified as MRG waves if the threshold of 0.08 is chosen. It was found that the results are not too sensitive to the choice of threshold because only dots corresponding to the blue circles in Figure 31 are used to form composites. All results presented in this study are based on the choice $E(x, t) \leq 0.06$.

Since the spatial interval between the linked data (CFSR resolution is 0.5° on latitude longitude grid) is known, the longitudinal travelling speeds, v_p , for the

linked activities can be calculated using a fourth order finite difference method,

and from which observed frequency can also be found using the relation

$\omega_{obs} = k\nu_p$. The intrinsic frequency ω_{int} is then given by,

$$\omega_{int} = k\nu_{int} = \omega_{obs} - k\bar{U} = k(\nu_p - \bar{U}) \quad (17)$$

where \bar{U} is the averaged unfiltered zonal speed (determined from average values

within area 5°S to 15°N and ±30° longitude of the zonal wind at 850hPa, and

within ±10days) around each selected location. The wave dispersion properties

can then be studied based on the wavenumber and frequency determined by the

method.

3.6 Other methods

To ensure that synoptic wave features found by this method are consistent

with those from past studies, conventional methods such as lag-correlation maps

(see Liebmann and Hendon 1990; Dunkerton and Baldwin 1995; Chen and Huang

2009) and kinetic energy balance (Lau and Lau 1992; Maloney and Hartmann

2001; Maloney and Dickinson 2003; Hsu et al. 2011; Ha et al. 2013) analysis

were also used. With these methods, wave features can be extracted and can be

compared with results found by wave tracking algorithm in this study.

3.7 Summary of the new algorithm

The new algorithm proposed in this study is similar to those used in tracking TCs. However, the MRG waves appear in form of wave trains and it requires more procedures before performing the actual tracking. All the procedures were mentioned in this chapter in details. The new algorithm can be summarized into the following order,

- 1) Take the symmetric component of CFSR 850hPa v-wind
- 2) Filter data to retain 3-8day fluctuation and $k = -20$ to 0 (westward propagating)
- 3) Identify local maximum/minimum value along equator
- 4) Match with the theoretical structure

$$v_{fitted}(x, y, t) = v_0(x, t) \cdot e^{-\left(\frac{y}{2y_0}\right)^2}$$

- 5) Compute error function

$$E(x, t) = \sqrt{\frac{1}{n} \sum_{y=0^\circ}^{y=90^\circ} [(v_{data} - v_{fitted})^2 \times weight] / abs(v_0)}$$

- 6) Track MRG if $E(x, t) \leq \text{threshold}$
- 7) Compute wavenumber k using wavelet analysis
- 8) Estimate phase speed v_p and average background \bar{U} ($5^\circ\text{S}-15^\circ\text{N}$, $\pm 30^\circ$ longitude, ± 10 days)
- 9) Compute intrinsic frequency

$$\omega_{int} = k v_{int} = \omega_{obs} - k \bar{U} = k(v_p - \bar{U})$$

All the functions above were already mentioned in this chapter before.

The differences between methods in Yang et al. (2003) and this study are summarized as follows:

	In this study	Yang et al. (2003)
	Events-based	Pattern-based
SWE Modes	Only n=0	n=0,1,2,...10
Info obtained	Locations/times of each MRG wave event	Instantaneous projected patterns
Usage of info obtained	Wave properties of each MRG wave	Regression / lag-correlation
Trapping scale y_0	found for each MRG instantaneously	$y_0=6^\circ$
Wave properties	found for each MRG instantaneously, including wavenumber, frequencies, magnitudes	one set of wave properties are found for each wave mode by regression / lag-correlation

Although both methods involve projection of theoretical wave solutions, method proposed in Yang et al. (2003) aims at obtaining projected patterns for later regression and lag-correlation. Instantaneous wave properties are not examined. This study focused on individual wave events. After applying the new dynamical method, each MRG wave event can have the following properties computed,

- \mathbf{k} : Wavenumber from wavelet
- v_p : Phase Speed
- \bar{U} : Background zonal wind average ($5^\circ\text{S}-15^\circ\text{N}$, $\pm 30^\circ$ longitude, ± 10 days)
- ω_{int} : Intrinsic frequency, $\omega_{int} = k(v_p - \bar{U})$
- y_0 : meridional shape
- v_0 : magnitude, filtered v-wind v' at each MRG wave location
- E : deviation from theoretical Gaussian shape

Analysis thus can be performed with these wave properties.

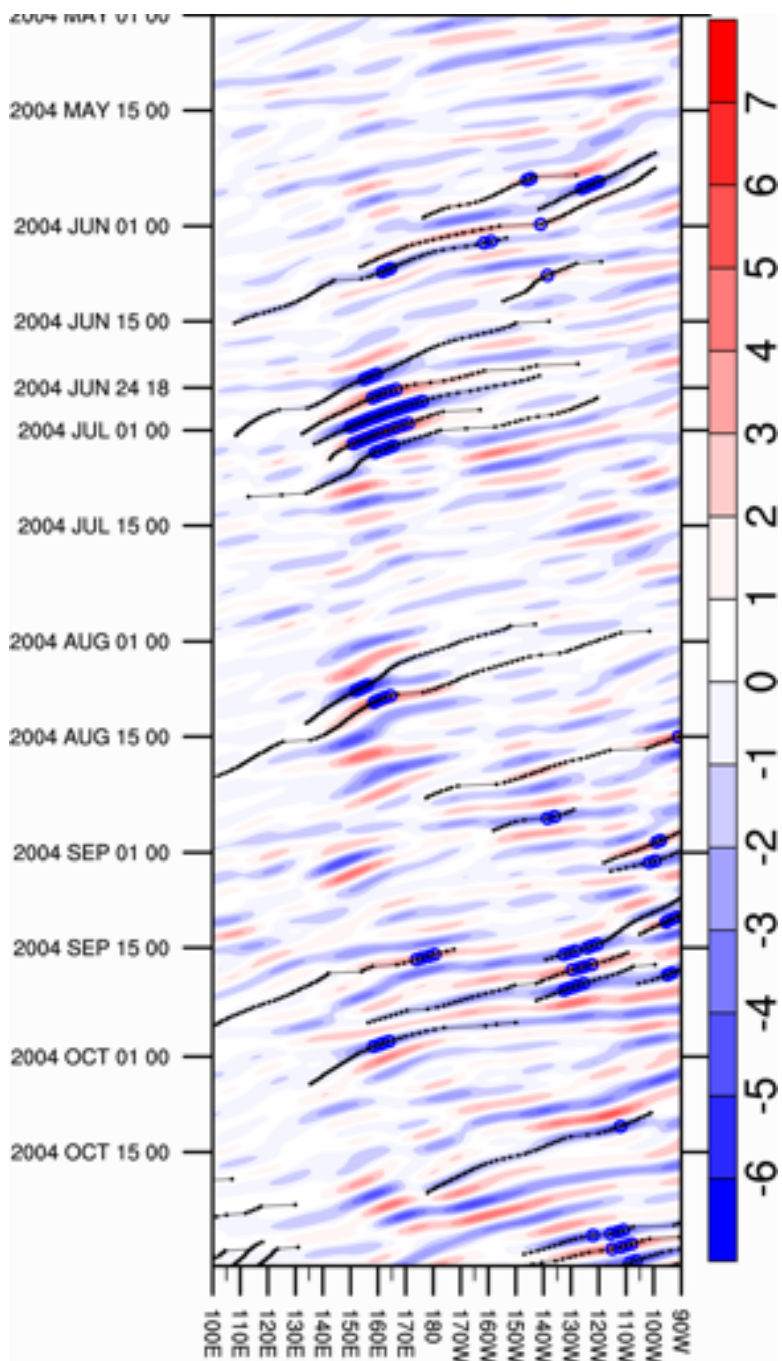


Figure 31 – Selected locations (black dots), tracked wave activities (black lines) and filtered v-wind v in shading.

Threshold used for tracking here is $E(x, t) < 0.06$ (Blue circles).

Unit of shading: ms^{-1} .

Chapter 4

Wave features in CFSR dataset as inferred from spectral and regression-based methods

In order to study the spectral characteristics of the low-level v-wind, spectral analysis was first performed based on the global CFSR data. A suitable frequency band for temporal filtering domain was determined. Then lag correlation based on the filtered v-wind was done to examine the wave properties of the synoptic-scale MRG waves in the CFSR data. In this chapter, MRG wave properties will be found using these techniques and results will be compared with those from past studies.

4.1 Spectral analysis

Before using the reanalysis data to track the structure of MRG waves, spectral analysis of the v-wind was performed to find out which types of oscillations are active, their active area and time in the western Pacific. V-wind is used because synoptic-scale signals (Liebmann and Hendon 1990) are found to be more obvious in the v-wind. Thus the low-level v-wind is used in tracking the waves in this study. In this section, frequency spectra at different locations and

wavenumber-frequency spectra will be presented.

Spectra of 850hPa v-wind for different locations in the western equatorial Pacific were computed based on the tapered 6-hourly CFSR data during the 1980-2009 period for the April-to-October season (Figure 32). In these figures products of frequency ν and spectral power $P(\nu)$ were plotted instead of just $P(\nu)$ to avoid the red noise nature of the data (increasing power with decreasing frequency; see LL90). Strong variance with a typical period of 3 to 8 days can be clearly seen in this region, with the activity being more pronounced in the northern hemisphere than that in the southern hemisphere. The 3-8day spectral peak within this band becomes stronger as one moves from the central pacific (170°E, 0°) to farther north-western locations at about (130-150°E, 10°N). This suggests that signals within 3-8day period bands should be retained (with other signals filtered out) so that they are ready for the following wave-tracking process.

Variation of the 3-8day period activities within the boreal summer season was also examined by computing the 850hPa v-wind spectrum at various locations along the equator, for different months in summer from 1980 to 2009 (Figure 33). The figure is the same as Figure 32 except that the spectra were found for different months, and for both zonally travelling components (eastward

and westward). From the central to the western Pacific, the 3-8day oscillations begin to be active in June and became stronger in late summer. Similar spectral speaks around dateline using twice-daily reanalysis data for the September-December 1980-1987 seasons can be found in Liebmann and Hendon (1990, their Figure 2). Their averaged power for September-December does not show the intraseasonal variation of the climatological wave activities. Indeed the synoptic-scale waves show a great amount of intraseasonal variation such that some features are not present in the averaged plot (see Figure 33). At first the westward 3-8day activities seem to be originating at 150°E in June. They become stronger and stronger from June to October and at the same time has an eastward extension to the central Pacific. Similarly, at 10°N , synoptic-scale waves become active in June at 135°E and extend eastward, but the highest power remains east of 150°E and the extension is less pronounced (Figure 34). The most active area on the equator is between $150^{\circ}\text{E}-180$ (see Figure 33), while at 10°N it is $130^{\circ}-150^{\circ}$ (see Figure 34). This is consistent with the interpretation that the most active westward travelling synoptic-scale waves move away from equator as the season progresses. This will be further discussed in next section.

The intraseasonal variation of synoptic-scale tropical waves was also captured by Takayabu (1994a, her Figure 7a), who found increasing magnitudes

starting from May-June for the 5°N-10°N averaged blackbody temperature (proxy for convective activities) variances. These increasing magnitudes found within 5°N-10°N are comparable to the peaks found in this study (see Figure 33). It was not shown in her plot that the seasonal variations were location dependent and the synoptic-scale activity variations at equator can be attributed mainly to the area around central to western Pacific.

The influence of the eastward components should not go unnoticed here. As mentioned in Chapter 2, the eastward moving planetary-scale intraseasonal variability is closely related to synoptic-scale oscillations embedded in it. At 10°N, eastward signals with period longer than 10 days are quite strong west of 150°E (Figure 34), which are at the same locations where there are prominent westward moving 3-8 day oscillations. However, the westward propagating 3-8 day oscillations signals extend beyond 150°E starting from August, without the presence of any low frequency waves. Thus the wave properties of westward moving 3-8 day band maybe different for area east and west of 150°E. The major difference would be both faster and slow waves exist west of 150°E but only faster waves remain east of 150°E. It is out of the scope of this study to discuss the relationship between the planetary-scale intraseasonal oscillation and synoptic-scale waves. However, the issue is stated here as a reminder that in

reality other types of oscillations exist and should not be overlooked.

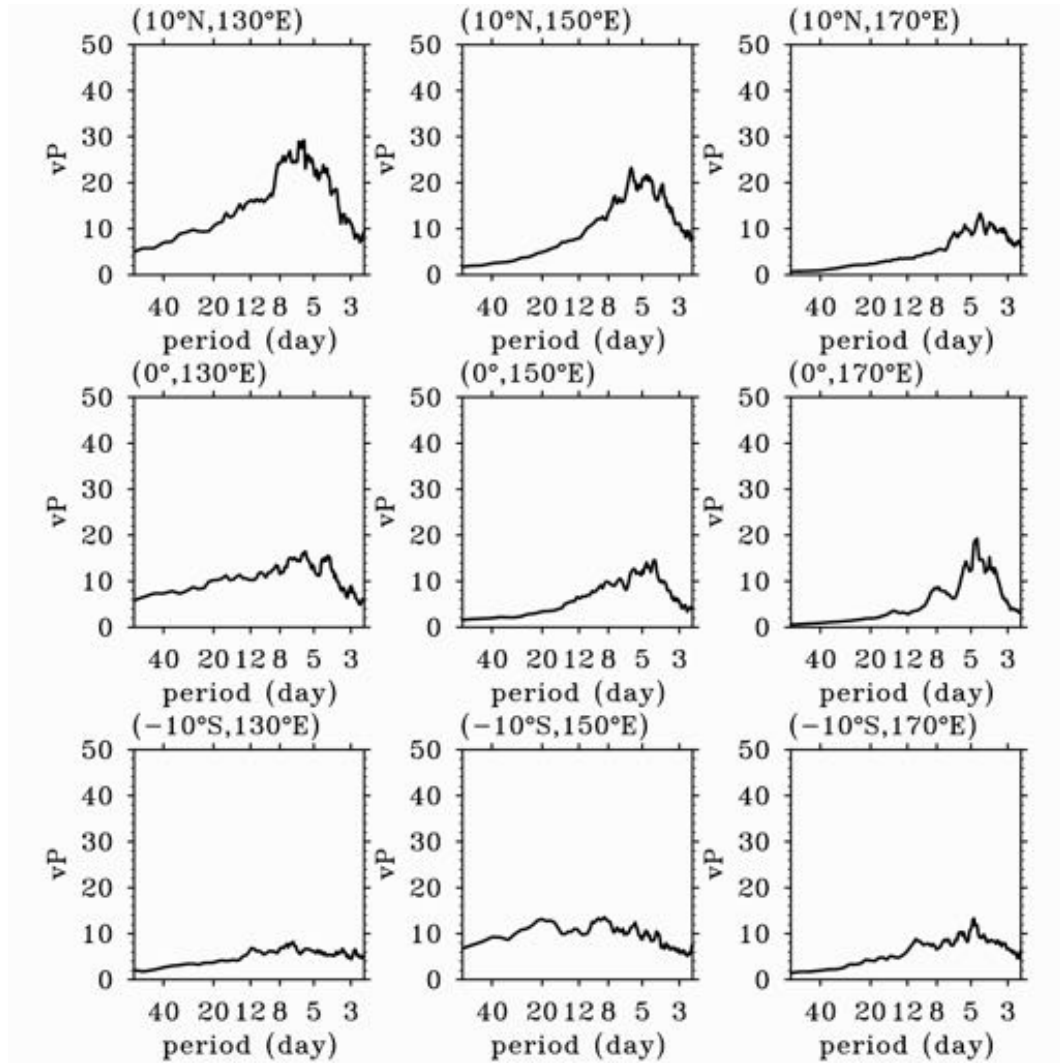
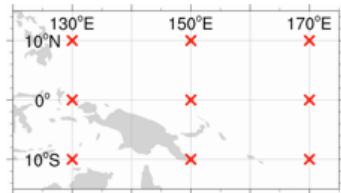


Figure 32 – Spectrum of 850hPa unfiltered v-wind
from 1980-2009 April to October over 12 locations in
the western North Pacific. The locations are shown in
the map. Graphs are plotted with $vP(v)$ (unit: $\text{m}^2 \text{s}^{-2}$)
against $\ln(v)$ (unit: day) where v = frequency, P =
power.



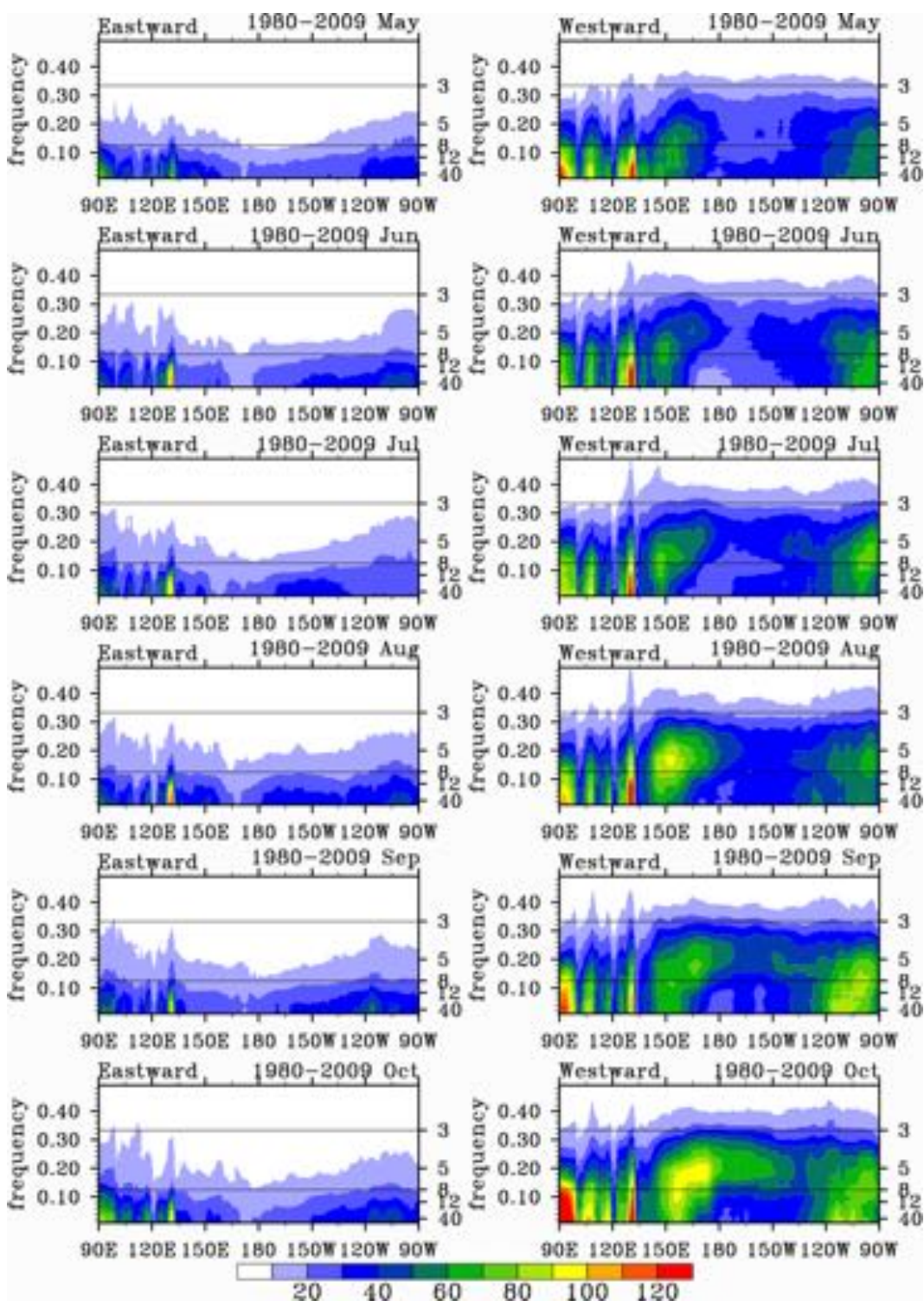


Figure 33 – Spectrum power $P(v)$ of unfiltered 850hPa v-wind (1980-2009) for the equator against longitudes for months from May to October. The eastward (westward) traveling powers are on left (right) panel. Left y-axis refers to frequency (cycle per day). Right y-axis refers to period in days. The thin lines indicate where period=3day and 8day. (shading unit: $m^2 s^{-1}$)

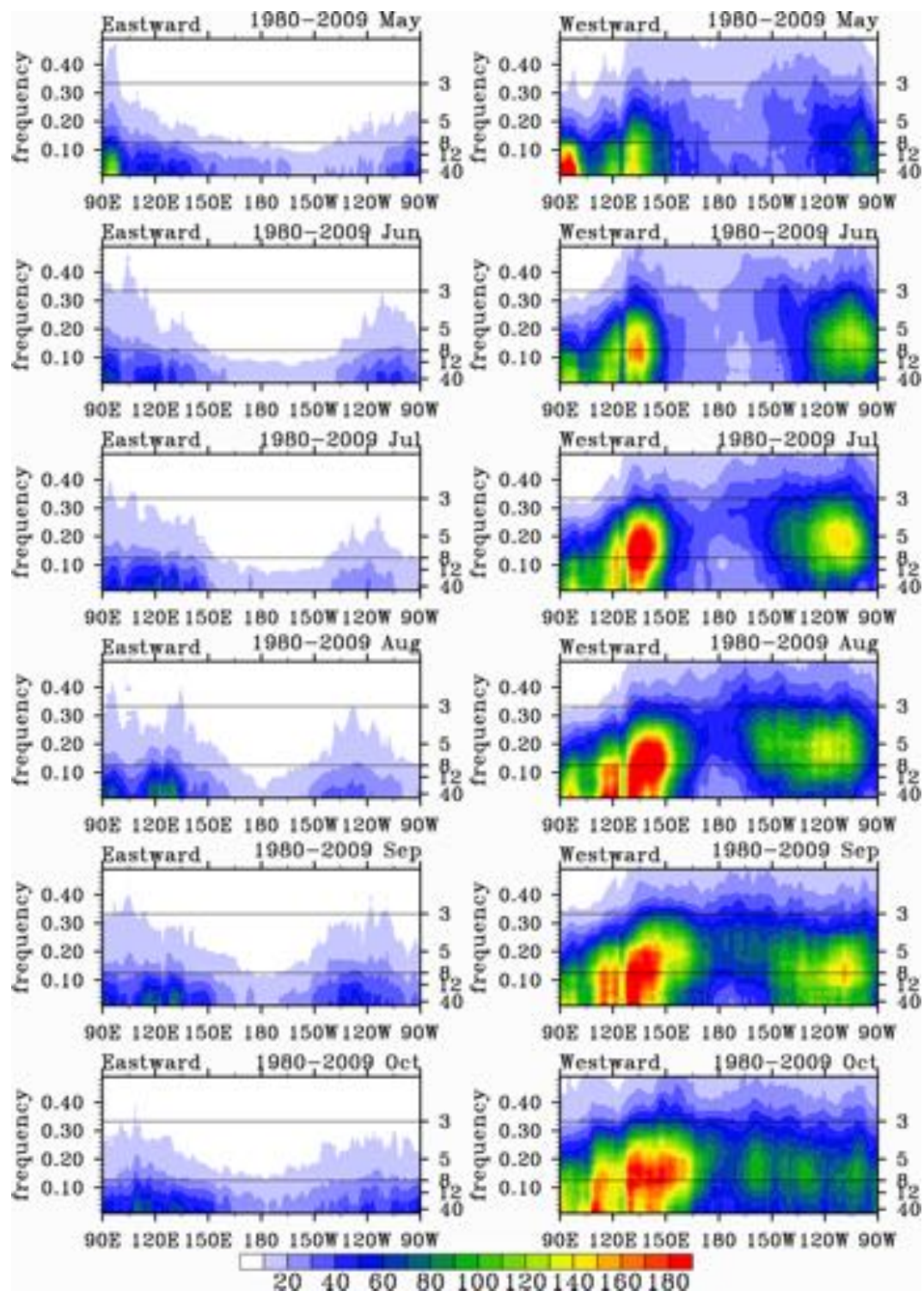


Figure 34 – Same as Figure 33 except for latitude 10°N

From the 850hPa v-wind frequency power spectra, it was found that the synoptic-scale oscillations are dominant in the central to western Pacific. However, tropical waves do not just vary in terms of their oscillation frequencies; they also vary in their spatial scales (see Figure 11). Therefore, a wavenumber-frequency spectral analysis is carried out to examine their dispersion characteristics. WK99 mentioned that the spectral response of the dynamics (in their case, the temperature fields) was quite different from those of the convection signals. This implied that OLR might just cover a portion of the tropical wave signals and one might expect different spectral features if another variable, say a dynamical variable, is investigated. Following WK99, the wavenumber-frequency spectrum of the 850hPa v-wind was computed, in order to extract zonally propagating wave signals in the equatorial area (Figure 35). The spectrum covered the April-October seasons over 1980-2009 and data from each season was tapered. Since the solutions of SWE are either symmetric or asymmetric about the equator, the gridded v-wind data can be decomposed into its symmetric and asymmetric components. Given that $V(\phi)$ is the latitude ϕ depending v-wind, the symmetric component $V_{sym}(\phi) = \frac{V(\phi)+V(-\phi)}{2}$ and the asymmetric component $V_{asym}(\phi) = \frac{V(\phi)-V(-\phi)}{2}$ are then used to produce the symmetric and asymmetric spectra (Figure 36).

In Figure 35 and Figure 36, the signals of the 850hPa v-wind spectrum are stronger with lower frequency/wavenumber. To separate spectral signals from the background, which is assumed to be the random activity without wave-like behavior, a background spectrum is first constructed. The background spectrum here (Figure 37) is produced by averaging the power of the symmetric and asymmetric components (see Figure 36), and smoothed many times with 1-2-1 filter in frequency and wavenumber. Number of passes of the 1-2-1 smoothing filter on power with frequencies less than 0.1 cycle per day (cpd), 0.1-0.2cpd, 0.2-0.3cpd and greater than 0.3cpd are 5, 10, 20 and 40. Although WK99 has pointed out that some of the periodic signals might still be retained in the background, major characteristic power signals seen in Figure 36 are removed. WK99 suggested that by dividing the symmetric (or anti-symmetric) power of a variable by the background power, the spectral properties stand out. Since the v-wind structure around the equator is symmetric for MRG waves (see Figure 6), the MRG signals are expected to appear in the symmetric spectrum (Figure 36). The symmetric spectrum is then divided by background (Figure 38). The power peaks suggest that filtering the CFSR data in frequency domain (3-8days) and wavenumber domain ($k=-20$ to 0, hence westward component) is appropriate as these areas over which the strongest activities are found in the spectrum.

On the dispersion curves on the divided spectrum, the inferred equivalent depths from SWE solutions for MRG waves are also shown. It can be interpreted as the parameter linking horizontal wave structures with vertical structures, and was found to be 12-50m in WK99 for convectively coupled waves. Our results indicate significant amount of power in the symmetric 850hPa v-wind with frequency of 0.2-0.3cpd and h_e between 12-50m. This part of the v-wind oscillations agrees with WK99 and is probably involved in the convectively coupled tropical MRG waves. Signals beyond the linear wave solution (indicated by domain beyond $h_e=\infty$) can also be found in the power spectrum indicating of active TD-type disturbances. Other than those spectral signals already discussed in WK99, very strong spectral peaks overlap with equivalent depth $h_e=\infty$. These peaks can also be found in Gehne and Kleeman (2012) with v-wind. The peaks seem to be localized because wavenumbers and frequencies are available at discrete level for the spectra. The peaks with westward wavenumber 2-3 are referred to as the 2-day planetary-scale wave (Salby 1981). These planetary-scale waves may have little connection with the MRG wave signals (as suggested by WK99, signals between $h_e=12\text{-}50\text{m}$) and the TD-type waves (signals beyond $h_e=\infty$) as they appear separated in the wavenumber-frequency domain. Therefore, their effect will not be discussed in this study. The fact that spectral properties of

850hPa v-wind are consistent with WK99's OLR spectrum indicates that both parameters could be involved in the synoptic-scale waves. Again, this indicates that it is also suitable to use v-wind to track MRG waves.

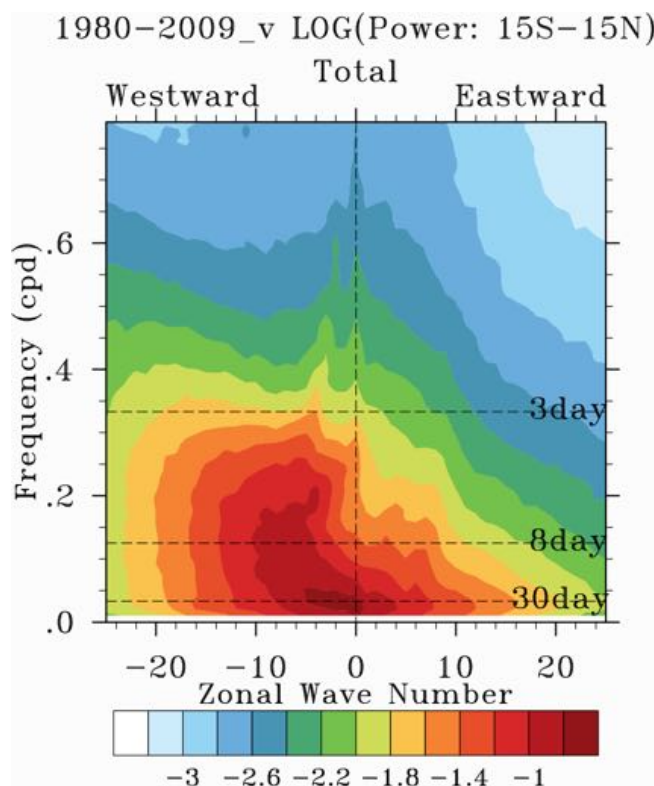


Figure 35 – The zonal wavenumber-frequency power spectrum of v-wind power (as in Wheeler and Kiladis 1999) calculated for the period 1980-2009 April-October.

Power values are the sums between 15°S to 15°N and base-10 logarithm is used.

Left y-axis refers to frequency (unit: cycle per day).

The oscillation periods (in days) are shown with horizontal dashed lines.

Contour interval is 0.2 arbitrary units.

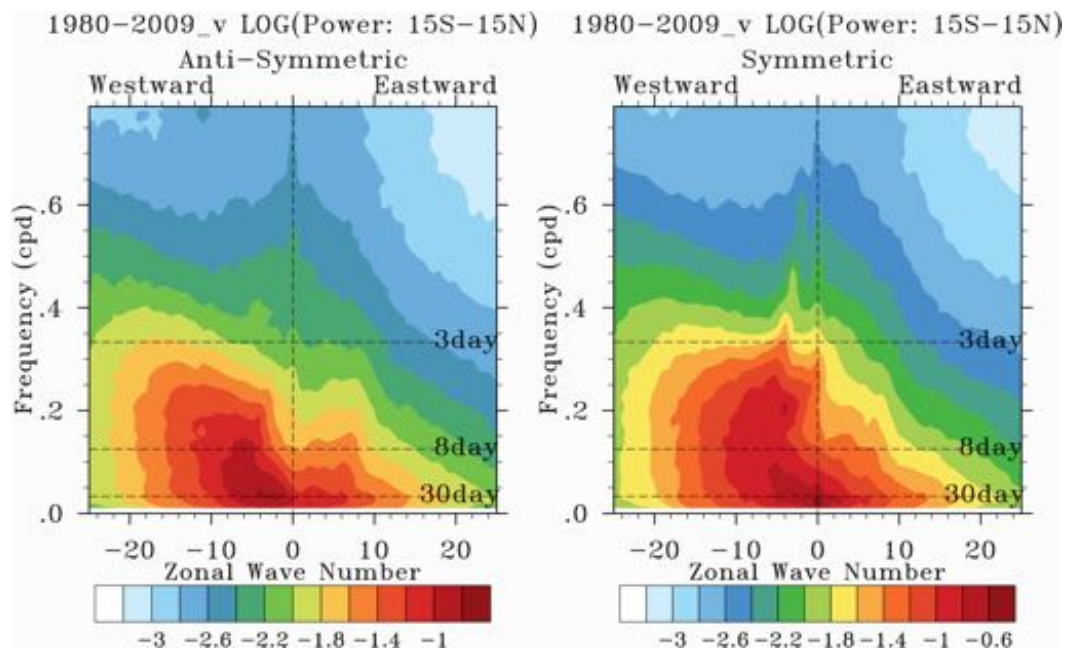


Figure 36 – Same as Figure 35 except the anti-symmetric and symmetric components about the equator are extracted.

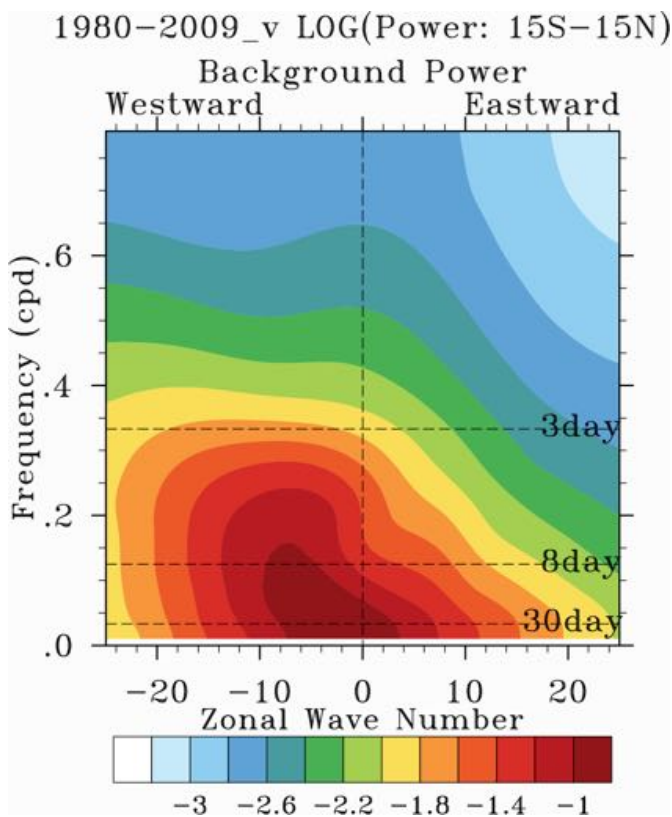


Figure 37 – Background spectrum produced from adding spectra in Figure 36 together and smoothing with 1-2-1 filter many times (details referred to text).

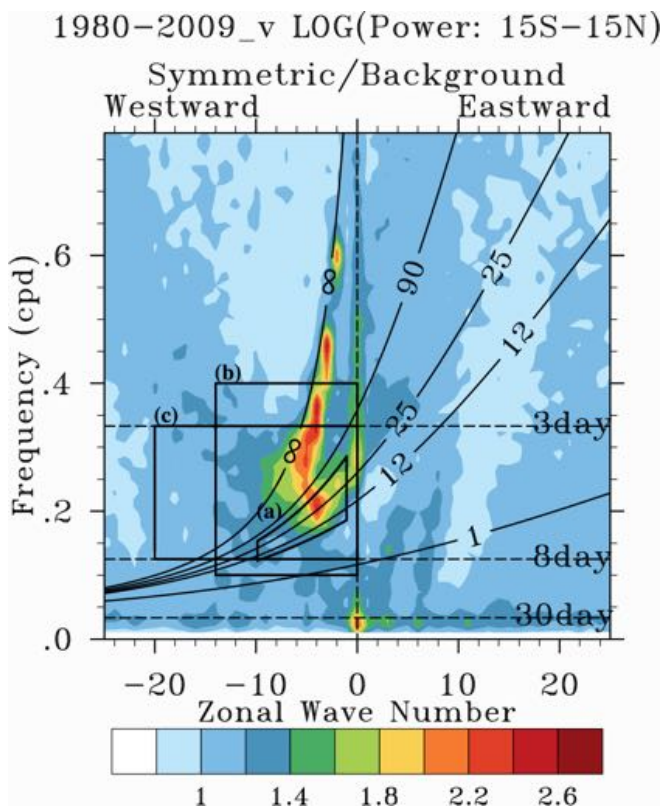


Figure 38 – The symmetric v-wind power divided by background power.

The curves are the dispersion profiles for MRG waves ($n = 0$) predicted by shallow water theory. The values of equivalent height $h_e = 1\text{m}$, 12m , 25m , 50m and ∞ are marked on the curves.

Enclosed areas indicate regions of MRG wave domain defined in (a) WK99, (b) Ching et al. 2010 and (c) this study

4.2 Variance of filtered meridional wind

In the last section, spectral properties of the low-level v-wind suggests that 3-8day period oscillations are prominent, and synoptic-scale waves can be extracted effectively based on such signals in the data. After performing time filtering, the variance of the filtered v-wind (Figure 39) is examined before performing the wave-tracking algorithm. The spectral properties of Figure 33 and Figure 34 only show the level of activity at 0° and 10°N , and the filtered variance here can further indicate areas in which westward synoptic-scale waves are most active. Based on v-wind data with period of 3-8day and wavenumber of -20 to 0,

low-level transient activities are found to be most active in the western Pacific, eastern Pacific and Atlantic basins (see Figure 39). The Indian Ocean basin is not discussed due to its weaker activities and the activities are in the winter hemisphere. Similar to what was found in the spectral analysis (see Figure 34 and Figure 35), synoptic-scale activities are most active between $150^{\circ}\text{E}-180^{\circ}(120^{\circ}-150^{\circ})$ near the equator (10°N). These westward propagating transient activities shift away from the equator near 150°E , and the variance attains its maximum east of the Philippines. The strong amplitude implies some energy generation mechanisms occurring in the area. This will be discussed in the part on wave energy energetics. Other transient-active areas include the eastern Pacific and the eastern Atlantic.

As mentioned in the literature review, the background flow, or the large-scale circulation, where the transient activities are embedded, can affect the wave structures, transport and generation of wave energy. Therefore, it is also important to examine the background zonal flow \bar{U} where the transient activities are most active. As mentioned above, in the western North Pacific, the strongest filtered variance appears to be located at the low-level convergence zone (Figure 40a). There is a change in the direction of low-level average zonal wind near $\sim 130^{\circ}\text{E}$ at the equator. It can greatly affect the MRG waves, which are characterized by the

low-level wind field. This can be demonstrated clearly if the vertical zonal wind distribution is examined. In fact, the westerly vertical shear becomes easterly shear in the western Pacific at 10°N (Figure 41), which means a change of the three-dimensional environment. The change of vertical shear can give rise to different vertical tilting structures of the MRG waves, which will be discussed in the section on composite structure of these waves. The zonal wind remains easterly in the central Pacific from 10°S-10°N (Figure 40a,b). Therefore in the next section, the calculated values of intrinsic frequencies of MRG waves are not sensitive to the choice of domain for \bar{U} around the equatorial area.

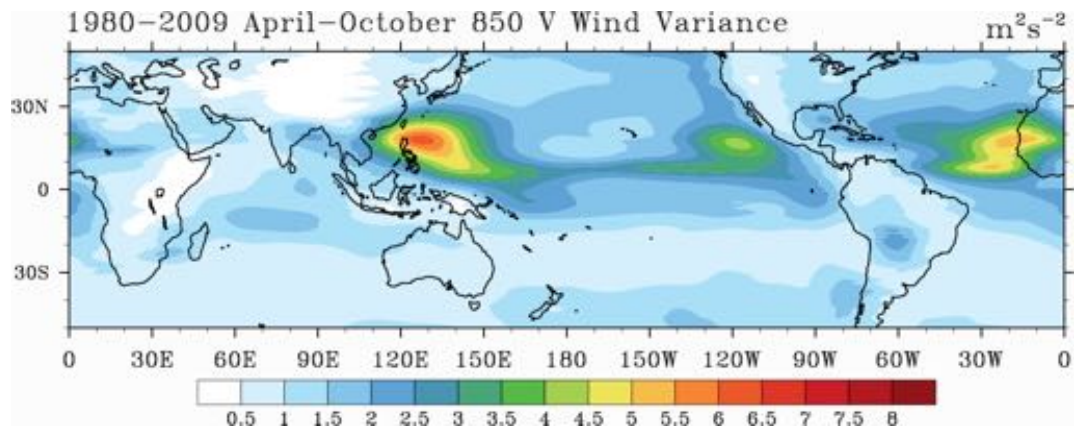


Figure 39 – 850hPa meridional bandpass-filtered wind variance in 1980-2009 April to October.

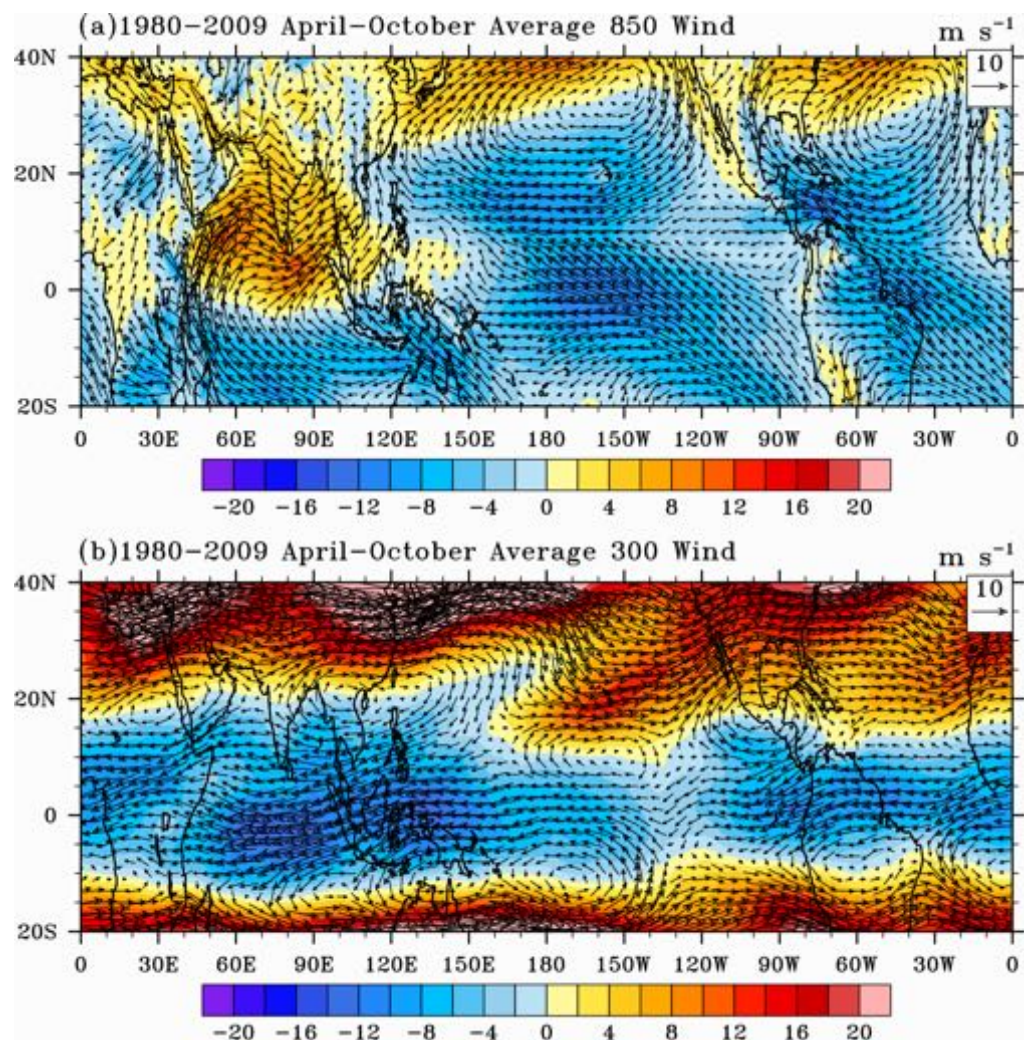


Figure 40 – Mean Wind in 1980-2009 April to October at pressure level (a) 850hPa and (b) 300hPa. Mean zonal wind (m s^{-1}) is shown in shading.

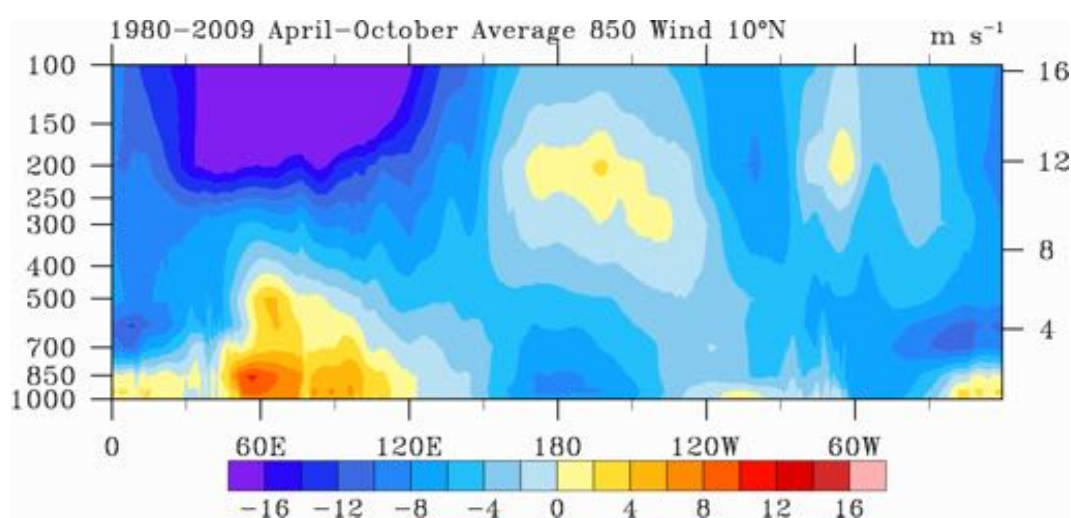


Figure 41 – The vertical distribution of mean zonal wind (m s^{-1}) at 10°N .

4.3 Lag-correlation analysis

Before applying the new tracking method using the CFSR dataset, lag-correlation analysis was done to assure that wave signals could be found in this dataset. Lag-correlation diagrams can show the MRG wave oscillating properties by values of correlation between the base grid point and locations around this base point, and also between times before and after the MRG events. The correlation values between -1.0 and 1.0 are shown with contours on time-longitude graphs.

As in Liebmann and Hendon (1990) (see their Figure 5), lag correlation maps of the filtered v-wind were calculated from CFSR data (Figure 42). Since the waves are presented in a time-longitude plane, the phase speed (v_p) and group speed (v_g) can be found from the slopes as demonstrated in the left top panel. The wavelength (λ , units=degree longitude) equals to two times of the length of the horizontal black line. The corresponding wavenumber (k) can be found by $k = 360/\lambda$. The unfiltered average zonal wind \bar{U} are the average values within area 5°S to 15°N and $\pm 30^\circ$ longitude around each stated location. The mean zonal wind was found so that it can be subtracted from the phase speed to obtain the intrinsic speed and frequency. The intrinsic phase speed (v_{int}) can be found by $v_{int} = v_p - \bar{U}$ and the intrinsic frequency is then just $\omega_{int} = kv_{int}$. The

equivalent depth h_e can be deduced from $c = \frac{\omega_{int}^2}{k\omega_{int} + \beta}$, and using $h_e = \frac{c^2}{g}$. The parameter $\beta = 2\Omega \cos \phi / a$ here equals $2.3 \times 10^{-11} \text{ s}^{-1} \text{ m}^{-1}$ at the equator, where $\Omega = 7.292 \times 10^{-5} \text{ rad s}^{-1}$ is the earth's angular speed of rotation, $\phi = 0^\circ$ is the latitude and $a = 6.37 \times 10^6 \text{ m}$ is the mean radius of earth. The wave properties at different locations are presented in Table 2.

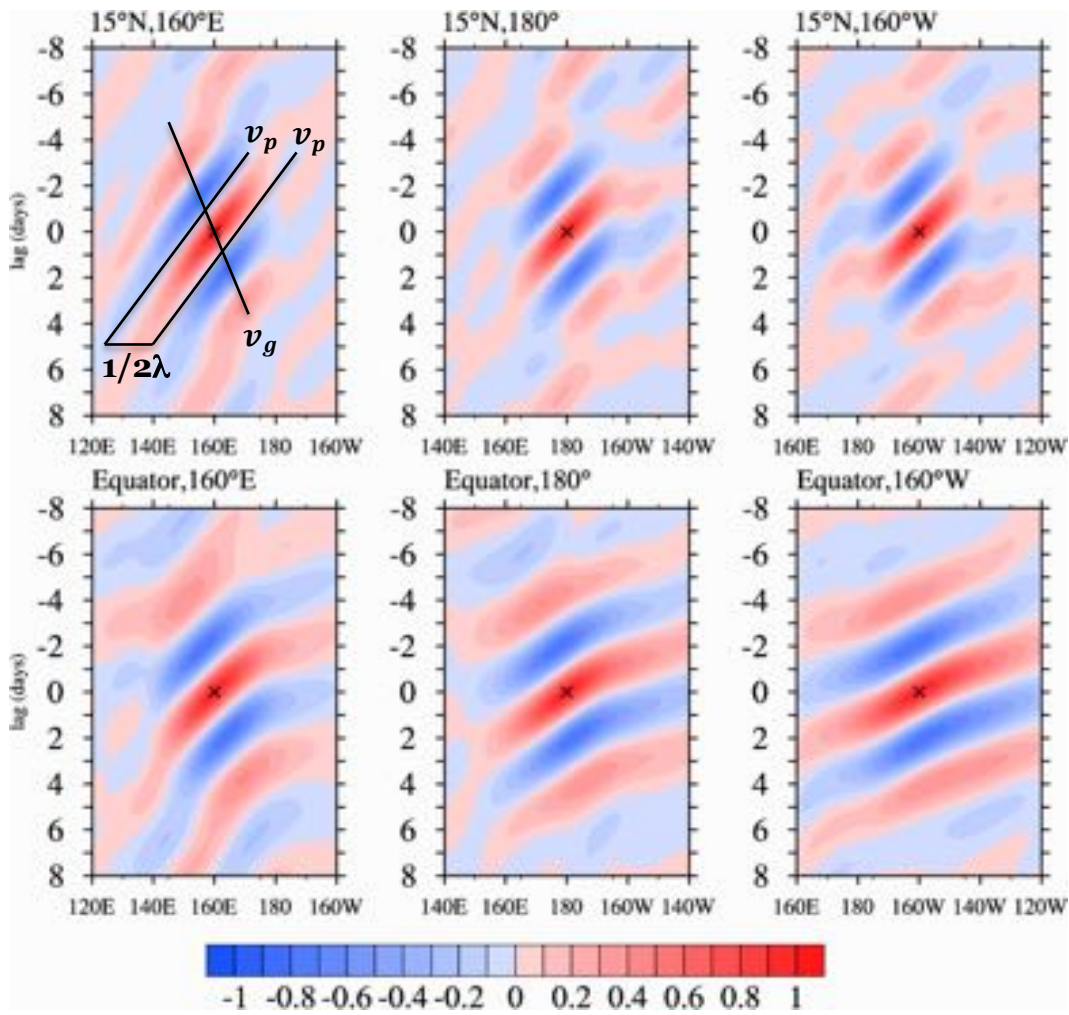


Figure 42 – Longitude-lag correlation between bandpass 850hPa v-wind at different locations – (15°N, 160°E), (15°N, 180°), (15°N, 160°W), (0°, 160°E), (0°, 180°) and (0°, 160°W) – and filtered 850 v-wind. The slopes of black lines shown in 15°N, 160°E graph indicate the values of phase speed (v_p) and group speed (v_g). The length of the horizontal black line indicates value of $1/2 \lambda$.

Wavelength at the equator is shorter and westward travelling phase speed is smaller in the western Pacific ($\sim 4700\text{km}$, -11.2m s^{-1}) comparing to the eastern Pacific (~ 6700 , -25.7m s^{-1}). This difference is similar to results found in composite maps by Liebmann and Hendon (1990), Dunkerton and Baldwin (1995) (their Figure 12) and Chen and Huang (2009) (Table 1). The easterly wind zonal wind has smaller magnitude in western Pacific (-5.17m s^{-1}) comparing to eastern Pacific (-7.53m s^{-1}), as consistent with mean wind in Figure 40. The intrinsic frequencies found are $\sim 0.1\text{-}0.2$ cycle per day (cpd), which is consistent with those in Liebmann and Hendon (1990) and Takayabu and Nitta (1993). Unlike the equivalent depths h_e of about 12-50m as found by WK99, the equivalent depths are much smaller. This could be due to the fact that v-wind, as the most prominent dynamical variable and as the signature of MRG waves, might give different wavenumber-frequency characteristics from those convectively coupled waves (WK99). The small values of h_e will also be discussed with the dispersion diagrams produced by wave tracking method in the next chapter. The group speed is larger in western Pacific than that in the eastern Pacific. This is consistent with Liebmann and Hendon (1990) and it means the eastward energy transport is anticipated to be stronger in the western Pacific. Similar calculations are done to

obtain the 2d lag-correlation maps (Figure 43). The off-equatorial movement of the synoptic-scale waves indicates the possibility of observing MRG-TD-type wave transformation in the filtered v-wind data. In summary, the wave properties found by lag-correlation analysis in filtered CFSR data suggest that the dataset is suitable for synoptic-scale wave tracking.

Locations		λ (km)	k	v_p (ms ⁻¹)	\bar{U} (ms ⁻¹)	v_{int} (ms ⁻¹)	ω_{int} (cpd)	h_e (m)	v_g (ms ⁻¹)
Equator	160°E	~ 4700	8.6	-11.2	-5.17	-6.03	0.11	0.39	2.27
	180°	~ 6400	6.2	-17.7	-7.15	-10.55	0.14	0.93	2.5
	160°W	~ 6700	6	-25.7	-7.53	-18.17	0.22	4.75	1.9
15°N	160°E	~ 3200	12.4	-7.3	-3.82	-3.48	/	/	3.9
	180°	~ 3600	11.2	-8.1	-5.2	-2.9	/	/	3.3
	160°W	~ 3800	10.6	-9.6	-5.38	-4.22	/	/	3.0

Table 2 – Wave properties found from lag correlation graphs (see Figure 42) at different locations. They are wavelength (λ), wavenumber (k), phase speed (v_p), group speed (v_g), intrinsic speed (v_{int}), intrinsic frequency (ω_{int}), equivalent depth (h_e) and average zonal wind (\bar{U}).

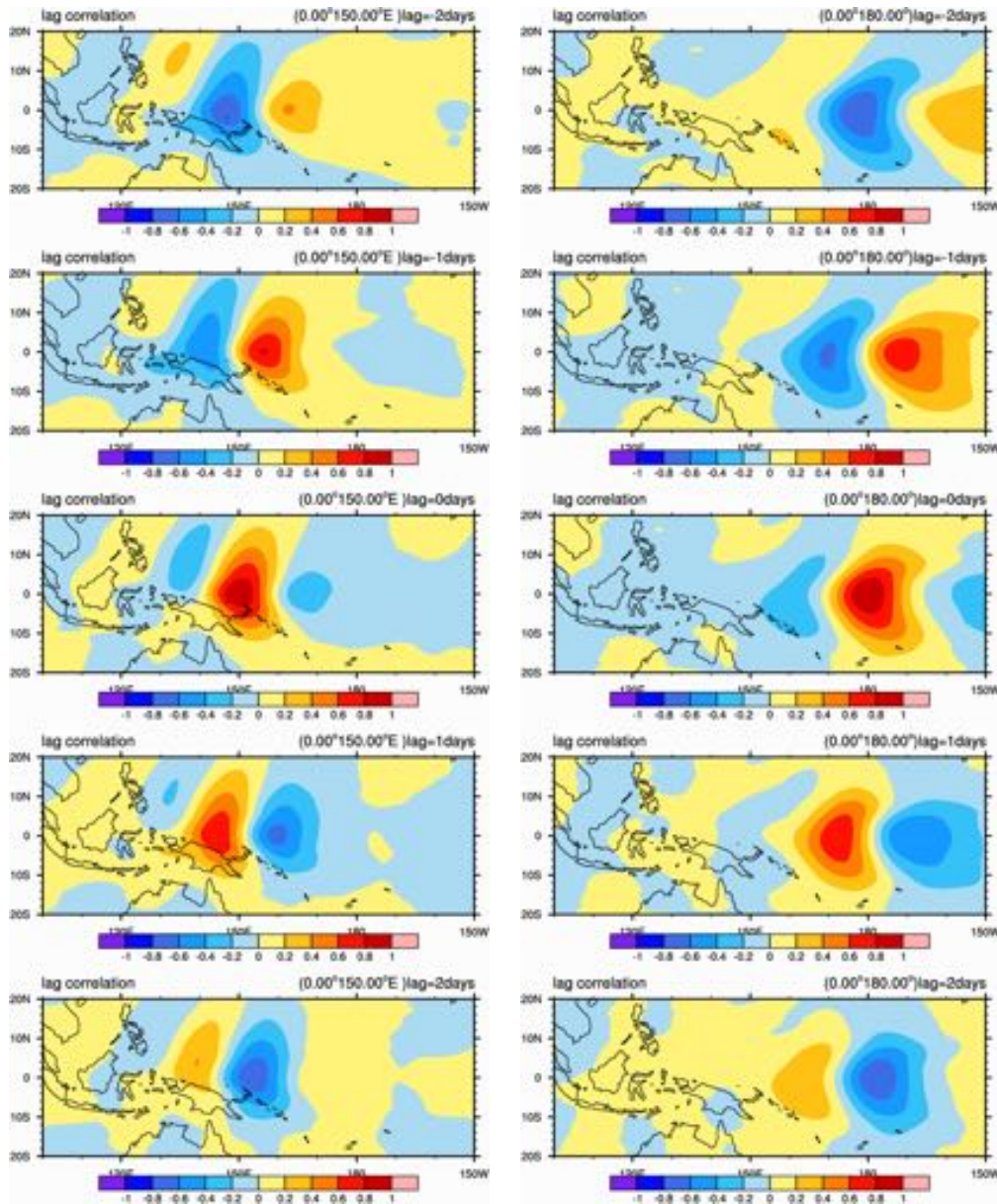


Figure 43 – Correlation of filtered 850hPa v-wind at two locations at equator, 150°E (left panel) and dateline (right panel).

4.4 Summary

Information as inferred from lag-correlation maps, or spectral analysis, can only represent the averaged wave properties for a certain time period. In other

words, the wave properties found here, such as phase speed and wavelength, depend on longitudes and latitudes only, and are not able to represent any variations in time. If one seeks to examine the wave property change (such as wave amplitudes) over a short period of time, say within a typical period of 5 days, a time dependent method is needed to track these MRG waves. A running-averaged variance of MRG was provided in Wheeler et al. (2000) (Figure 15). Their method provides a systemic method to evaluate the strength of different modes of tropical waves. However, the running-averaged variance of each mode only represented the change of variance in the location wherever the variance is the largest. That means their method can track the waves depending on time, but not space. Also, all the filtered data, within a certain wavenumber-frequency domain, was assumed to be MRG waves. They did not consider the possibility that there are time periods where MRG waves cannot be found in filtered data. This provides the motivation to this study, which seeks to track the MRG waves in both space and time.

Chapter 5

Wave features tracked by dynamical method

A novel technique was proposed for MRG wave-tracking; based on such a wave-tracking program, local wavelength and frequency of waves at different geographical locations can be determined. From the tracked wave activities, their corresponding wave properties can be used to compose dispersion diagrams and graphs showing their occurrences according to regions. The dispersion characteristics were then compared with dispersion curves from theory. Composite maps of different dynamical variables were also computed in order to show how these waves evolve over time. Then the tracked variables were used to examine terms in kinetic energy balance equation, in order to gain more insights on the physical processes involved with the MRG waves.

5.1 Dispersion diagrams

For each of the located wave activity on the equator, the intrinsic frequency and wavenumber were recorded with procedures stated in sections 3.4 and 3.5 respectively. Because the waves were tracked using 6-hourly filtered CFSR data, here “one tracked MRG wave” means an MRG-like v-wind structure is found at

one particular instance from the 6-hourly data. Since only westward travelling signals are considered, the minus sign of the wavenumber k will be omitted in the following discussions. The wavenumbers and intrinsic frequencies are sorted into different bins: $k=0$ to 20 ($\Delta k = 1$) and $\omega_{int}=0$ to 0.4 ($\Delta\omega_{int}=0.04$). Their occurrences are counted for each bin. The seasonal average occurrences are shown with shadings on a wavenumber-frequency plane and the graph is also known as dispersion diagram (Figure 44). Past studies utilized spectral analysis to obtain the dispersion properties of a variable and data in all longitudes are needed. In this study, the wavenumber-frequency properties can be categorized into different basins because this algorithm tracks each wave activity in time and space. The choice of longitudes for each basin is based on locations where the filtered variance (see Figure 39) is the strongest: 110°E-180° for western Pacific, 180°-75°W for eastern Pacific and 75°W-0° Atlantic. Indian Ocean is not considered here because the transient activities are not significant and the wave activities lie in the winter hemisphere. Results are found to be not sensitive to different choices of averaging domains for computing the background wind \bar{U} (refer to section 4.2) and different values of the threshold E . Similar results are obtained under other steering levels such as 300hPa and 700hPa (not shown).

To examine the overall MRG wave activities of the northern hemisphere in

summertime, there is also a graph gathering the occurrences of all three concerned basins. Two peaks obtained show that there are two major groups of transient activities (Figure 44a). One group appears with lower wavenumber ($k \sim 6$, $\lambda \sim 6700\text{km}$) and has the highest occurrences. The other group has higher wavenumber ($k \sim 11$, $\lambda \sim 3600\text{km}$). It might not be suitable to discuss the overall situation because the wave occurrences are highly dependent on their locations. Since two groups of waves are mainly from western and eastern Pacific, the following discussions will be mainly about the comparison of the wave properties found in these two basins.

The occurrence in eastern Pacific is the highest (Figure 44c). The major group $k \sim 6$ in eastern Pacific agrees with the results found by lag-correlation in this study (section 4.3) and in Liebmann and Hendon (1990). Both wavenumber groups ($k \sim 6$ and $k \sim 11$) appear in both eastern and western Pacific (Figure 44b,c). The fact that waves with different length scales appearing in the same basin agrees with the past discussions on the co-existence of both MRG waves and TD-type waves and possible existence of wave type transformation in the basin (see wave transition section). It should also be noted that the wave features found are different for the two basins. Most of the events appear with $k \sim 6$ are in eastern Pacific and events with $k \sim 11$ are in western Pacific. The longitudinal spatial

scale difference between eastern and western Pacific found agrees with past studies (Liebmann and Hendon 1990; Takayabu and Nitta 1993). The total average numbers per season are ~ 32 , ~ 31 and ~ 11 for western Pacific, eastern Pacific and Atlantic respectively. The numbers of MRG events in western and eastern Pacific are very close, but the dispersive properties have larger variation in western Pacific (spread out more) than those in the eastern Pacific (more events with $k \sim 6$).

At least one event happened each season with the equivalent heights range from 0.1m to 400m. A part of the wave signals extracted from dynamical features in this study corresponds to the $h_e = 12\text{-}50\text{m}$ suggested by WK99. While it is reasonable to expect wave signals found in WK99 are convection-related, it was not discussed whether waves with the smaller equivalent depth found in the temperature spectra (their Figure 4a) exist in the atmosphere. The other part where the waves are not corresponding to the convectively coupled MRG waves can also be seen in Gehne and Kleeman (2012) using dynamical method (in their Fig 10f). The fact that low-level v-wind dispersion diagram covers both the convectively-coupled signals and other signals suggests that it is possible to study both coupled and non-coupled stages with the variable.

The wavenumber-frequency relationship found here suggests that even

though the proposed new algorithm tracks the MRG waves case by case, it is pursuing the same wave type as mentioned in past studies. Since the wavelengths are found to be dependent on the locations, the geographical distribution of wave occurrences will be examined in the next section.

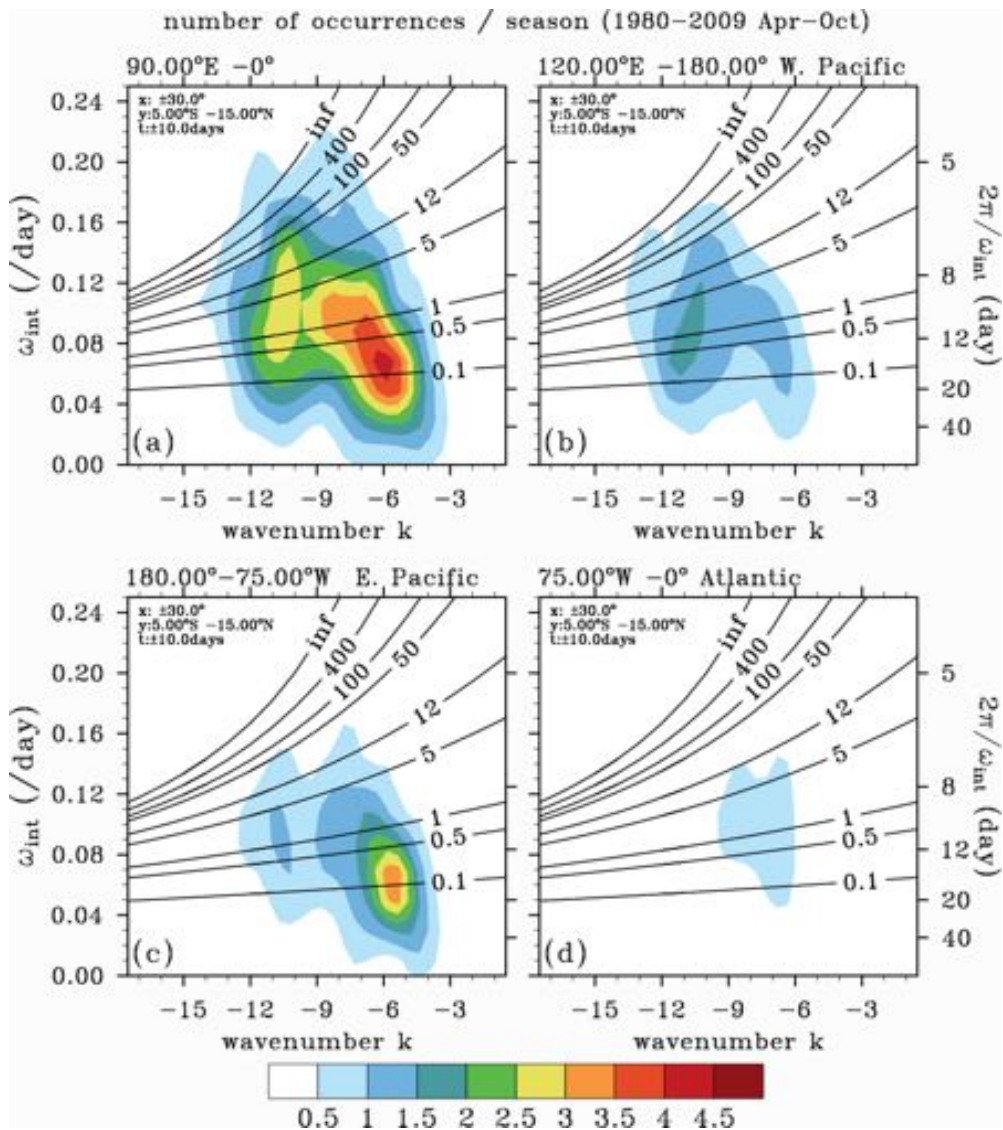


Figure 44 – Number of occurrences according to intrinsic frequency and wavenumber per summer during 1980-2009 in (a) all three basins, (b) western Pacific, (c) eastern Pacific and (d) Atlantic. Black lines are the dispersion relation of MRG waves and the values are the equivalent height (h_e) in meter.

5.2 Occurrences of MRG waves

Since the new algorithm can track each of the MRG wave in space and time, it is possible to examine the geographical distributions of wave occurrences and strength. The tracked waves are sorted according to their longitudes ϕ with bin size of $\Delta\phi=5^\circ$. The seasonal average of their occurrences and the corresponding $v_0^2/2$ is shown for each bin (Figure 45, bar color and bar height respectively). Here square of v-wind at a certain location can be considered as the wave strength. It is divided by 2 so that it is comparable to kinetic energy. Averages of $v'^2/2$ from filtered v-wind at all longitudes at the equator are also calculated (Figure 45, black line) so that comparison can be made between the synoptic-scale filtered data and MRG waves collected by the algorithm. Similar to the last section, this section will focus on the transient wave activities in eastern Pacific, western Pacific and Atlantic Ocean (Figure 45a). The longitudinal variations of the peaks of both $v'^2/2$ (line) and $v_0^2/2$ (bar height) are quite similar in the three basins, with $v_0^2/2$ being about 10 times larger than $v'^2/2$. The occurrence numbers (bar color) indicate that the chance of having MRG waves in some area is quite small, even though the average $v_0^2/2$ is not small (white bars). Attention should be paid to the longitudes where it is more likely to observe MRG waves (bar colors).

MRG waves in western Pacific have larger variation in dispersive properties (see last section) but most events happen are between 150°W-180. In other words, most of the MRG waves keep appearing in same area with diverse (or changing) properties. As for the events in eastern Pacific, they appear almost all over the region, but with rather uniform dispersive properties (see last section). The MRG waves in the two basins behave quite differently. Discussions on wave property change, environment they are embedded in and the wave triggering mechanisms have been discussed in the past (see Chapter 2). In this study, composites of the wave events are made to extend our understanding of MRG waves (next section). In Atlantic Ocean, the values of average wave strength $v_0^2/2$ are larger than 10 times of $v'^2/2$ although the occurrences found there are not particularly high.

Since the wave activities were found to belong to two groups in the frequency and wavenumber domain (see Figure 44), the geographical distribution in Figure 45a can be plotted again for the $k>9$ group (Figure 45b) and the $k<9$ group (Figure 45c). They are supposed to represent the two groups of MRG waves with $k\sim 11$ and $k\sim 6$ respectively. The activities with larger wavenumber (hence tighter structure) mainly appear west of dateline and fewer of them are seen in the eastern Pacific and rarely appear in the Atlantic, indicating that there might be a unique atmospheric condition in the western Pacific. The drastic contrast between the

east and west of dateline for waves with higher wavenumber implies that it is possible that there are some processes in that area are responsible for the wave initiation or generation. The activities with lower wavenumber ($k \sim 6$) appear with similar occurrences in all three basins (Figure 45c) and with similar peaks with wave strength. In the area west of dateline, there is also a significant amount of activities with lower wavenumber, also indicating co-existence of both types there. The geographical distribution of $v_0^2/2$ and $v'^2/2$ on latitude-longitude map are quite similar (Figure 46) between 150°E and 180°. Here total tracked wave activity is shown instead of averaged because there are locations where the wave occurrence is quite small (white bars in Figure 45a).

The special behavior of the transient wave activities in the western Pacific prompts the search for the mechanisms behind the MRG wave initiation and maintenance processes. The composites to be shown in the next sections are meant to shed light on this issue.

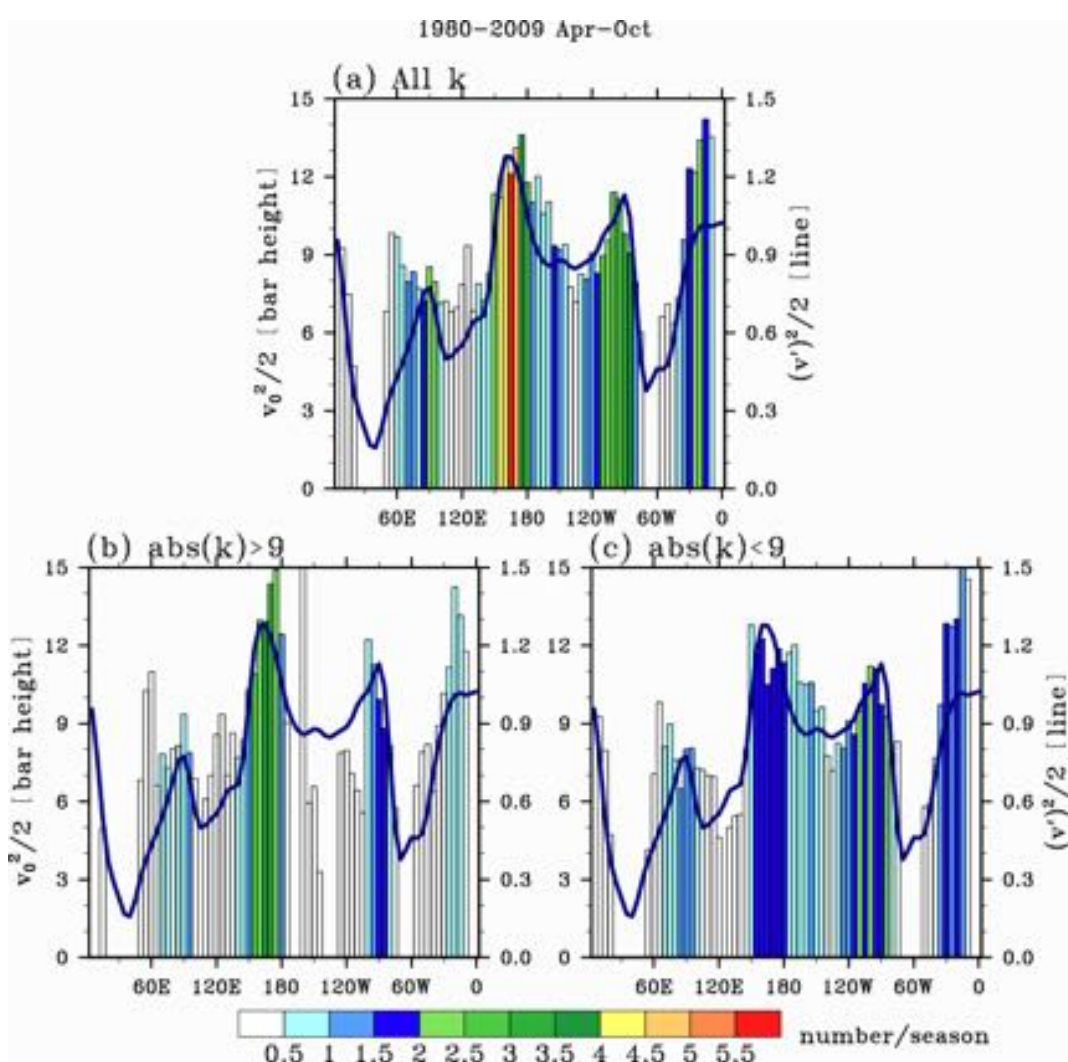


Figure 45 – Average $v_0^2/2$ of tracked wave activity (bar height) and average $v'^2/2$ from filtered wind field (black lines). Color indicates the number of occurrences per season for each bin. Bottom two plots are for the wave activity with absolute wavenumber smaller than 9 and larger than 9. Black lines in all three graphs are identical. Units bar height and line: m^2s^{-2}

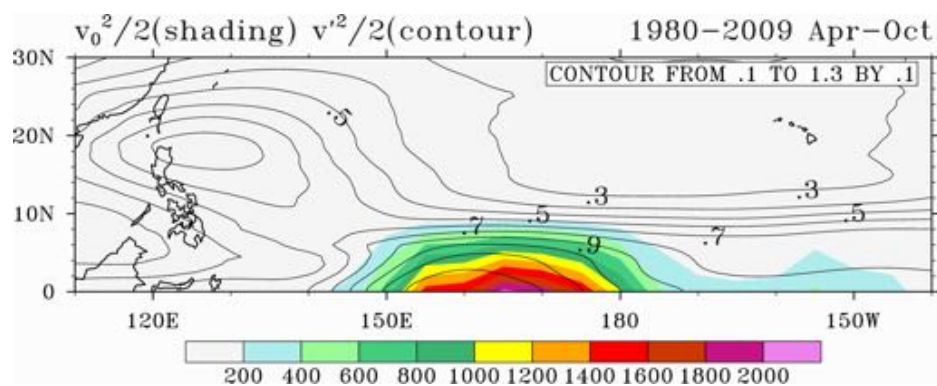


Figure 46 – Total $\left[v_0(x)e^{-(|y|/y_0)^2}\right]^2/2$ of tracked wave activity (shading) and seasonal average $[v'(x,y)]^2/2$ from filtered wind field (contour). Units: m^2s^{-2}

5.3 Composites of three-dimensional circulation and convection

It has been a common practice to examine typical tropical wave structures (different atmospheric fields) by using composites (Nitta and Takayabu 1985, LL90, Lau and Lau 1992, Takayabu and Nitta 1993, Ching et al 2010, Chen 2014). Composites are averages of atmospheric fields at selected locations and time frames. They tend to retain features common to all selected fields and to eliminate those that vary in time and space among the fields (Done et al. 2011). Some of the composite studies were briefly mentioned in section 2.5. They will be further discussed here.

There are currently a number of ways to track MRG waves in space and time. One is to use a longitude-time plot (Hovmöller diagram) of a filtered variable and composites (Figure 18) are made at reference longitudes (Takayabu and Nitta 1993). There is no objective criterion other than finding strongest local maxima (or minima) in the data and all synoptic-scale activities will be included. This might not be suitable because not all filtered data should be included if the study is about MRG waves. This could be shown by Figure 45, where the variable $v'^2/2$ from filtered v-wind is not as strong as the wave strength $v_0^2/2$. The second method is to perform EOF analysis and obtain a typical wave pattern on a map and the oscillation of the pattern (determined by a time series of coefficients)

can then be used to track the waves in time (LL90, their Figure 13). Wave patterns determined from the EOF analysis limit the concerned “waves” to a certain waveform in space and the EOF patterns are sensitive to the domain chosen. This is again not suitable because the wave dispersive characteristics vary in space and time (Figure 44). In this study, we try to track MRG waves in space and time with the help of the theoretical dynamical structures; in a way that the waves are allowed not only to have varying properties over time, but also varying waveform, or length scale at the same time.

By the new wave tracking method (Chapter 3), the MRG waves are found (blue circles in Figure 31) at selected times and locations. The fields of the waves are aligned to the middle longitude for each of the basin (basin regions are determined in section 5.1) and averaging the aligned fields at all vertical levels can then yield the composites in the western Pacific (Figure 47). Filtered variables including v-wind, temperature, geopotential height, horizontal and vertical wind and OLR are used to form composites of different cross-sections:

- i) horizontal cross-section at pressure level 200hPa,
- ii) horizontal cross-section at pressure level 850hPa,
- iii) vertical cross-section at 15°N, and
- iv) vertical cross-section at middle longitude of the defined domain (the fields

are aligned at this longitude, for example it is 145°E for western Pacific).

Here the longitude 145°E should not be confused with the true 145°E because it is the position where the MRG waves are aligned in the western Pacific domain. It should rather be considered as the locations where MRG waves are found. The above four cross-sections of v-wind (contour) and temperature (shading) are shown in Figure 47a-d and the cross-sections of geopotential height (contour) and OLR (shading) are shown in Figure 47e-h. OLR values in each vertical level in Figure 47g,h are duplicates of those values shown on Figure 47e,f (both Figure 47e,f are showing same values of OLR). Vectors on Figure 47e,f and those on Figure 47g,h are the horizontal wind and vertical pressure velocity respectively and the vectors are all above 99.9% significance level. The details of statistical significance test will be discussed later. Domain ±40° longitude and ±30° latitude around each MRG wave would be used, including all vertical levels. All fields found in western Pacific are aligned at 145°E (from 105°E to 175°W) and size of the composites is 80° in longitude and 60° in latitude. Results from horizontal and vertical planes will be presented in the following paragraphs and will focus on western Pacific composites (Figure 47). Composites for the eastern Pacific are in Figure 48. Figure 49 and Figure 50 are the composites of the unfiltered average zonal wind. The wind shear condition for the tracked MRG waves is similar to the

seasonal average zonal wind in Figure 40.

5.3.1 Composites at $t=0$ day

The alternating signals of 850hPa v-wind collected at $\sim 145^\circ\text{E}$ and $\sim 162^\circ\text{E}$ in Figure 47a (contour) and the corresponding cyclonic flow and anti-cyclonic flows in Figure 47e (vector) agree with theoretical structure in Figure 6c. For each found MRG wave, values of v-wind at one single longitude is used in the tracking process (see section 3.2). However, the composite wave structures here at regions around the tracked locations still resemble the MRG pattern found by the EOF pattern (Kiladis et al. 2009, their Figure 12). The northwestward movement of the alternating synoptic-wave train (Nitta and Takayabu 1985, Liebmann and Hendon 1990, LL90, Takayabu and Nitta 1993) is also captured here. Comparing to western Pacific, the lower-level circulations in the eastern Pacific are more trapped in the equatorial region (Figure 47a,e and Figure 48a,e). And there is obvious zonal contraction (past studies refer to section 2.7) comparing wave structure at 145°E and the off-equatorial structures near Philippine in Figure 47a. All the features found in the composites here support the idea that findings from the new algorithm are consistent with past studies and it is possible to find the theoretical MRG structures in instantaneous filtered data objectively.

In Figure 47e (blue shading), the active convection indicated by negative OLR around 140°E appears around the convergence of v-wind. As implied in the linear theory, the anti-symmetric structure of the divergent field calculated from filtered data is expected to be strongly correlated to convection (Pires et al. 1997, their Figure 17). The southwest-northeast tilt of the regressed OLR pattern mentioned in Wheeler et al. (2000) (their Figure 13) can also be found here. Furthermore, the convection is more tightly connected to the low-level circulation in western Pacific than that in the eastern Pacific (Figure 47e and Figure 48e, similar results found in Dunkerton and Baldwin 1995, their Figure 9). In this study, the captured OLR features at t=0day of MRG waves are consistent with linear theory and also past studies.

The southwest-northeast tilting wave train structures similar to that on 850hPa are also present at the level of 200hPa (Figure 47a,b). The 200hPa activities appear east and north of those on 850hPa level. This gives rise to the speculation that those activities are related. To find out their relationship, the vertical cross-sections at one latitude (15°N) and one longitude (145°E, middle of the domain) are presented (Figure 47c,d,g,h). Those are at locations in between the upper- and lower-level wave activities and are supposed to reveal connection between them, if there is any.

Vertical structures started to become obvious at the middle longitude of the composites (Figure 47c,g contour). The 850hPa wave train appears to be triggered around the middle of the domain (locations where MRG v-wind signature were identified), but actually there is a similar wave train appearing in higher latitudes and originating from further east on 200hPa level. The cross-section at 145°E (Figure 47d contour) shows that the 200hPa v-wind local maximum (Figure 47b contour) is connected to the 850hPa v-wind local maximum at equator. The connection will become more obvious in the series of composites before and after t=0day, and will be further discussed in next section. Other major features concerning the vertical structures are also found in Figure 47c,g (similar results in past studies are also listed here):

- i) warm/cold cores at ~300hPa level (similar to Wallace 1971 his Figure 18, Chang et al. 1970 their Figure 6, LL90 their Figure 16),
- ii) westward tilting of v-wind (Nitta and Takayabu 1985 their Figure 13, Dickinson and Molinari 2002 their Figure 3, Yang et al. 2007a their Figure 7) due to low-level convergence from background low-level zonal wind in the western Pacific (Figure 40 and Figure 49),
- iii) OLR out of phase with temperature perturbations at 300hPa (LL90, their Figures 14b and 15e),

- iv) rising (sinking) motion appears with positive (negative) temperature perturbation at 300hPa (LL90, their Figure 16), and
- v) first baroclinic mode observed with geopotential height; the first baroclinic mode structure will be further discussed in next section.

Low-level unfiltered zonal wind is recorded during the times when MRG waves events are found (Figure 49) and the recorded zonal wind fields for each MRG wave do not align at a certain longitude. MRG waves appear in an environment where the lower tropospheric westerlies and easterlies meet in the western Pacific.

Note that the term $-\overline{\omega' T'}$ in equation (9) here is positive (Figure 47c,d). It means the eddy kinetic energy of the MRG waves is increasing with time, due to the energy conversion from the eddy available potential energy.

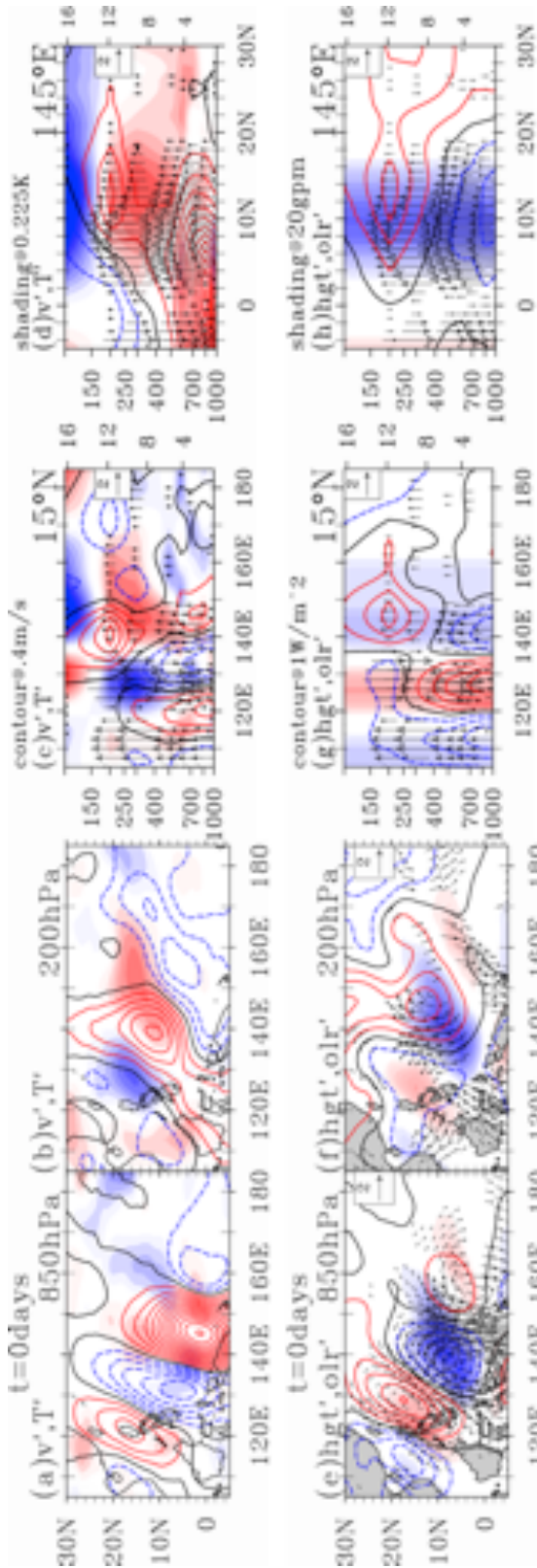


Figure 47 – Composites of MRG wave events at $t=0$ days between 110°E - 180° (western Pacific).

The filtered variables are (a)-(d) V-wind (contour, at 0.4 m s^{-1} levels) and temperature (shading, at 0.225 K levels); (e)-(h) geopotential height (contour, at 1 gpm levels) and OLR (shading, at 1 W m^{-2} levels). Red, black and blue lines are positive, zero and negative values. Red and blue shadings are positive and negative values.

(a) and (e) are 850 hPa composite maps and (b) and (f) are 200 hPa composite maps. (c) and (g) are vertical cross-sections at 15°N . (d) and (h) are vertical cross-sections at the middle longitude of the composites. Vectors in the horizontal cross sections are horizontal wind (m s^{-1}) at that level. Vectors in the vertical cross sections are the pressure velocities (Pa s^{-1}) with values multiplied by 150. The vectors in all graphs are 99.9% above significance level in Student t-test (please refer to text). Values of OLR are shown for all vertical levels in (g) and (h). MRG waves are found with region 110°E to 180° (defined in section 5.1). Total number of events over 30 years is 956. Label bars of temperature and OLR (shadings) can be found in the appendix.

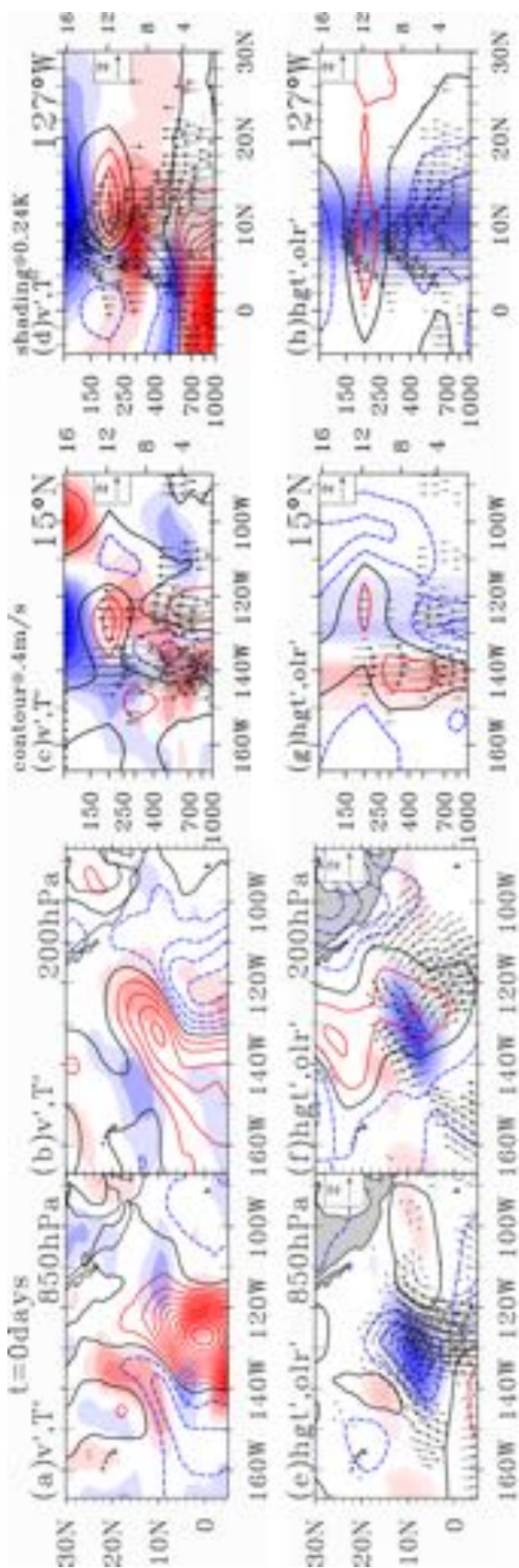


Figure 48 – Same as Figure 47 except the graphs are for MRG waves between 180° and 75° W (eastern Pacific). Vectors in the vertical cross sections are the pressure velocities (Pa s^{-1}) with values multiplied by 300. Total number of events over 30 years is 935.

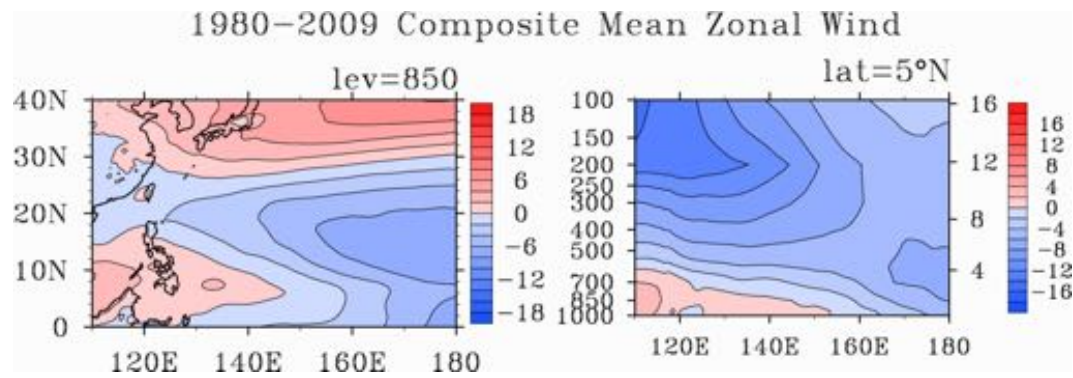


Figure 49 – Average unfiltered 850hPa zonal wind during the times for MRG events tracked in western Pacific (graphs not aligned in longitudes). Left graph is 850hPa distribution of composite zonal wind. Right graph is vertical cross-section of zonal wind. Units: m s^{-1}

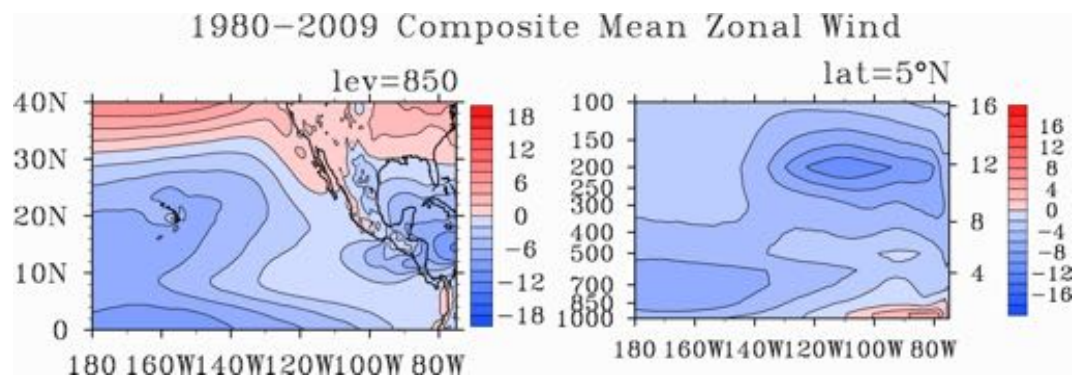


Figure 50 – Same as Figure 49 except for eastern Pacific

5.3.2 Composites from t=-5.5day to 4day

So far the discussions have been focused on the t=0day composites and the results are consistent with past studies. More details of the MRG wave structures can be revealed by comparing the composites before and after the t=0day (black dots before and after the blue circles in Figure 31). We extend our examination to time period before and after the tracked MRG events from t=-5.5 day to t=4day. The significance of the vectors (vertical and horizontal wind) in the composites drops significantly before t=-5.5day and after t=4day. Student t-test is performed on differences between the MRG composites and the 30-season average filtered data. Since the locations of the fields used in composing the composites are all different (MRG events are found anywhere within 110°E-180°), the composites cannot be used to compare any particular average filtered domain. Hence for each MRG composite, with grid box size of 80° longitude × 30° latitude, a significance test is performed between the composite and the 30-season average filtered data at different locations:

i) 65°E-145°E

ii) 75°E-155°E

iii) 85°E-165°E

iv) 95°E-175°E

v) 105°E-175°W

vi) 115°E-145°W

vii) 125°E-145°W

viii) 135°E-145°W

ix) 145°E-145°W

In this study, values in the composites are considered to be significantly different from the 30-season average filtered data if the composite is significantly different from all the above domains by 99.9%.

The structure of the pre-MRG waves ($t=-5.5$ day, Figure 51) is different from $t=0$ day (see Figure 47). Here comparison is made between $t=-5.5$ day composite and $t=0$ day composite because they have the same phase of temperature perturbation (warm/cold core locations) and the warm/cold cores at 300hPa are suggested to be out of phase with convective activities (mentioned in last section). Also, major structural change happens within $t=-5.5$ to $t=0$ day. The composites from $t=-5.5$ to 4.5day with time interval of 0.5day are included in the appendix. Hereafter, the $t=5.5$ day and $t=0$ day composites will be referred to as the pre-MRG waves and MRG waves respectively.

The pre-MRG waves are rather barotropic for the v-wind and geopotential height (Figure 51c,g) comparing to the first baroclinic mode of the MRG waves at

$t=0$ day (mentioned in last section). Some past studies (Reed Recker 1971 their Figure 10, Liebmann and Hendon their Figure 21, Yang et al. 2007a Figure 7, Yang et al. 2007c their Figure 6) have supported the idea of opposite signs in upper and lower-level v-wind. This is more obvious when one examines the period in between, say the $t=-3.5$ day composite (see appendix). The active convection (negative OLR) at $t=-2$ day (see appendix) near 160° E moves to the center of the circulation at $t=0$ day around 140° E (Figure 47e). This can be observed in the whole series of composites and the convection appears to become more coupled with circulation west of the middle longitude (145° E) comparing to east of middle longitude.

Another major change during $t=-5.5$ day to $t=0$ day is the phase relationship between temperature and v-wind perturbations. Since the vertical wave activity flux is downward if $v'T' < 0$ and vice versa (wave activity flux as defined by Takaya and Nakamura 2001; see their equation 32, see also Tam and Li 2006), the signs of $v'T'$ for the pre-MRG and MRG waves will be examined here. At $t=-5.5$ day (Figure 51c), most of the 300hPa cold (warm) core is covered by positive (negative) v-wind perturbations. At $t=0$ day (Figure 47c), the 300hPa warm core at 145° E is covered by positive v-wind perturbations. Sign of $v'T'$ changes from negative to positive. In other words, before the MRG waves are

tracked ($t=0$ day), there is a time period when the wave activity flux is travelling downward from upper levels until the upper-level (lower-level) circulations become weaker (stronger) (see composites in appendix). Similar argument was put forth by Tam and Li (2006) based on regressed vorticity and temperature perturbations (their Figure 6). Similar to the schematic diagrams of warm/cold cores shown in Chang et al. 1970 (their Figure 6) and Wallace 1971 (their Figure 18), schematic diagrams are plotted here to show the change of phase relationship between the temperature and v-wind perturbations (Figure 52 and Figure 53).

Scale contraction is also observed during the period $t=-5.5$ day to $t=0$ day (see Figure 51c,g and Figure 47c,g). The wavelength is about 50° longitude at $t=-5.5$ day and about 30° longitude at $t=0$ day. By examining the whole time series of composites in the appendix, the scale contraction of the lower-level wave structures is more obvious. The lower-level scale contraction made it possible for the lower-level v-wind to “catch up” with the upper-level v-wind, and hence the westward tilting is observed for the MRG waves in the western Pacific (Figure 47c and Figure 53).

The composites composed here show that the upper-level synoptic-scale activities are important in the development of MRG waves, which are considered as the lower-level wave train structure. In this study, the composite MRG

structures are consistent with results from past study. The new algorithm, which tracked MRG waves by both space and time, however allows further studies on statistics between MRG wave occurrences and TC genesis and case-by-case studies for TC formations during wave transformation in the future.

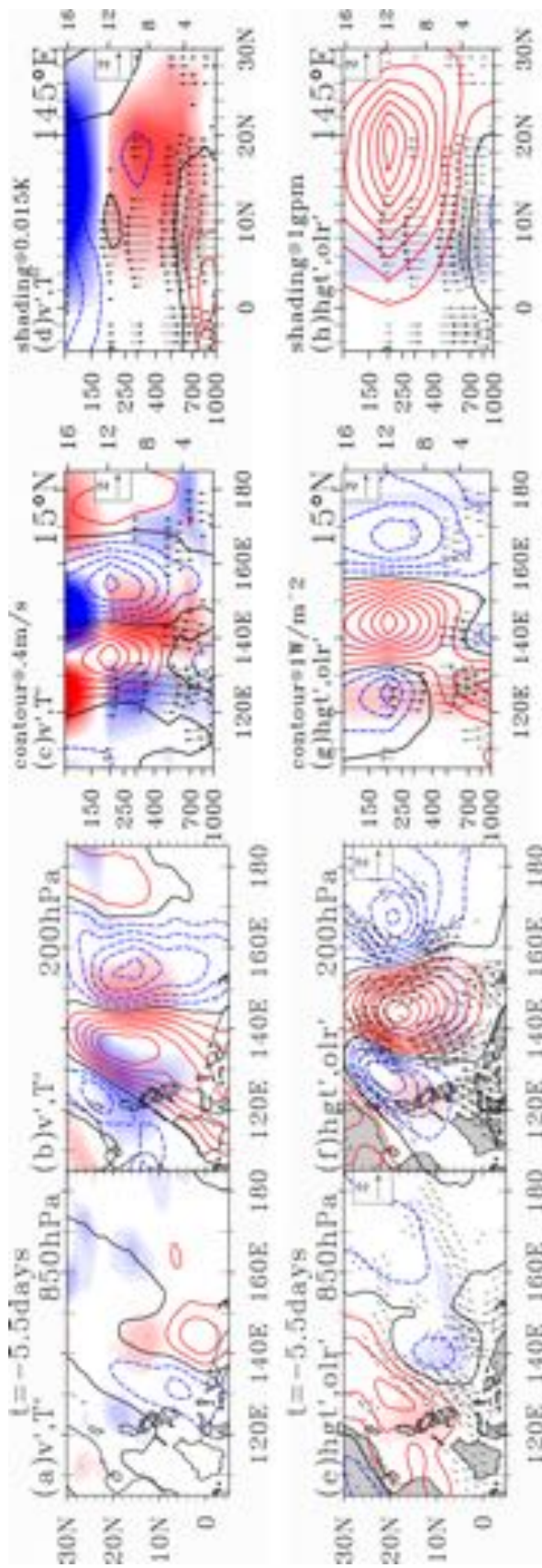


**Figure 51 – Same as Figure 47 except the graphs are at $t = -5.5$ day.
Same values for the contour and shading levels are used here.**

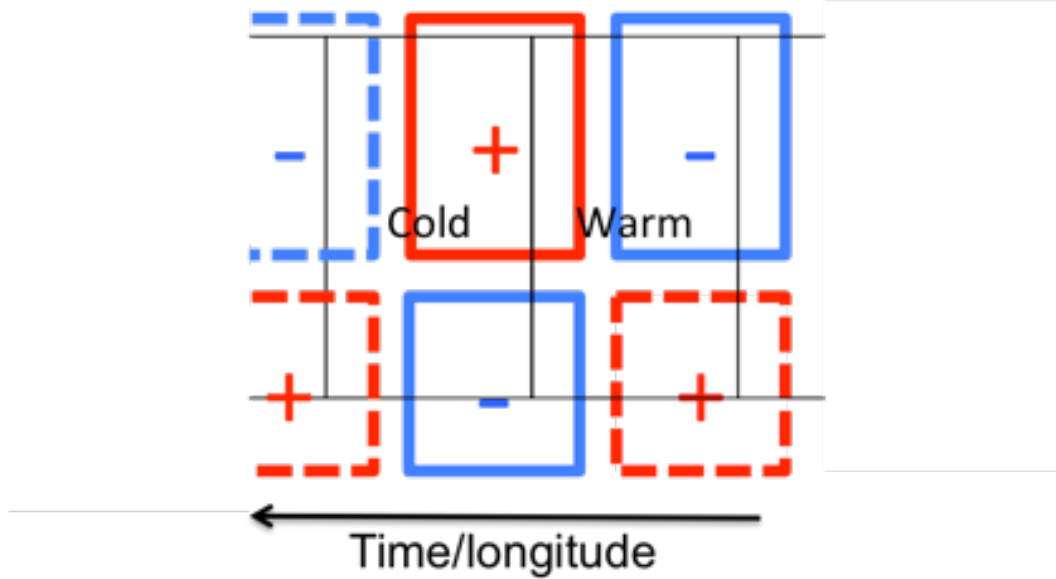


Figure 52 – Schematic diagram of vertical-latitudinal cross-section of composite $t=-5.5\text{day}$ (refer to Figure 51c). Black boxes indicate the temperature perturbations with words “warm” and “cold”. Red and blue boxes are v-wind perturbations. The red (blue) box with solid lines is the positive (negative) v-wind at high levels between $130^\circ\text{E}-140^\circ\text{E}$ ($150^\circ\text{E}-160^\circ\text{E}$).

The dashed boxes do not exist in $t=-5.5\text{day}$, but, after examining the composites following $t=-5.5\text{day}$ in the appendix, they are plotted there to show a complete picture of the waves.

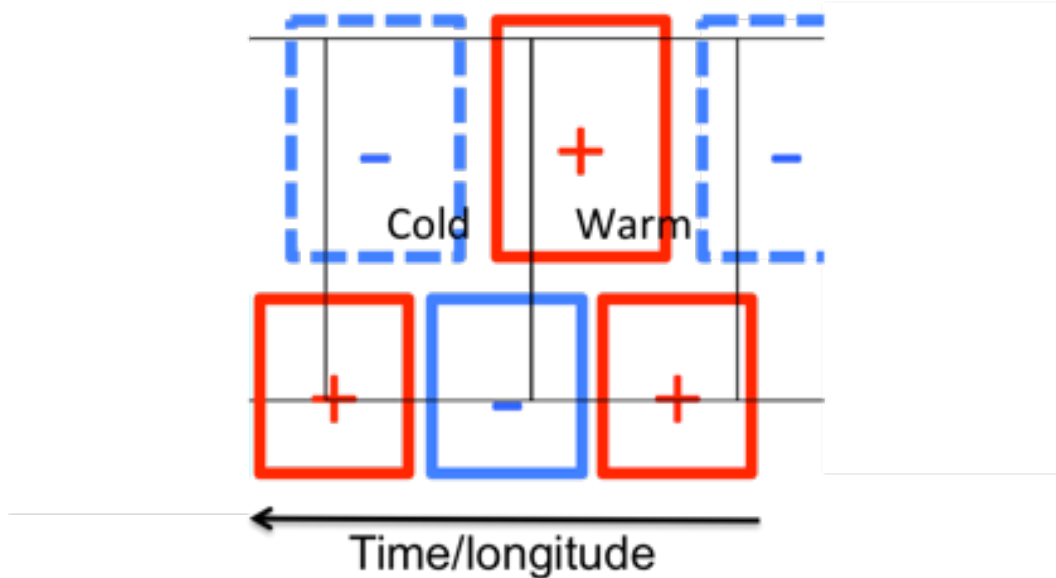


Figure 53 – Same as Figure 52, except it is for $t=0\text{day}$ (refer to Figure 47). The red box with solid lines is the positive (negative) v-wind at high levels between $140^\circ\text{E}-150^\circ\text{E}$.

5.4 Energetics

To find out contributions of different processes in EKE generation (section 2.6), each term in equation (9) for each MRG wave (blue circle in Figure 31) are calculated. For each MRG wave, the transient quantities (variables with prime notation) are the filtered data from $t=-5\text{day}$ to 5day . The averaged quantities such as \bar{u} and \bar{v} are from the average unfiltered data around the found location of each MRG wave (average value within area 5°S to 15°N and $\pm 30^{\circ}$ longitude around each stated location, similar to \bar{U} section 4.3). The dissipation term is not included here. The fields are then aligned at location of each MRG wave in the same way as producing composites. The terms are phase-independent and each term of EKE from $t=-5\text{day}$ to $t=5\text{day}$ is averaged so that at least one period is included (Figure 54). For each of the term, horizontal composites at two levels (850hPa and 300hPa) and vertical composites (15°N or 15°N) are calculated. The EKE tendency terms for western Pacific (Figure 54 and Figure 55) and eastern Pacific (Figure 56 and Figure 57) are included for comparison. The (h) panel of each graph is the EKE term and (a)-(g) are the tendency terms. Note that the advection term is plotted with contour levels one order greater than all other terms (however it is not considered as a real source as it merely moves energy around).

The western Pacific EKE (Figure 54h) at 850hPa has its highest values lying

at the same location of the northwestward moving path of the MRG waves. Below 400hPa, the kinetic energy generation relies on the barotropic conversion (Figure 54g). The barotropic conversion is the sum of first four terms in (9). The largest contributors are the $-\overline{u'v'} \frac{\partial}{\partial y} \bar{u}$, $-\overline{u'^2} \frac{\partial}{\partial x} \bar{u}$ and $-\overline{v'^2} \frac{\partial}{\partial y} \bar{v}$ (Figure 54a,c,e). The covariance $\overline{u'v'}$ is positive due to the northeast-southwest orientation of the waves (Figure 47a,e) and $\overline{u'^2}$ is always positive. The background flow for the MRG waves (Figure 40) in the western Pacific shows that both $\frac{\partial}{\partial x} \bar{u}$ and $\frac{\partial}{\partial y} \bar{u}$ is negative, due to the westerlies between 0° and 10°N (easterlies in the north versus westerlies in the south; easterlies in the east versus westerlies in the west). The northeast-southwest tilting that gives rise to positive $\overline{u'v'}$ and the zonal background flow both lead to the energy extraction from the mean flow.

The vertical distribution is similar to those in Maloney and Dickinson (2003). Highest values in the vertical dimension are located at 200hPa (Figure 55h), which could be generated by high-level barotropic conversion (Figure 55g). The location of the baroclinic conversion $-\frac{R}{p} \overline{\omega' T'}$ (Figure 55b) coincides with the low-level EKE generated around Philippines (Figure 54h), which agree with past studies that both barotropic and baroclinic conversion are important in the synoptic-scale wave activities (LL90, Maloney and Dickinson 2003).

The difference between the western and eastern Pacific can be examined by

comparing the barotropic conversion (Figure 54g and Figure 56g), which dominates the energy generation for both basins. In the western Pacific, the east part of the barotropic conversion comes from mean v-wind shear (Figure 54e) while west part of it comes from mean zonal wind shear (Figure 54a,c). It means that there is a shift in the MRG wave energy source as they move westward. The situation is not the same in the eastern Pacific (Figure 56g). It is obvious that only the mean v-wind shear is the largest contributor. In other words, the transient energy generation process in western Pacific changes depending on the location, while it is mostly the same in the eastern Pacific. In both basin, the v-wind shear terms contribute the most near equatorial latitude (5-10°N), only that there are a few features unique to the off-equatorial western Pacific: zonal wind shear energy generation terms (Figure 54a,b), covariance $\overline{u'v'}$ (horizontal wave tilting) (Figure 54a) and upper-level baroclinic conversion (Figure 55b). The background confluent flow (yellow shading in Figure 40) in the western Pacific allows transient eddies to draw energy from the mean flow and the positive covariance $\overline{u'v'}$ enhances the conversion process. Also another feature unique to the western Pacific is the strong upper-level EKE generation, as temperature perturbation starts to be larger in the off-equatorial area (small in the Tropics) and vertical wind is stronger in later stage of the waves (refer to section 5.3). All features

unique to the western Pacific region are closed linked and further detailed study is

needed to find the relationship between the features.

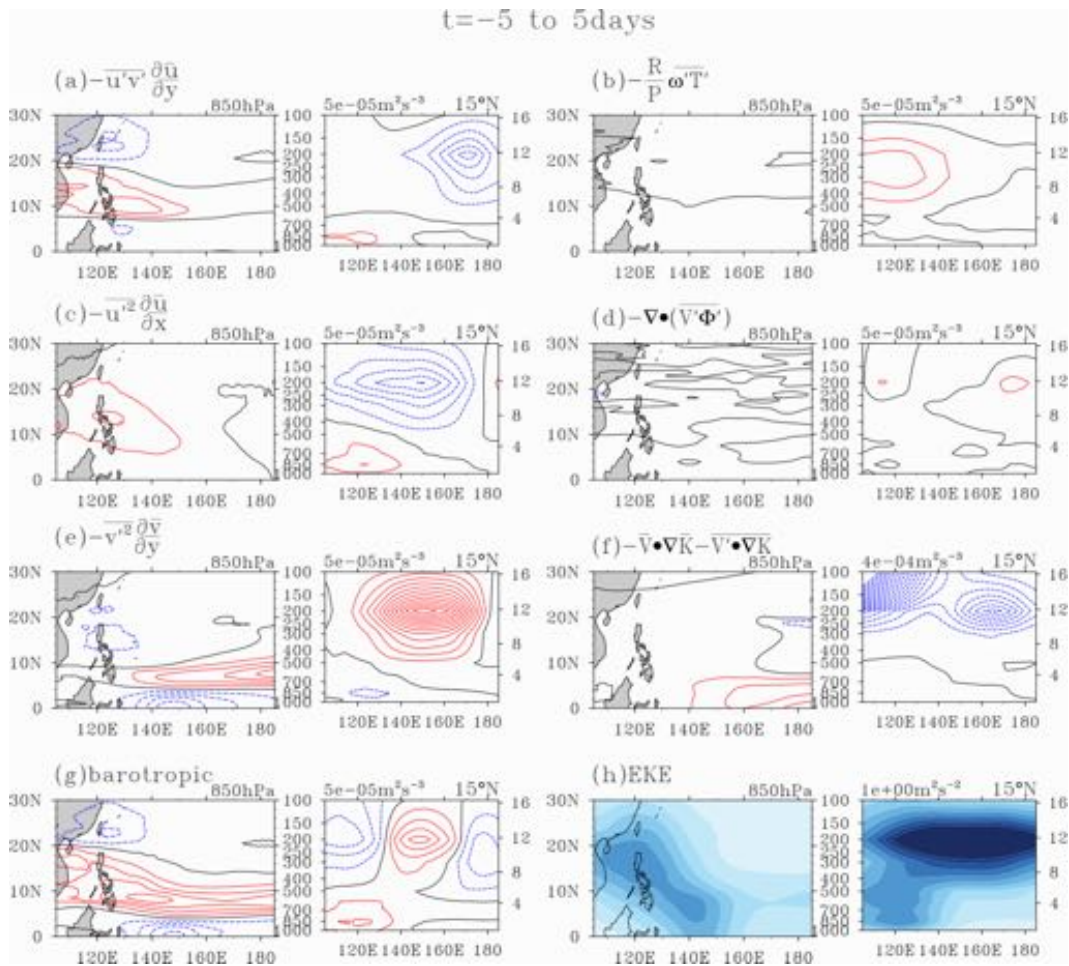


Figure 54 – Vertical and horizontal composites of average EKE and EKE tendency terms in (9) for MRG waves for the western Pacific. They include (a)(c)(e) three barotropic terms, (e) barotropic energy conversion, or, sum of all barotropic terms, (b) baroclinic conversion, (d) convergence of the geopotential flux, (f) advection of EKE by mean and perturbation flow, and (h) EKE.

For each term, a vertical composite (15°N) and a 850hPa horizontal composite are plotted. Red and blue contour lines are positive and negative values. Black contour line equals to zero. Contour interval level is marked on each term. EKE is shown by shading levels.

$t = -5$ to 5 days

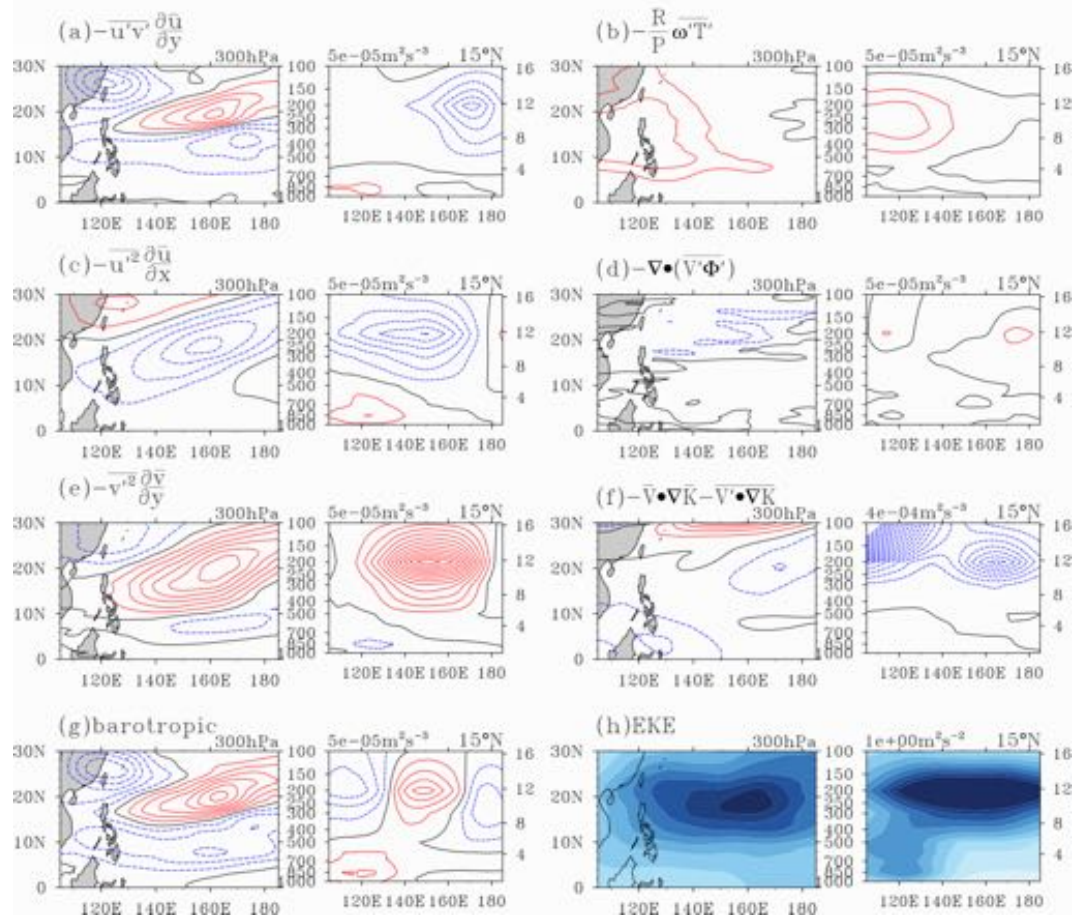


Figure 55 – Same as Figure 54 except for higher horizontal levels (300hPa).

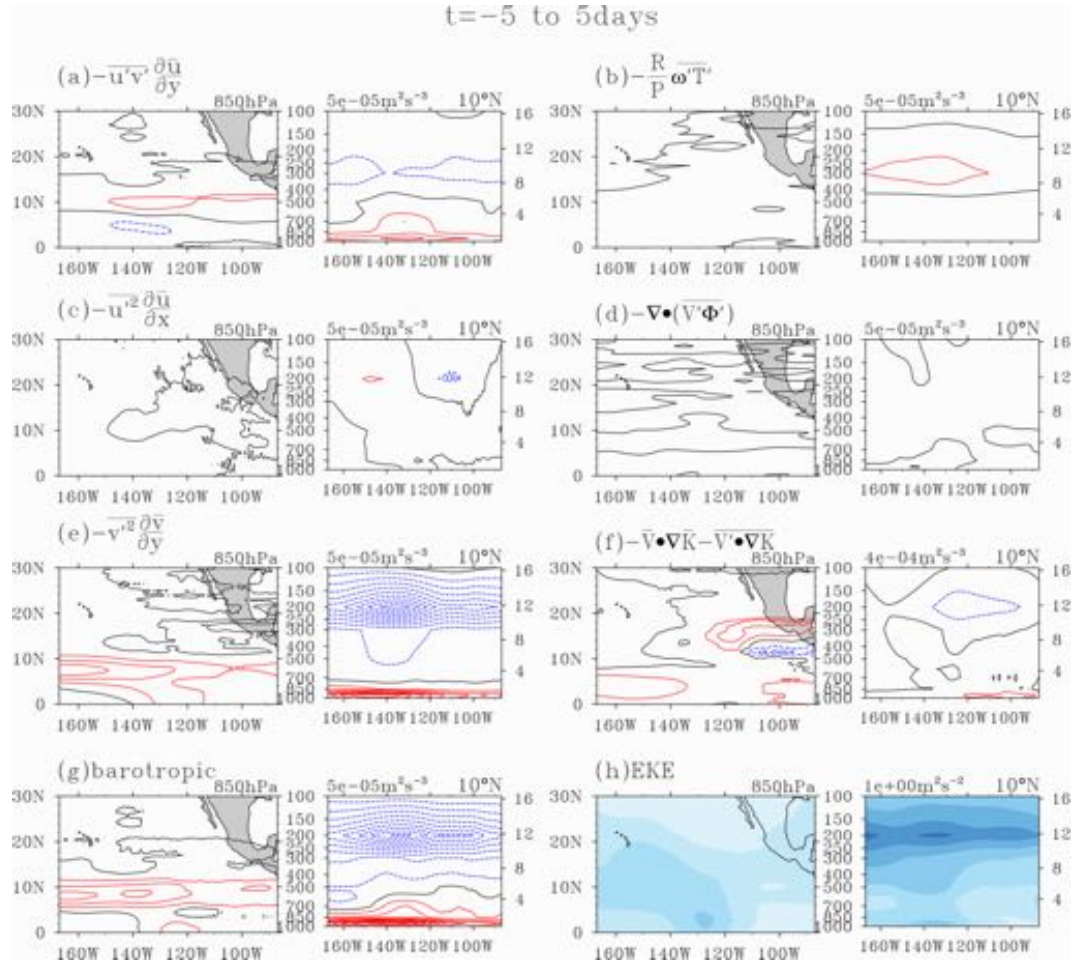


Figure 56 – Same as Figure 54 except for the eastern Pacific.

$t = -5$ to 5 days

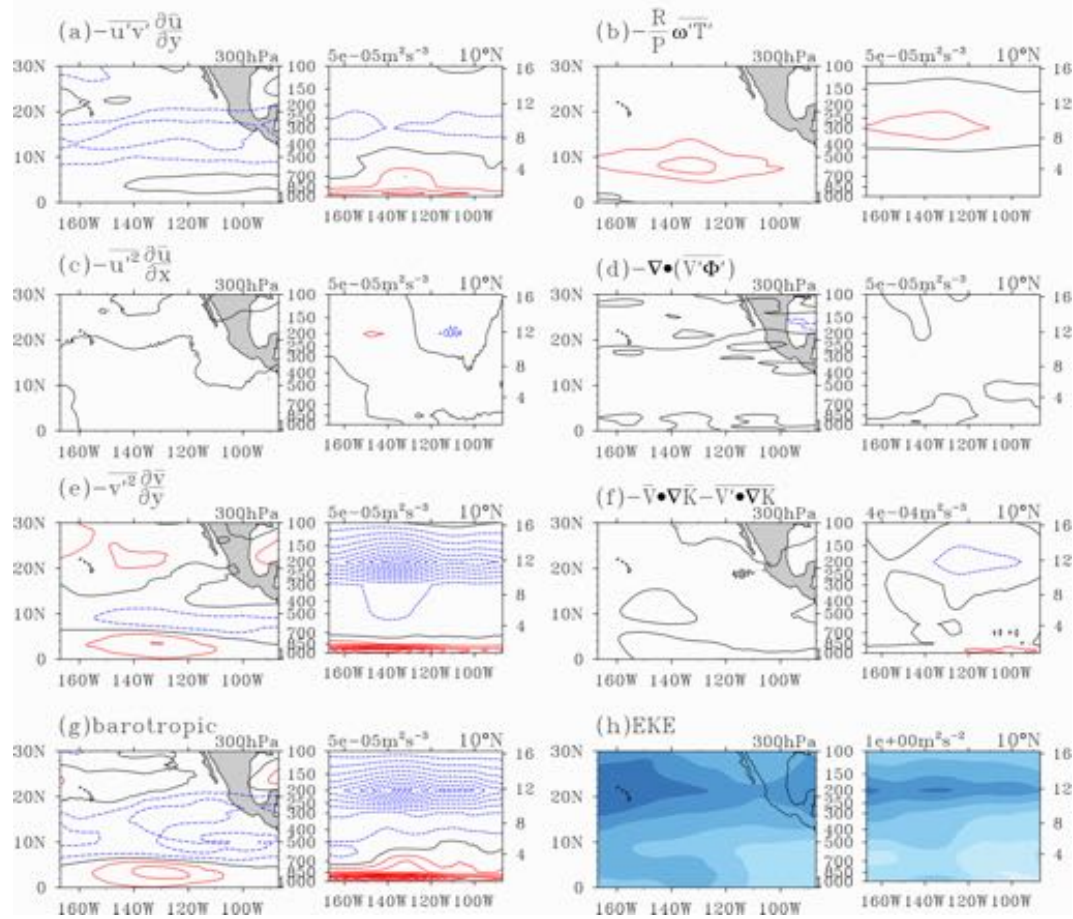


Figure 57 – Same as Figure 55 except for the eastern Pacific.

Chapter 6

Discussion and Conclusion

A new algorithm has been developed to track the low-level westward travelling MRG waves in the tropical western and eastern Pacific based on their theoretical structure stated in the SWE solutions. First, spectral analysis was performed on the reanalysis dataset, CFSR, so as to determine suitable wavenumber-frequency (period=3-8 day, k =-20 to 0) domain for the data filtering process. Wave features were extracted by lag-correlation to ensure that the wave features found in the dataset are consistent with those in past studies. After applying the new wave tracking algorithm, the occurrence time and location of each MRG wave as well as their wave properties such as wavenumber and intrinsic frequency at the equator were recorded.

The wave properties found were plotted on dispersion diagrams, and two major groups of wave activities were found (with wavenumber $k\sim 6$ and $k\sim 11$). While both groups appear in the western Pacific, mainly $k\sim 6$ waves were found in eastern Pacific. The fact that both $k\sim 6$ and $k\sim 11$ waves appear in the western Pacific agrees with past discussions on the co-existence of MRG waves and tropical-disturbance type (TD-type) waves. The high-wavenumber wave activities

($k \sim 11$) mainly appear west of dateline, implying that there is little relationship between high-wavenumber MRG waves in eastern and western Pacific and some initiation processes may take place in that region. One possibility why more high-wavenumber waves observed in the western than in the eastern Pacific is that wave contraction (as shown in the composites) takes place in the western Pacific. As shown in the western Pacific composites, wave contraction is observed in the northwestward moving wave train; this could be due to the confluent background flow in the low levels. This was discussed in Section 2.7. Also noteworthy here is that the MRG waves in western Pacific are observed to have larger variations in terms of their dispersive properties. That means that their waveform is less regular and it is better to track them without assuming any fixed wave structure in space.

Although the tracking algorithm in this study is designed to track MRG waves at the equator, TD-type waves are also observed in the circulation composites to the west of the tracked MRG waves over the western Pacific; i.e. wave transition occurs when wave trains move northwestward in the western North Pacific. Energetics of the basin shows that transient activities can grow under the negative mean zonal wind shear in both latitudinal and longitudinal directions ($\frac{\partial}{\partial x} \bar{u} < 0$ and $\frac{\partial}{\partial y} \bar{u} < 0$), and in conjunction with the northeast-southwest horizontal tilting structure of the eddies ($\overline{u'v'} > 0$). This kind

of structure in the northwestward-moving wave train is favorable for the growth of TD-type waves. Another possible mechanism involved in the MRG-TD transition is wave accumulation (if TD-type waves are defined as high-wavenumber waves). It was suggested in past studies that mean zonal wind convergence could amplify wave energy and could reduce the wave scale through a wave accumulation process (mentioned in Section 2.7). On the other hand, a theoretical study with a two-level equatorial beta-plane and spherical coordinates models showed that, the climatological easterly vertical wind shear in the western Pacific can be favorable for trapping of wave kinetic energy in the lower troposphere (Wang and Xie 1996). This could explain why the perturbation kinetic energy is trapped in low levels in a region of easterly vertical wind shear (in the energetics found in this study). It was also suggested that the easterly wind shear is favorable for strong Ekman vertical velocity in the boundary layer and the MRG wave mode could be destabilized in the easterly wind shear environment (Xie and Wang 1996). This could be a mechanism where the active convection becomes more coupled with the low-level circulations in the off-equatorial area (as shown in the composites). Since TD-type waves could be defined by phase relationship between circulation and convection or wave contraction, objective definitions are needed in order to conduct research of the wave transformation in

the future.

From the vertical composites, the negative $v'T'$ suggests downward vertical wave activity flux prior to the occurrences of MRG waves. Wave composites show that the phase relationship between temperature and v-wind changes during wave propagation: the term $v'T'$ becomes less negative and finally becomes mainly positive. Meanwhile, the upper-level wave activities fade and lower-level wave activities thrive. Also, vertical cross-sections along the middle longitude give hints on the connection between the upper-level and lower-level activities. The influence of upper-level and higher-latitude wave activities on the tropical MRG waves is obvious by examining the vertical cross-sections. This was mentioned in Section 5.3.2.

MRG occurrences in the wavenumber-frequency domain and the occurrences according to geographical locations have been recorded. And yet their interannual and intraseasonal occurrences have not examined and should be addressed in the future. Statistics of MRG waves, such as their occurrences, strengths and locations can also be compared to TC statistics. We can also separate cases depending whether they contributed to TC formation. Since the MRG waves were found to relate to extra-tropical activities, numerical simulations could be done to further examine the processes involved.

Finally, it is important to have a method recording MRG waves, given their contributions to TC formations in the western Pacific, as generally accepted by the research community. Even with an objective method, it is still very challenging to delineate the relationship between these waves and TC genesis and also the role of the background flow, due to the complicated situation in the summertime western Pacific where the monsoon westerlies meet the trade wind easterlies (Figure 4). Also, other types of tropical waves (such as equatorial Rossby waves) also are related to TC formation (Ching et al 2010). Nevertheless, the objective method presented here can provide a way to record MRG waves, and in the future, this would allow examining possible wave-TC transformation mechanism from the point of view of tropical waves.

References

A-B

Abramowitz, M. and I. A. Stegun, 1972: Handbook of Mathematical Functions with Formulas, Graphs and Mathematical Tables. National Bureau of Standards. Applied Mathematics Series- 55. 19.13

Briegel, L. M. and W. M. Frank, 1997: Large-Scale Influences on Tropical Cyclogenesis in the Western North Pacific. *Mon. Wea. Rev.*, **125**, 1397–1413.

C

Chan, S. C., J. L. Evans, 2002: Comparison of the structure of the ITCZ in the west Pacific during the boreal summers of 1989–93 using AMIP simulations and ECMWF reanalysis. *J. Climate*, **15**, 3549–3568

Chang, C-P., 1970: Westward Propagating Cloud Patterns in the Tropical Pacific as seen from Time-Composite Satellite Photographs. *J. Atmos. Sci.*, **27**, 133–138.

Chang C.-P., V. F. Morris and J. M. Wallace, 1970: A statistical study of easterly waves in the western Pacific: July–December 1964. *J. Atmos. Sci.*, **27**, 195–201.

Chen, G., R. Huang, 2009: Interannual Variations in Mixed Rossby–Gravity Waves and Their Impacts on Tropical Cyclogenesis over the Western North Pacific. *J. Climate*, **22**, 535–549.

Chen, G., and C.-Y. Tam, 2012: A new perspective on the excitation of low-tropospheric MRG waves in association with energy dispersion, *J. Atmos. Sci.* **69**, 1397–1403.

Ching, L., C-H. Sui, M-J. Yang. 2010: An analysis of the multiscale nature of tropical cyclone activities in June 2004: Climate background. *J. Geophys. Res.*, **115**

D

- Dickinson, M., and J. Molinari, 2002: Mixed Rossby–gravity waves and western Pacific tropical cyclogenesis. Part I: Synoptic evolution. *J. Atmos. Sci.*, **59**, 2183–2196.
- Done, J. M., G. J. Holland, P. J. Webster, 2010: The role of wave energy accumulation in tropical cyclogenesis over the tropical North Atlantic. *Clim. Dynm.*, **36**, 753–767
- Dunkerton, T. J., 1993: Observation of 3-6 day Meridional wind oscillations over the tropical Pacific, 1973-1992: vertical structure and interannual variability. *J. Atmos. Sci.*, **50**, 3292–3307.

Dunkerton, T. J. and M. P. Baldwin, 1995: Observation of 3-6 day Meridional wind oscillations over the tropical Pacific, 1973-1992: horizontal structure and propagation. *J. Atmos. Sci.*, **52**, 1585–1601.

F-G

- Frank, W. M., and P. E. Roundy, 2006: The role of tropical waves in tropical cyclogenesis. *Mon. Wea. Rev.*, **134**, 2397–2417.
- Fu, B., T. Li, M. S. Peng, and F. Weng, 2007: Analysis of tropical cyclogenesis in the western North Pacific for 2000 and 2001. *Wea. Forecasting*, **22**, 763–780.
- Gehne, M., R. Kleeman, 2012: Spectral Analysis of Tropical Atmospheric Dynamical Variables Using a Linear Shallow-Water Modal Decomposition. *J. Atmos. Sci.*, **69**, 2300–2316.
- Gu, G., and C. Zhang, 2001: A spectrum analysis of synoptic-scale disturbances in the ITCZ. *J. Climate*, **14**, 2725–2739.

H

- Ha, Y., Z. Zhong, Y. Zhu, and Y. Hu, 2013: Contributions of Barotropic Energy Conversion to Northwest Pacific Tropical Cyclone Activity during ENSO. *Mon. Wea. Rev.*, **141**, 1337–1346.

- Hendon, H. H., and B. Liebmann 1994: Organization of convection within the Madden-Julian oscillation, *J. Geophys. Res.*, **99**, 8073–8083
- Hendon, H. H., and M. C. Wheeler, 2008: Some space-time spectral analyses of tropical convection and planetary-scale waves., *J. Atmos. Sci.*, **65**, 2936-2948.
- Holton, J. R., 1971: A Diagnostic Model for Equatorial Wave Disturbances; The Role of Vertical Shear of the Mean Zonal Wind, *J. Atmos. Sci.*, **28**, 55-64.
- Holton, J. R., 2004: *An Introduction to Dynamic Meteorology*. 4th ed. Elsevier, 535 pp.

Hsu, P.-C. and Tim Li, 2011: Interactions between Boreal Summer Intraseasonal Oscillations and Synoptic-Scale Disturbances over the Western North Pacific. Part II: Apparent Heat and Moisture Sources and Eddy Momentum Transport, *J. Climate*, **24**, 942–961.

K

- Kiladis, G. N., 1998: Observations of Rossby waves linked to convection over the eastern tropical Pacific. *J. Atmos. Sci.*, **55**, 321–339.
- Kiladis, G. N., M. C. Wheeler, P. T. Haertel, K. H. Straub, and P. E. Roundy, 2009: Convectively coupled equatorial waves, *Rev. Geophys.*, **47**, RG2003, doi:10.1029/2008RG000266.
- Kuo, H-C, J-H Chen, R. T. Williams, C-P. Chang, 2001: Rossby Waves in Zonally Opposing Mean Flow: Behavior in Northwest Pacific Summer Monsoon. *J. Atmos. Sci.*, **58**, 1035–1050.

L

- Lau, K. H., and N. C. Lau, 1990: Observed structure and propagation characteristics of tropical summertime synoptic scale disturbances. *Mon. Weather Rev.*, **118**, 1888–1913
- Lau, K. H., and N. C. Lau, 1992: The energetics and propagation dynamics of tropical summertime synoptic-scale disturbances. *Mon. Weather Rev.*, **120**, 2523-2539

Li, T., B. Fu, X. Ge, B. Wang, and M. Peng, 2003: Satellite data analysis and numerical simulation of tropical cyclone formation. *Geophys. Res. Lett.*, **30**, 2122

Lindzen, R. S., 1967: Planetary waves on beta planes. *Mon. Wea. Rev.*, **95**, 441-451.

Liu, K. S. and J. C. L. Chan, 2003: Climatological characteristics and seasonal forecasting of tropical cyclones making landfall along the South China coast. *Mon. Wea. Rev.*, **131**, 1650-1662.

Liebmann, B., and H. H. Hendon, 1990: Synoptic-scale disturbances near the equator. *J. Atmos. Sci.*, **47**, 1463 – 1479

M

Magaña, V., and M. Yanai, 1995: Mixed Rossby-Gravity Waves Triggered by Lateral Forcing. *J. Atmos. Sci.*, **52**, 1473-1486

Mak, M.-K., 1969: Laterally Driven Stochastic Motions in the Tropics. *J. Atmos. Sci.*, **26**, 41-64

Maloney, E. D. and M. J. Dickinson, 2003: The Intraseasonal Oscillation and the Energetics of Summertime Tropical Western North Pacific Synoptic-Scale Disturbances, *J. Atmos. Sci.*, **60**, 2153-2168

Maloney, E. D., and D. L. Hartmann, 2001: The Madden-Julian oscillation, barotropic dynamics, and north Pacific tropical cyclone formation. Part I: Observations. *J. Atmos. Sci.* , **58** , 2545-2558.

Maruyama, T., and M. Yanai, 1967: Evidence of large-scale wave disturbances in the equatorial lower stratosphere. *J. Meteor. Soc. Japan*, **45**, 196-199.

Matsuno, T., 1966: Quasi-geostrophic motions in the equatorial area. *J. Meteorol. Soc. Jpn.*, **44**, 25-43.

N

Nakazawa, T., 1988: Tropical super clusters within intraseasonal variations over the western Pacific, *J. Meteorol. Soc. Jpn.*, **66**, 823 – 839.

Nitta, T., 1970: On the role of transient eddies in the tropical troposphere. *J. Meteor. Soc. Japan*, **48**, 348–359.

Nitta, T., and Y. Takayabu, 1985: Global analysis of the lower tropospheric disturbances in the Tropics during the northern summer of the FGGE year. Part II: Regional characteristics of the disturbances. *Pure Appl. Geophys.*, **123**, 272-292.

P-R

Pires, P., J-L. Redelsperger, J-P. Lafore, 1997: Equatorial Atmospheric Waves and Their Association to Convection. *Mon. Wea. Rev.*, **125**, 1167–1184.

Reed, R. J., E. Klinker, and A. Hollingsworth, 1988: The structure and characteristics of African easterly wave disturbances as determined from the ECMWF Operational Analysis/Forecast System. *Meteor. Atmos. Phys.*, **38**, 22–33.

Reed, R. J., and E. E. Recker, 1971: Structure and properties of synoptic-scale wave disturbances in the equatorial western Pacific. *J. Atmos. Sci.*, **28**, 1117-1133.

Riehl, H., 1945: Waves in the easterlies and the polar front in the tropics. *Miscellaneous Rep. 17*, Department of Meteorology, University of Chicago, 79 pp.

Roundy, P. E. and W. M. Frank, 2004: A Climatology of Waves in the Equatorial Region. *J. Atmos. Sci.*, **61**, 2105-2132.

Roundy, P. E., 2012: Tracking and prediction of large-scale organized tropical convection by spectrally focused two-step space-time EOF analysis. *Q. J. Roy. Meteorol. Soc.*, **138**, 919-931.

S

Saha, S., and Coauthors, 2010: The NCEP climate forecast system reanalysis. *Bull. Amer. Meteor. Soc.*, **91**, 1015–1057.

Salby, M. L., 1981: The 2-day Wave in the Middle Atmosphere: Observations and Theory. *J. Geophys. Res.*, **86**, 9654-9660

- Serra, Y. L., G. N. Kiladis, and M. F. Cronin, 2008: Horizontal and Vertical Structure of Easterly Waves in the Pacific ITCZ. *J. Atmos. Sci.*, **65**, 1266–1284.
- Sobel, A. H., C. S. Bretherton, 1999: Development of Synoptic-Scale Disturbances over the Summertime Tropical Northwest Pacific. *J. Atmos. Sci.*, **56**, 3106–3127.

T

- Takaya, K., and H. Nakamura, 2001: A formulation of a phase-independent wave-activity flux for stationary and migratory quasigeostrophic eddies on a zonally varying basic flow. *J. Atmos. Sci.*, **58**, 608–627.
- Takayabu, Y. N., 1994a: Large-scale cloud disturbances associated with equatorial waves. Part I: Spectral features of the cloud disturbances. *J. Meteor. Soc. Japan*, **72**, 433–448.
- Takayabu, Y. N., 1994b: Large-scale cloud disturbances associated with equatorial waves. Part II: Westward propagating inertio-gravity waves. *J. Meteor. Soc. Japan*, **72**, 451–465.
- Takayabu, Y. N., and T. Nitta, 1993: 3-5 day-period disturbances coupled with convection over the tropical Pacific Ocean. *J. Meteor. Soc. Japan*, **71**, 221–246.
- Tam, C. Y., T. Li, 2006: The Origin and Dispersion Characteristics of the Observed Tropical Summertime Synoptic-Scale Waves over the Western Pacific. *Mon. Wea. Rev.*, **134**, 1630–1646.
- Torrence, C., and G. P. Compo, 1998: A practical guide to wavelet analysis. *Bull. Amer. Meteor. Soc.*, **79**, 61–78.

Y

- Yanai, M. and T. Maruyama, 1966: Stratospheric wave disturbances propagating over the equatorial Pacific. *J. Meteor. Soc. Jap.*, **44**, 291-294.

Yanai M., T. Maruyama, T. Nitta and Y. Hayashi, 1968: Power spectra of large-scale disturbances over the tropical Pacific. *J. Meteorol. Soc. Jpn.*, **46**, 308-323.

Yang, G. Y., B. Hoskins, and J. Slingo, 2003: Convectively coupled equatorial waves: A new methodology for identifying wave structures in observational data. *J. Atmos. Sci.*, **60**, 1637-1654.

Yang, G. Y., B. Hoskins, and J. Slingo, 2007a: Convectively coupled equatorial waves. Part II: Propagation characteristics. *J. Atmos. Sci.*, **64**, 3424–3437.

Yang, G. Y., B. Hoskins, and J. Slingo, 2007b: Convectively coupled equatorial waves. Part III: Synthesis structures and their forcing and evolution. *J. Atmos. Sci.*, **64**, 3438–3451.

Yang, G. Y., B. Hoskins, and J. Slingo, 2007c: Convectively coupled equatorial waves: Part III: Synthesis structures and their forcing and evolution. *J. Atmos. Sci.*, **64**, 3438-3451.

W

Wang, B., and X. Xie, 1996: Low-Frequency equatorial waves in vertically shear flow. Part I: Stable waves. *J. Atmos. Sci.*, **53**, 449-467.

Wallace, J. M., 1971: Spectral studies of tropospheric wave disturbances in the tropical western Pacific. *Rev. Geophys. Space Phys.*, **9**, 557-612.

Wallace, J. M. and C-P. Chang, 1969: Spectral analysis of large-scale wave disturbances in the tropical lower troposphere. *J. Atmos. Sci.*, **26**, 1010-1025.

Wallace, J. M., and V. E. Kousky, 1968: Observational evidence of Kelvin waves in the tropical stratosphere. *J. Atmos. Sci.*, **25**, 900-907.

Wallace, J. M. and P. V. Hobbs, 2006: Atmospheric Science: An Introductory Survey, 2nd Ed., Academic Press, 504 pp.

Wheeler, M., and G. N. Kiladis, 1999: Convectively coupled equatorial waves: Analysis of clouds and temperature in the wavenumber–frequency domain. *J. Atmos. Sci.*, **56**, 374-399.

Wheeler, M., G. N. Kiladis, P. J. Webster, 2000: Large-Scale Dynamical Fields Associated with Convectively Coupled Equatorial Waves. *J. Atmos. Sci.*, **57**, 613–640.

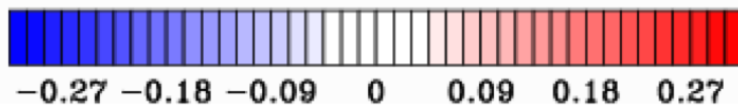
X-Z

- Xie, X., and B. Wang, 1996: Low-frequency equatorial waves in vertically sheared zonal flows. Part II: Unstable waves, *J. Atmos. Sci.*, **53**, 3589– 3605.
- Xu, Y., T. Li and M. Peng, 2014: Roles of Synoptic-Scale Wave Train, the Intraseasonal Oscillation, and High-Frequency Eddies in the Genesis of Typhoon Manyi (2001). *J. Atmos. Sci.*, **71**, 3706-3722
- Zehr, R.M., 1992: Tropical cyclogenesis in the Western North Pacific. NOAA Technical Report NESDIS 61, U. S. Department of Commerce, Washington, DC, 181 pp.
- Zhou, X. Q., and B. Wang (2007), Transition from an eastern Pacific upper-level mixed Rossby-gravity wave to a western Pacific tropical cyclone, *Geophys. Res. Lett.*, **34**, L24801, doi:10.1029/2007GL031831.

Appendix – Composites of MRG structures in western Pacific

This appendix shows all the western Pacific composites from $t=-5.5\text{day}$ to $t=4\text{day}$. All graphs have same arrangement in the panels and same contour/shading levels. The hatchings with solidus shape and backslash shape in (a)-(d) represent statistically significant areas with level of 99.9% for v-wind and temperature respectively (refer to section 5.3.2 for details of the statistical test). The hatchings with solidus shape and backslash shape in (e)-(h) represent the significant areas for geopotential height and OLR respectively.

Here's the label bar (Units: K) for temperature from (a)-(d):



And the label bar for OLR (Units: W m^{-2}) from (e)-(h),

